Faculty of Aerospace Engineering

Robust Stability Augmentation of a Le Mans Prototype 1 race car using Incremental Nonlinear Dynamic Inversion

M. B. Ruijs

July 4, 2018

TU Delft Delft University of Technology

Challenge the future

Robust Stability Augmentation of a Le Mans Prototype 1 race car using Incremental Nonlinear Dynamic Inversion

Master of Science Thesis

For obtaining the degree of Master of Science in Aerospace Engineering
at Delft University of Technology

M. B. Ruijs

July 4, 2018

Faculty of Aerospace Engineering · Delft University of Technology

Delft University of Technology

Delft University Of Technology
Department Of
Control and Simulation

The undersigned hereby certify that they have read and recommend to the Faculty of Aerospace Engineering for acceptance a thesis entitled **"Robust Stability Augmentation of a
Le Mans Prototype 1 race car using Incremental Nonlinear Dynamic Inversion"** by **M. B. Ruijs** in partial fulfillment of the requirements for the degree of **Master of Science**.

Dated: July 4, 2018

Readers:

Dr.ir. Q. P. Chu

Dr.ir. E. van. Kampen

Dr.ir. C. C. de. Visser

ir. R. Noomen

Acknowledgments

I like to thank the people that have supported me throughout my master thesis project. In particular, I am very grateful for the initial support from my supervisor Dr.ir. Q.P. Chu for my wish to write master thesis at Audi Sport and all the Skype sessions that followed which helped me so very much. I am also very thankful for the support from Martin Kalkofen and Marvin Struijk who supervised me during my internship and subsequent master thesis project. Their support from the very start to finish helped me bring this project to a successful end.

I would further like to thank all the people that let me drive to AS with them every single day. It allowed me to stay live in Munich throughout the project and make some very good friends along the way. For which I am truly thankful.

Mart Ruijs

Contents

Part I

Paper

Robust Stability Augmentation for an LMP1 Race Car Using Incremental Nonlinear Dynamic Inversion

M. B. Ruijs[a] and Q. P. Chu[b]

[a]Delft University of Technology, Delft, Netherlands; [b]Delft University of Technology, Delft, Netherlands;

ARTICLE HISTORY
Compiled July 4, 2018

ABSTRACT

In this paper Incremental Nonlinear Dynamic Inversion, a sensor based approximate form of Feedback Linearization with favorable robustness properties, is applied to the traction control and stability augmentation problem of a Le Mans Prototype 1 race car. A cascaded side-slip and yaw-rate envelope protection system is developed in combination with a model following yaw-rate controller which acts inside the safe envelope. The vehicle is controlled through two limited slip differentials featured in the front and rear of the vehicle. A method is presented to account for load-tranfer effects in the calculation of the limited control effectiveness associated the actuators . Simulations with a high-fidelity vehicle model demonstrate that the control system is robust against parameter uncertainties and is able to effectively keep the vehicle within the bounds of the safe envelope.

KEYWORDS
Vehicle Stability Augmentation, Incremental Nonlinear Dynamic Inversion, Feedback Linearization, Le Mans Prototype 1, Limited Slip Differential, Load Transfers, Envelope Protections

1. Introduction

The World Endurance Championship (WEC) features some of the most technologically advanced race cars that exist today. The Le Mans Prototype 1 (LMP1) class of race cars compete in races lasting from 6 up to 24 hours, the most famous being the *'24h of Le Mans'*. The WEC stands out from other championships in that it allows the use of certain technologies which have been prohibited in other forms of racing. Where most competitions have banned the use of modern driver assist technologies like Traction Control (TC) and Electronic Stability Control (ESC), the WEC, a tournament revolving around technology and strategy, permits a restricted form of TC to be used. In this paper, Incremental Nonlinear Dynamic Inversion (INDI), a robust nonlinear control technique first developed for aerospace applications, is investigated outside its usual context and will be applied to the traction and stability control problem of an LMP1 race car.

ESC systems are primarily developed for reasons of added safety in limit conditions where the average driver would otherwise lose control [1]. Therefore, most ESC sys-

CONTACT M. B. Ruijs Email: mart_ruijs@outlook.com

tems that can be found on consumer cars prevent the driver from entering the highly non-linear parts of the vehicle state-space entirely. However, in the context of high-performance vehicles, driving further into this nonlinear region is advantageous for performance around a lap [2]. In other words, the control system should increase the driver's ability to keep the race car in this region of the state-space.

Automotive control systems frequently feature nonlinear Sliding Mode Control (SMC) techniques [3–6] as these tend to offer some robustness in the presence of parameter uncertainties but tend to suffer from chatter in the control signal. Other nonlinear control techniques, such as Nonlinear Dynamic Inversion (NDI), are inherently difficult to apply to road vehicle control due to the nature of the tire force characteristics. Control inputs typically do not appear affine in the state equations, which requires either strong assumptions on the manner in which forces are modeled [7], or nonlinear optimizations to find the controls [8]. Other possibilities include linearization of the equations involved in the optimization [9], or neglecting the nonlinear nature of the tire-force characteristics entirely [10].

Furthermore, ESC systems typically rely on a form of differential braking [3,11, 12], differential drive [13], active steering[7] or a combination thereof [4,14,15]. In the vehicle under consideration, two power units, one at the front and one at the rear of the vehicle, distribute the drive force through two limited slip differentials and form the only means of controlling traction forces. Although the control authority of such systems is limited compared to differential brake or differential drive systems, the longitudinal distribution of drive forces has a strong effect on the vehicle dynamics [16] and has been investigated a means of yaw-rate control [17,18]. However, the limited control authority may require the consideration of secondary effects such as lateral and longitudinal load-transfers [19,20] due to vehicle accelerations.

Envelope protection systems potentially provide the driver with more control authority inside the safe envelope compared to classical model following techniques [21,22]. Therefore, a side-slip and yaw-rate stability augmentation and envelope protection system is developed which incorporates the bounds presented in [21]. The cascaded control structure is based on INDI. This sensor based nonlinear control technique has favorable robustness characteristics over classical NDI [23]. Furthermore, INDI can be applied, with relative ease, to a much wider range of nonlinear systems such as those with control variables that do not appear affine in the state equations.

The structure of this paper is as follows: Firstly, section 2 briefly describes the theory behind INDI. Section 3 provides the model that was used in the approximate inversion of the drive-train and yaw-rate dynamics. The structure of the proposed control system and the envelope is given in section 4. Next, section 5 provides the derivation of the control effectiveness of the front and rear drive-trains and a method for including load-transfer effects. Lastly, section 6 provides simulation results of the stability augmentation system in conjunction with a high-fidelity vehicle model.

2. Incremental Nonlinear Dynamic Inversion

Incremental Nonlinear Dynamic Inversion (INDI) is an approximate, sensor based, form of Nonlinear Dynamic Inversion [23], sometimes also referred to as approximate [24] or simplified Feedback Linearization [25]. INDI can be applied to the general nonlinear system (1) and starts by approximating the state equations using a Taylor

series expansion (2).

$$\dot{\mathbf{x}} = \mathbf{f}(\mathbf{x}, \mathbf{u}) \tag{1}$$

$$\dot{\mathbf{x}} \approx \mathbf{f}(\mathbf{x}_0, \mathbf{u}_0) + \left.\frac{\partial \mathbf{f}(\mathbf{x}, \mathbf{u})}{\partial \mathbf{x}}\right|_{(\mathbf{x}_0, \mathbf{u}_0)} (\mathbf{x} - \mathbf{x}_0) + \left.\frac{\partial \mathbf{f}(\mathbf{x}, \mathbf{u})}{\partial \mathbf{u}}\right|_{(\mathbf{x}_0, \mathbf{u}_0)} (\mathbf{u} - \mathbf{u}_0) + \text{h.o.t.} \tag{2}$$

By neglecting higher order terms and realizing that for high control rates the term $(\mathbf{x} - \mathbf{x}_0)$ vanishes, equation 2 simplifies to,

$$\dot{\mathbf{x}} \approx \mathbf{f}(\mathbf{x}_0, \mathbf{u}_0) + \left.\frac{\partial \mathbf{f}(\mathbf{x}, \mathbf{u})}{\partial \mathbf{u}}\right|_{(\mathbf{x}_0, \mathbf{u}_0)} (\mathbf{u} - \mathbf{u}_0). \tag{3}$$

Further, noting that the first term can be substituted with a measurement of the state derivative at t_0,

$$\mathbf{f}(\mathbf{x}_0, \mathbf{u}_0) = \dot{\mathbf{x}}_0, \tag{4}$$

and defining the control effectiveness as,

$$\mathbf{G}(\mathbf{x}_0, \mathbf{u}_0) = \left.\frac{\partial \mathbf{f}(\mathbf{x}, \mathbf{u})}{\partial \mathbf{u}}\right|_{(\mathbf{x}_0, \mathbf{u}_0)}, \tag{5}$$

equation 3 simplifies to,

$$\dot{\mathbf{x}} \approx \dot{\mathbf{x}}_0 + \underbrace{\mathbf{G}(\mathbf{x}_0, \mathbf{u}_0)}_{\text{Control Effectiveness}} (\mathbf{u} - \mathbf{u}_0). \tag{6}$$

Where $\dot{\mathbf{x}}_0$ is the state derivative measured at time $t = t_0$.

Similar to exact NDI [26], by equating the right hand side of equation 6 to ν and inverting, one ends up with a mapping between the original control input u and the virtual control ν (7), which once applied to equation 1 results in an approximate linear differential relation between the state $\mathbf{x}$ and ν (8).

$$\Delta \mathbf{u} = \mathbf{G}^{-1}(\mathbf{x}_0, \mathbf{u}_0)(\nu - \dot{\mathbf{x}}_0) \tag{7}$$

$$\dot{\mathbf{x}} \approx \nu \tag{8}$$

Note that in contrast with regular NDI the mapping (7) results in a control increment only. The new control input can be calculated with equation 9.

$$\mathbf{u} = \Delta \mathbf{u} + \mathbf{u}_0 \tag{9}$$

Where $\mathbf{u}_0$ is the actuator state as measured at time $t = t_0$.

3. Vehicle Model

The control effectiveness required for the approximate inversion of the drive-train and yaw-rate dynamics is determined using a 7-DOF vehicle model [18,27,28]. The motion

is assumed completely planar. Furthermore, the roll and pitch angles are assumed to be small and the corresponding dynamics fast enough, such that these states and the associated wheel normal loads can be approximated by their steady-state values [29]. Tire forces are modeled with a normalized Magic Formula (MF)-like function in conjunction with the similarity method [30]. The behavior of the front and rear Limited Slip Differentials (LSD) are described by a relatively detailed model that accurately captures the transition between locked and unlocked conditions [31] as this behavior greatly influences the magnitude and even the sign of the control effectiveness. This phenomenon detailed in a later section.

3.1. Vehicle Body Dynamics

The vehicle body dynamics, which are described by the three states corresponding to the translational and rotational motion of the vehicle in the horizontal plane, are depicted in 1. Also shown are the wheel force vectors.

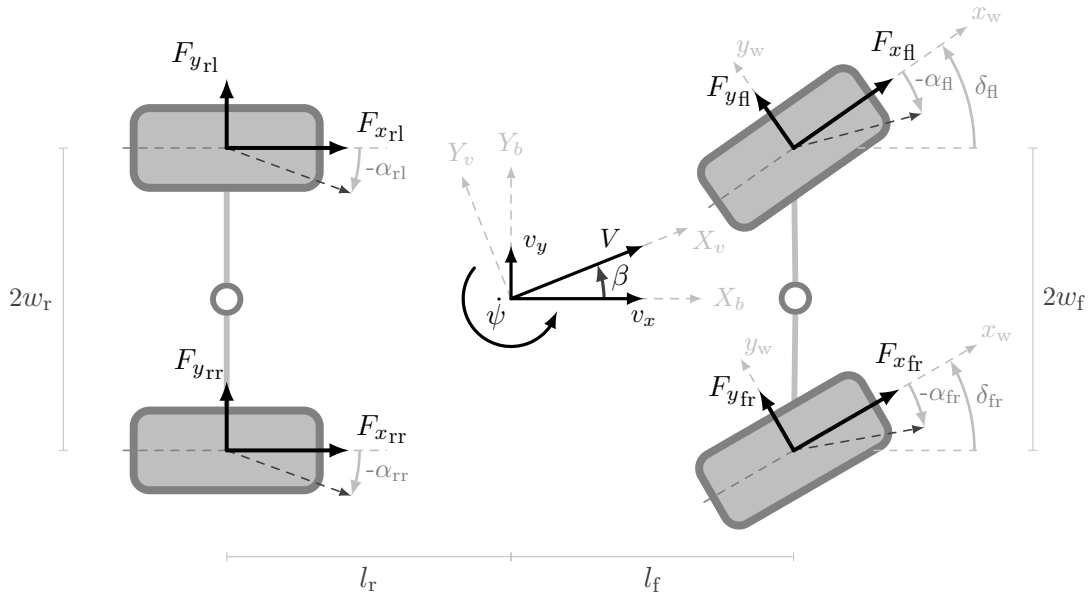

Figure 1. Two-track vehicle model

The body state vector is defined as $\mathbf{x}_{\mathrm{B}} = \begin{bmatrix} v_x & v_y & \dot{\psi} \end{bmatrix}^{\mathrm{T}}$, where v_x, v_y and $\dot{\psi}$ stand for the longitudinal velocity, lateral velocity and yaw-rate respectively. Using $\mathbf{x}_{\mathrm{B}}$, the equations describing the body dynamics can be compactly expressed in matrix form as [16,28],

$$\dot{\mathbf{x}}_{\mathrm{B}} = \mathbf{M}^{-1}\mathbf{E}\,{}^{\mathrm{B}}\mathbf{F} - c. \tag{10}$$

Where $\mathbf{M} = \mathrm{diag}\,(m, m, I_{zz})$, ${}^{\mathrm{B}}\mathbf{F} = \begin{bmatrix} {}^{b}F_{x_{\mathrm{fl}}} & {}^{b}F_{y_{\mathrm{fl}}} & \dots & {}^{b}F_{x_{\mathrm{rr}}} & {}^{b}F_{y_{\mathrm{rr}}} \end{bmatrix}^{\mathrm{T}}$, $c = \begin{bmatrix} -v_y\dot{\psi} & v_x\dot{\psi} & 0 \end{bmatrix}^{\mathrm{T}}$

and $\mathbf{E}$ is given by,

$$\mathbf{E} = \begin{bmatrix} 1 & 0 & 1 & 0 & 1 & 0 & 1 & 0 \\ 0 & 1 & 0 & 1 & 0 & 1 & 0 & 1 \\ -w_{\mathrm{f}} & l_{\mathrm{f}} & w_{\mathrm{f}} & l_{\mathrm{f}} & -w_{\mathrm{r}} & -l_{\mathrm{r}} & w_{\mathrm{r}} & -l_{\mathrm{r}} \end{bmatrix}. \tag{11}$$

The transformation from the tire force vector ${}^{\mathrm{W}}\mathbf{F}$ expressed in the wheel frame to the tire-force vector in the body frame ${}^{\mathrm{B}}\mathbf{F}$ appearing in equation 10 is given by equation 12.

$${}^{\mathrm{B}}\mathbf{F} = \mathbb{T}_{\mathrm{B,W}}\, {}^{\mathrm{W}}\mathbf{F} \tag{12}$$

$$\mathbb{T}_{\mathrm{B,W}} = \mathrm{diag}\left(\mathbb{T}_{\mathrm{B,W_{fl}}}, \mathbb{T}_{\mathrm{B,W_{fr}}}, \mathbb{T}_{\mathrm{B,W_{rl}}}, \mathbb{T}_{\mathrm{B,W_{rr}}}\right) \tag{13}$$

Where the sub-rotation matrices depend on the corresponding steering angles δ_{ij} are given by,

$${}^{\mathrm{B}}\mathbf{F}_{ij} = \mathbb{T}_{\mathrm{B,W}_{ij}}\, {}^{\mathrm{W}}\mathbf{F}_{ij} \tag{14}$$

$$\begin{bmatrix} {}^{b}F_{x_{ij}} \\ {}^{b}F_{y_{ij}} \end{bmatrix} = \begin{bmatrix} \cos\delta_{ij} & -\sin\delta_{ij} \\ \sin\delta_{ij} & \cos\delta_{ij} \end{bmatrix} \begin{bmatrix} {}^{w}F_{x_{ij}} \\ {}^{w}F_{y_{ij}} \end{bmatrix}$$

Subscripts $i \in \{\mathrm{f}, \mathrm{r}\}$ and $j \in \{\mathrm{l}, \mathrm{r}\}$ denote the front or rear and left or right wheel respectively.

3.2. Normal Loads

High performance vehicles commonly feature stiff suspensions and low centers of gravity. Consequently, the time constants associated with the roll and pitch degrees of freedom can be assumed to be small compared to those of the planar body dynamics [2]. Therefore, the effects of changing normal loads on the control effectiveness, are approximated with a steady state load-transfer model adopted from [29]. Equations 15a and 15b give the lateral load-transfers for the front and rear axles respectively.

$$\Delta W_{y_{\mathrm{f}}} = A_y \frac{m}{2w_{\mathrm{f}}} \left(\frac{K_{\phi\mathrm{f}}}{K_{\phi\mathrm{f}} + K_{\phi\mathrm{r}} - m\, h_{\mathrm{s}}} + \frac{l_{\mathrm{r}}}{l} h_{\mathrm{f}} \right) \tag{15a}$$

$$\Delta W_{y_{\mathrm{r}}} = A_y \frac{m}{2w_{\mathrm{r}}} \left(\frac{K_{\phi\mathrm{r}}}{K_{\phi\mathrm{f}} + K_{\phi\mathrm{r}} - m\, h_{\mathrm{s}}} + \frac{l_{\mathrm{f}}}{l} h_{\mathrm{r}} \right) \tag{15b}$$

Where $K_{\phi\mathrm{f}}$ and $K_{\phi\mathrm{r}}$ denote the front and rear roll-stiffnesses, and h_{f} and h_{r} the corresponding roll-center heights. Lastly, A_y denotes the specific force in lateral direction, h_{s} is the vertical distance between the roll-axis and the center of gravity and l represents the wheel base. Longitudinal load transfers are approximated with equation 16.

$$\Delta W_x = A_x \frac{h\, m}{l} \tag{16}$$

Where, A_x is the specific force in longitudinal direction and h is the height of the center of gravity.

The normal loads for each wheel are now given by equation 17.

$$\mathbf{F}_z = \mathbf{F}_{z\,\mathrm{stat}} + \Delta\mathbf{F}_z \tag{17}$$

Where $\mathbf{F}_{z\,\mathrm{stat}}$ represents the static normal load distribution and the load-transfer vector is given by,

$$\begin{aligned}\Delta\mathbf{F}_z = [&-\Delta W_x - \Delta W_y, -\Delta W_x + \Delta W_y,\\ &-\Delta W_x - \Delta W_y, -\Delta W_x + \Delta W_y]\end{aligned} \tag{18}$$

3.3. Drive-Train

The behavior of the front and rear drive-trains, including the Salisbury type LSDs, is described by a model adopted from [31,32]. Instead of using the commonly used left and right wheel speeds or drive-shaft velocities as state variables, the motion is described by the average movement of the system and the difference between the left and right drive-shafts (19).

$$2\omega_\mathrm{p} = \omega_\mathrm{l} + \omega_\mathrm{r} \tag{19a}$$

$$2\omega_\mathrm{d} = \omega_\mathrm{l} - \omega_\mathrm{r} \tag{19b}$$

Where, ω_p is the angular velocity of the prop-shaft and $2\omega_\mathrm{d}$ denotes the delta between the left and right wheel-speeds, respectively ω_l and ω_r. This choice of state variables allows the motion to be described by a reduced order model if two or more bodies stick, i.e., if one or more states become zero. Circumventing the need to estimate the indeterminate static friction forces [33]. Equations 20a and 20a describe the motion of a single axle. The subscript i has been dropped for clarity.

$$\dot{\omega}_\mathrm{p} = \frac{K_\mathrm{t} T_\mathrm{in} - {}^{b}F_{x\mathrm{l}} \cdot R_\mathrm{e} - {}^{b}F_{x\mathrm{r}} \cdot R_\mathrm{e} - T_\mathrm{L}}{J_\mathrm{eq} + 2J_\mathrm{w} + J_\mathrm{c}} \tag{20a}$$

$$\dot{\omega}_\mathrm{d} = \frac{-T_\mathrm{D} - {}^{b}F_{x\mathrm{l}} \cdot R_\mathrm{e} + {}^{b}F_{x\mathrm{r}} \cdot R_\mathrm{e}}{2J_\mathrm{w} + J_\mathrm{d}} \tag{20b}$$

Where ${}^{b}F_{x\mathrm{l}}$ and ${}^{b}F_{x\mathrm{l}}$ denote the left and right longitudinal wheel forces on the corresponding axle and R_e stands for the effective wheel radius. Torque T_L accounts for possible friction losses in the drive train and T_D is used to model limited-slip behavior. The factor K_t, represents the total transmission gain and control input T_in is the torque coming from the power-unit. The combined inertia of the power-unit, transmission and prop-shafts, incorporating the effect of transmission-ratios, is represented by J_eq. The terms relating to the differential, J_d and J_c, respectively denote the inertia of the casing and those parts that only move if $\omega_\mathrm{d} \neq 0$. Lastly, the inertia of the wheels and corresponding drive-shafts are lumped into J_w.

Friction forces T_D and T_L are approximated with a coulomb friction model with a distinction between static and kinetic friction. Equation 21 gives the kinetic friction model for T_D.

$$T_{\mathrm{D_k}} = \max\left(T_{\mathrm{D_{k0}}}, r_{\mathrm{D_k}} \cdot |T_\mathrm{p}|\right) \cdot \mathrm{sgn}\left(\omega_\mathrm{d}\right) \tag{21}$$

Where the coefficient $r_{\mathrm{D_k}}$ depends on the geometry of the ramps which cause the internal clutch package to compress, leading to the characteristic torque transfer. The term $T_{\mathrm{D_{k0}}}$ depends on the differential's preload settings and T_{p} stands for the input torque experienced at the differential and is corrected for the accelerations of the power-unit, transmission and prop-shaft (22).

$$T_{\mathrm{p}} = \frac{K_{\mathrm{t}} T_{\mathrm{in}} \cdot 2J + ({}^{b}F_{x\mathrm{l}} \cdot R_{\mathrm{e}} + {}^{b}F_{x\mathrm{r}} \cdot R_{\mathrm{e}})(J_{\mathrm{eq}} + J_{\mathrm{c}})}{2J_{\mathrm{w}} + J_{\mathrm{eq}} + J_{\mathrm{c}}} \tag{22}$$

The maximum static friction $T_{\mathrm{D_{max}}}$ is defined similarly.

Four cases are used to describe the sticking and sliding behavior of the two differentials [31,32].

- Case 1: $\omega_{\mathrm{p}} \neq 0, \omega_{\mathrm{d}} \neq 0$
  Both states are non-zero, therefore no sticking of the moving parts occurs. The motion of the differential is described by both equations (20a) and (20b). Therefore, the differential torque transfer and torque due to friction losses are given by their kinetic values, i.e., $T_{\mathrm{D}} = T_{D_{\mathrm{k}}}$ and $T_{\mathrm{L}} = T_{L_{\mathrm{k}}}$.
- Case 2: $\omega_{\mathrm{p}} \neq 0, \omega_{\mathrm{d}} = 0$
  When the relative velocity between the left and right wheel is zero, the differential is said to be locked. In this scenario, the drive-train effectively moves as a single body and associated dynamics can therefore be described by a single equation (20a). As long as the torque required to maintain this condition ($\dot{\omega}_{\mathrm{d}} = 0$) is less than the maximum static friction force, the relative velocity between the left and right wheel remains zero. The required torque follows from equation 20b and is simply given by,

  $$\tilde{T}_{\mathrm{D}} = -{}^{b}F_{x\mathrm{l}} \cdot R_{\mathrm{e}} + {}^{b}F_{x\mathrm{r}} \cdot R_{\mathrm{e}} \tag{23}$$

  The resulting friction force can now be expressed as,

  $$T_{\mathrm{D}} = \begin{cases} \tilde{T}_{\mathrm{D}} & \text{if,} \quad |\tilde{T}_{\mathrm{D}}| \leq T_{\mathrm{D_{max}}} \\ T_{\mathrm{D_{max}}} \mathrm{sgn}(\tilde{T}_{\mathrm{D}}) & \text{otherwise.} \end{cases} \tag{24}$$

  The prop-shaft's rotational velocity is non-zero and friction force T_{L} is given by its kinetic value,

  $$T_{\mathrm{L}} = T_{\mathrm{L_s}}.$$

Cases three and four, corresponding to $\{\omega_{\mathrm{p}} = 0, \omega_{\mathrm{d}} \neq 0\}$ and $\{\omega_{\mathrm{p}} = 0, \omega_{\mathrm{d}} = 0\}$, are defined similarly but are of little practical value for the design of the control system. However, the first two cases descried above, $\{\omega_{\mathrm{p}} \neq 0, \omega_{\mathrm{d}} = 0\}$ and $\{\omega_{\mathrm{p}} \neq 0, \omega_{\mathrm{d}} = 0\}$, determine the torque distribution created by a limited slip differential and therefore have a large influence on the vehicle dynamics. Specifically, switching from case 1 to 2 and vice versa will play a dominant role in the choice of control system structure and the determination of the control effectiveness.

3.4. Tire Model

Tire forces are evaluated with an MF-like model and the similarity method [30]. The force-slip characteristic is normalized at some reference normal force, after which the normalized curved can be appropriately scaled to represent different driving conditions. Equation 25 gives the normalized reference MF used in this paper.

$$F_{k\mathrm{n}}(\phi) = \frac{1}{\mu_{i0} F_{z0}} F_k \left(\frac{C_{Fk0}}{\mu_{k0} F_{z0}} \phi \right) \Bigg|_{F_z = F_{z0}} \tag{25}$$

$$F_{k\mathrm{n}}(\phi) = \sin\left[1/B_{k\mathrm{n}} \arctan\left\{B_{k\mathrm{n}}\phi - E_{k0}\left(B_{k\mathrm{n}}\phi - \arctan(B_{k\mathrm{n}} \cdot \phi)\right)\right\}\right] \tag{26}$$

The force in the direction $k \in \{x, y\}$ is then found by rescaling the reference curve using,

$$F_k = (\mu_k(F_z) \cdot F_z) \frac{\sigma_k}{\sigma} F_{k\mathrm{n}} \left(\sigma_{eq}^k \right) \tag{27}$$

Where the scaled equivalent slip is defined as,

$$\sigma_{eq}^k = \frac{\mu_k(F_z) \cdot F_z}{C_{Fk}(F_z)} \sigma. \tag{28}$$

and the magnitude of the wheel-slip vector of a single wheel is given by,

$$\sigma_{ij} = \sqrt{{\sigma_{xij}}^2 + {\sigma_{y_{ij}}}^2}. \tag{29}$$

The theoretical wheel slip σ_{kij} is defined by equations 30 and 31 [30].

$$\sigma_{xij} = \frac{\omega_{ij} R_e - v_{xij}}{\omega_{ij} R_e} \tag{30}$$

$$\sigma_{y_{ij}} = -\frac{v_{y_{ij}}}{\omega_{ij} R_e} \tag{31}$$

Where the translational velocities of the wheel centers each wheel centers, v_{xij} and $v_{y_{ij}}$, are given by,

$$\begin{bmatrix} {}^{w}v_{x\mathrm{fl}} \\ {}^{w}v_{y\mathrm{fl}} \end{bmatrix} = \begin{bmatrix} \cos\delta_{\mathrm{fl}} & \sin\delta_{\mathrm{fl}} \\ -\sin\delta_{\mathrm{fl}} & \cos\delta_{\mathrm{fl}} \end{bmatrix} \begin{bmatrix} 1 & 0 & -w_f \\ 0 & 1 & l_f \end{bmatrix} \begin{bmatrix} v_x & v_y & \dot{\psi} \end{bmatrix}^{\mathrm{T}} \tag{32}$$

Therefore, the tire force vector can be written as a function of the full state vector $\mathbf{x} = [v_x,\, v_y,\, \dot{\psi},\, \omega_{\mathrm{fl}},\, \omega_{\mathrm{fr}},\, \omega_{\mathrm{rl}},\, \omega_{\mathrm{rr}}]^{\mathrm{T}}$, i.e., ${}^{\mathrm{W}}\mathbf{F} = \mathbf{f}(\mathbf{x})$ which will be used in the subsequent sections on controller design and control effectiveness.

4. Controller Design

This chapter initially discusses the basic structure of the control system and its individual parts in separate sections. The concluding section provides a description of the envelope protection system and the yaw-rate set-point generator.

4.1. Cascaded control structure

The basic control structure consists of a cascade of feedback loops controlling respectively the vehicle side-slip angle, the yaw-rate, and the prop-shaft velocity. A cascaded control structure greatly simplifies the design of an inversion based controller, which would otherwise involve the repeated differentiation and subsequent inversion of equations 10, 20a and 20b, including the tire model. The nature of INDI ordinarily requires a cascaded structure if the control input does not directly appear in the time derivative of the controlled output, further reinforcing the proposed choice of control system structure.

A prerequisite for the use of a cascaded control structure is the existence of naturally occurring time scales in the controlled dynamical system [34] or the ability to sufficiently speed-up the inner-loops by increasing the associated gains [35]. Time-scale separation in combination with inversion techniques has been used successfully in aircraft control where the existence of different time scales between the aerodynamic angles and the angular rates [34,36] or the attitude angles and angular rates [23], is well-established. Most of the references on automotive stability control included here assume that the dynamics associated with controlling the wheel forces are fast enough to be separated from the yaw dynamics or can be neglected entirely [4,11–15,37]. The bandwidth separation is assumed to be large enough to adopt a cascaded control structure.

4.2. Prop-Shaft Velocity Controller

The low level controller incorporates an INDI control scheme based on the equations that describe the dynamics of the power-train (20a). Combining the front and rear prop-shaft dynamics in a single equation, neglecting the friction losses T_L and linearizing around $\boldsymbol{\omega}_{\mathrm{p}0}$ results in,

$$\dot{\boldsymbol{\omega}}_\mathrm{p} = \dot{\boldsymbol{\omega}}_{\mathrm{p}0} + \mathbf{J} R_\mathrm{e} \left.\frac{\partial \mathbf{F}_x}{\partial \mathbf{x}}\right|_{(\mathbf{x}_0,\, \mathbf{T}_{\mathrm{in}0})} (\mathbf{x} - \mathbf{x}_0) + \mathbf{J} K_\mathrm{t} (T_\mathrm{in} - T_{\mathrm{in}0}). \tag{33}$$

Where ${}^{\mathrm{W}}\mathbf{F} = \begin{bmatrix} {}^{w}F_{x\mathrm{fl}} & \dots & {}^{w}F_{x_\mathrm{rr}} \end{bmatrix}^{\mathrm{T}}$ denotes the tire-force vector in x direction, the prop-shaft velocity vector is given by $\boldsymbol{\omega}_\mathrm{p} = [\omega_{\mathrm{p}\mathrm{f}},\, \omega_{\mathrm{p}\mathrm{r}}]^{\mathrm{T}}$ and the drive torque vector $T_\mathrm{in} = [T_\mathrm{inf},\, T_\mathrm{inr}]^{\mathrm{T}}$. Diagonal matrix K_t has the transmission of the front, and rear drive train on its diagonal and the inertia matrix is defined as,

$$\mathbf{J} = \begin{bmatrix} (J_\mathrm{eq} + 2J_\mathrm{w} + J_\mathrm{c})_\mathrm{f} & 0 \\ 0 & (J_\mathrm{eq} + 2J_\mathrm{w} + J_\mathrm{c})_\mathrm{r} \end{bmatrix}. \tag{34}$$

Lastly, $\dot{\boldsymbol{\omega}}_{\mathrm{p}0}$ denotes the current prop-shaft angular acceleration and is substituted with a measurement or estimate.

By equating the virtual ν_ω to the state derivative $\dot{\omega}_\mathrm{p}$, equation 33 can be used to find a linear differential relation between the controlled variable ω_p and ν_ω. Furthermore, if the control rate is sufficiently high, the time-scale separation principle dictates that the term containing the linearized tire model can be neglected as the change in prop-shaft velocity over each time-step becomes negligible compared to the changes in the control input, i.e. $(\boldsymbol{\omega}_\mathrm{p} - \boldsymbol{\omega}_{\mathrm{p}0}) \approx \mathbf{0}$. The resulting relation can be solved for the control

increment ΔT_p leading to,

$$\Delta T_\mathrm{p} = K_\mathrm{t}^{-1}\mathbf{J}^{-1}\left(\nu_\omega - \dot{\boldsymbol{\omega}}_{\mathrm{p}0}\right) \tag{35}$$

Torque increment ΔT_p represents the torque increment required to reach the desired propshaft acceleration set by the virtual control. The commanded torque is therefore given by,

$$T_\mathrm{pc} = T_\mathrm{pf} + \Delta T_\mathrm{p}. \tag{36}$$

Where T_pf is the current measured or estimated current torque set-point.

If Equation 35 and 36 are applied to 33 it is approximately linearized. In other words, under the aforementioned assumptions an approximate linear differential relation exists between the prop-shaft velocity and the virtual control, i.e.,

$$\dot{\omega}_\mathrm{p} \approx \nu_\omega. \tag{37}$$

Therefore, a simple linear controller suffices to control the system with ν_ω. In the prop-shaft velocity loop, this linear controller is a simple PID.

Note that the approximate linearization does not depend on the tire-forces and therefore does not necessitate the inversion of a complex tire-model as required by NDI [38], greatly simplifying the inversion process. Furthermore, matrix $\mathbf{J}$ and K_t depend solely on the transmission ratios, equivalent inertias and the current transmission gain, but are otherwise constant.

However, Equation 35 may require differentiating a measurement or estimate of the prop-shaft velocity if no direct prop-shaft acceleration measurement is available. To facilitate the differentiation of a potentially noisy signal, the prop-shaft velocity measurement is filtered by a second order low-pass filter, $\mathbf{H}(z)$. The same filter is applied to the measurement or estimate of the current control input in order to guarantee the stability of the system [39].

4.2.1. Pseudo Control Hedge

The prop-shaft velocity controller further incorporates Psuedo Control Hedging (PCH), a technique first introduced in the context of Model Reference Adaptive Control (MRAC) to address the problems associated with model adaptation in the presence of actuator dynamics and (rate-) saturation [40]. A reference model is negated with the error between the commanded and actual virtual or pseudo control signals such that the reference signal more closely resembles the system dynamics permissible by the actuator. Psuedo Control Hedging (PCH) has also been demonstrated as advantageous outside the context of adaptive control in conjunction with NDI as a means for flight envelope protection [41]. PCH further improved controller performance when used with INDI in the presence actuator dynamics and saturation [42].

In this controller PCH is used to compensate for the torque and power limits of both power-units of the vehicle. The PCH compensated reference dynamics of the first order reference model are given by equation 38 [41].

$$\dot{\mathbf{x}}_\mathrm{r} = K_\mathrm{p}(\mathbf{x}_\mathrm{c} - \mathbf{x}_\mathrm{r}) - \boldsymbol{\nu}_\mathrm{h}. \tag{38}$$

Where the diagonal gain matrix K_p is chosen such that the time constant of the first

order reference model reflects the desired dynamics of the controlled system. The PCH signal ν_{h}, when used in conjunction with INDI, is simply given by equation 39 [42].

$$\boldsymbol{\nu}_{\mathrm{h}} = \mathbf{G}(\mathbf{u}_{\mathrm{c}} - \mathbf{u}_{\mathrm{a}}) \tag{39}$$

Where $\mathbf{u}_{\mathrm{c}} - \mathbf{u}_{\mathrm{a}}$ corresponds to the difference between the commanded and actual actuator position. In the prop-shaft velocity controller this amounts to the delta between the commanded and the actual torque. An accurate estimate of prop-shaft torque is assumed to be available from either a power-train model or a direct measurement. Consequently, the dynamics of the implemented reference model are given by,

$$\dot{\boldsymbol{\omega}}_{\mathrm{ref}} = K_{\mathrm{p}}(\boldsymbol{\omega}_{\mathrm{c}} - \boldsymbol{\omega}_{\mathrm{ref}}) - \mathbf{G}_{\omega}(T_{\mathrm{c}} - T_{\mathrm{a}}) \tag{40}$$

Where $\boldsymbol{\omega}_{\mathrm{c}}$ and $\boldsymbol{\omega}_{\mathrm{ref}}$ are the commanded and filtered reference prop-shaft velocities respectively.

Figure 2 provides a schematic of the control structure of the prop-shaft velocity controller including the PCH. The block $\mathbf{E}(z)$ represents the actuator dynamics, comprising the behavior of both the electric motor in the front and the combustion engine in the rear of the car, which are assumed to be known. Block **VD** corresponds to the remaining vehicle dynamics and the effectiveness $\mathbf{J}K_{\mathrm{t}}$ is abbreviated as $\mathbf{G}_{\omega}$. Note that subscripts have been dropped where does not cause any ambiguity.

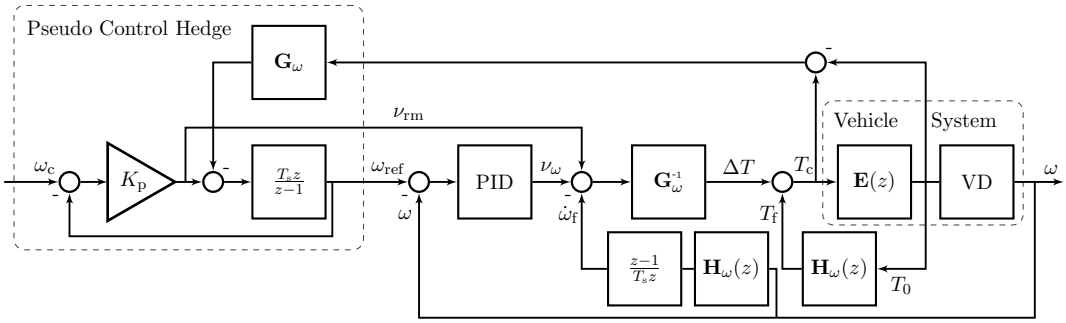

Figure 2. A schematic of the prop-shaft velocity controller including the Psuedo Control Hedging (PCH)

4.3. Yaw Rate Control

The feedback loop enclosing the prop-shaft loop controls the vehicle yaw-rate. The equation describing the yaw-rate dynamics (10) reveals that constructing a controller based on NDI would require the full inversion of a tire-model. Moreover, the control variable $\boldsymbol{\omega}_{\mathrm{s}}$ does not appear affine in 10, i.e., the controlled system has the more general form given in equation 1. Determining the control input once the virtual control is known, would therefore require solving a nonlinear optimization problem. The problem can be simplified by linearizing the corresponding equations [9] or by neglecting the nonlinear nature of tire model by using the tire forces as pseudo control inputs and solving for the tire-slips at a later time [10].

However, these methods only result in approximate feedback linearizations and are characterized by the characteristic shortcomings of NDI or Feedback Linearization (FBL) [26]. A different approach would be to linearize the system before inverting the

equations, corresponding to INDI [23]. Linearizing equation 10 results in the approximate yaw-rate equations in matrix form.

$$\ddot{\psi} \approx \ddot{\psi}_0 + \mathbf{M}^{-1}{}_{3,3}\mathbf{E}_{3,*}\mathbb{T}_{\mathrm{B,W}}\left[\left.\frac{\partial \mathbf{F}}{\partial \mathbf{x}}\right|_{(\mathbf{x}_0,\,\mathbf{u}_0)}(\mathbf{x}-\mathbf{x}_0) + \left.\frac{\partial \mathbf{F}}{\partial \boldsymbol{\omega}_\mathrm{p}}\right|_{(\mathbf{x}_0,\,\mathbf{u}_0)}\left(\boldsymbol{\omega}_\mathrm{p}-\boldsymbol{\omega}_{\mathrm{p}0}\right)\right] \tag{41}$$

Where $\ddot{\psi}_0$, the yaw-acceleration at the time of linearization, can be substituted with a measurement or estimate of the state derivative. The subscripts accompanying matrix $\mathbf{M}$ and $\mathbf{E}$ refer to the rows and columns corresponding to the derivative of the yaw-rate. Lastly, $\frac{\partial \mathbf{F}}{\partial \mathbf{x}}$ and $\frac{\partial \mathbf{F}}{\partial \boldsymbol{\omega}_\mathrm{p}}$ denote the partial derivatives of the tire-forces towards the state vector and the prop-shaft velocities respectively.

Analogous to the inversion of the prop-shaft velocity loop, assuming that the control rate is sufficiently high, such that the state increment over one sample time is much smaller than the control increment, equation 41 simplifies to,

$$\ddot{\psi} \approx \ddot{\psi}_0 + \mathbf{M}^{-1}{}_{3,3}\mathbf{E}_{3,*}\mathbb{T}_{\mathrm{B,W}}\frac{\partial \mathbf{F}}{\partial \boldsymbol{\omega}_\mathrm{p}}\Delta\boldsymbol{\omega}_\mathrm{p} \tag{42}$$

$$\ddot{\psi} \approx \ddot{\psi}_0 + \mathbf{G}_\psi \Delta\boldsymbol{\omega}_\mathrm{p} \tag{43}$$

Where the control effectiveness is abbreviated as $\mathbf{G}_\psi$. Section 5 treats the calculation of the control effectiveness in more detail and provides a method for incorporating the effect of load-transfers in $\mathbf{G}_\psi$ directly.

Equating the virtual control ν_ψ to the state derivative $\ddot{\psi}$ and solving for $\Delta\boldsymbol{\omega}_\mathrm{p}$ yields a mapping between $\Delta\boldsymbol{\omega}_\mathrm{p}$ and ν_ψ which once applied to equation 10 results in an approximate linear differential relation between $\ddot{\psi}$ and ν_ψ. A simple linear controller then suffices to control the system with ν_ψ.

$$(\nu_\psi - \ddot{\psi}_0) = \mathbf{G}_\psi \Delta\boldsymbol{\omega}_\mathrm{p} \tag{44}$$

$$\hat{\nu} = \mathbf{G}_\psi \Delta\boldsymbol{\omega}_\mathrm{p} \tag{45}$$

However, the columns of $\mathbf{G}_{\dot{\psi}}$ are not linearly independent and therefore equation 45 may not have a unique solution in $\Delta\boldsymbol{\omega}_\mathrm{p}$. The problem of finding a suitable set of control commands that satisfy equation 45 is commonly referred to as *control allocation* and is treated in the next section

4.3.1. Control Allocation

A typical approach to finding a distinct solution to the control allocation problem 45 is to simultaneously minimize a secondary objective such as the deviation from some desired input [43]. In conjunction with an incremental control law, the deviation to some desired control increment $\Delta\boldsymbol{\omega}_{\mathrm{p_d}}$ can be minimized instead. Where $\Delta\boldsymbol{\omega}_{\mathrm{p_d}}$ may be chosen such that it reflects some feed-forward torque or slip distribution associated with maximizing the lateral acceleration as described in [18].

If the l_2-norm is used as a measure for the error between the control input and a

desired value, the control allocation problem can be cast into,

$$\underset{\Delta\boldsymbol{\omega}_\mathrm{p}}{\arg\min} \left\| W_\mathrm{s} \left(\Delta\boldsymbol{\omega}_\mathrm{p} - \Delta\boldsymbol{\omega}_\mathrm{d} \right) \right\|_2 + \gamma \left\| W_v \left(\mathbf{G}_\psi \Delta\boldsymbol{\omega}_\mathrm{p} - \hat{\nu} \right) \right\|_2 \tag{46a}$$

$$\text{subject to } \Delta\underline{\boldsymbol{\omega}_\mathrm{p}} \leq \Delta\boldsymbol{\omega}_\mathrm{p} \leq \Delta\overline{\boldsymbol{\omega}_\mathrm{p}} \tag{46b}$$

Where the primary objective (45) is augmented to a secondary objective using a parameter γ reflecting the relative importance of the two terms. Weighting matrix W_s and W_v prioritize the different actuators and the rows of the primary objective respectively. Lastly, equation 46b constrains the solution such that it does not violate any actuator rate or position limits.

Redistributed Pseudo Inverse (RPI) [44] or Cascaded Generalized Inverse (GCI) [45] methods, which iteratively modify the exact solution to a similarly defined equality constraint problem [46,47], are widely adopted within control allocation algorithms due to their simplicity and low computational burden [43]. However, these methods do not always converge to the optimal solution as demonstrated in [43,47]. Active-set methods do not suffer from this inherent problem and have been demonstrated to converge to the optimal solution in a finite number of steps [48]. Therefore, a Weighted Least Squares (WLS) control allocation algorithm, an active-set method described by [47] was incorporated into the yaw-rate controller.

The actuator rate limits are related to the maximum and minimum realizable prop-shaft rotational accelerations and the sample time t_s as,

$$\Delta\overline{\omega_{\mathrm{p_r}}} = \dot{\omega}_{\mathrm{s}\max}(T_\mathrm{max}) \cdot t_s \tag{47}$$

$$\Delta\underline{\omega_{\mathrm{p_r}}} = \dot{\omega}_{\mathrm{s}\min}(T_\mathrm{min}) \cdot t_s \tag{48}$$

Where $\Delta\overline{\omega_{\mathrm{p_r}}}$ and $\Delta\underline{\omega_{\mathrm{p_r}}}$ depend on the maximum available drive torque and engine drag respectively. Furthermore, prop-shaft velocities that saturate the longitudinal slip on one of the wheels are taken as absolute limits are transcribed to an incremental form by subtracting the current prop-shaft velocity as,

$$\Delta\overline{\omega_{\mathrm{p}\sigma}} = \max\left(\omega_{\mathrm{s}\,\mathrm{sat}}(\sigma_{xij}, \sigma_{xij})\right) - \omega_{\mathrm{p}0} \tag{49}$$

$$\Delta\underline{\omega_{\mathrm{p}_\sigma}} = \min\left(\omega_{\mathrm{s}\,\mathrm{sat}}(\sigma_{xij}, \sigma_{xij})\right) - \omega_{\mathrm{p}0} \tag{50}$$

Figure 3 provides a schematic of the yaw-rate loop described in this section. Analogous to the controller described in the previous section, the measured yaw-rate and prop-shaft velocity are filtered using the same second order low-pass filter which reflects the bandwidth of the yaw-rate response of the vehicle. Lastly, the block that is responsible for control allocation is denoted by $\mathbf{G}^+_{\psi}$.

4.4. Side-Slip Control

The outer-loop of the control system is formed by a feedback loop and dynamic inversion of the vehicle side-slip angle. In contrast to the prop-shaft velocity and yaw-rate loops, the side-slip angle inversion can be made exact as demonstrated by [23]. A prerequisite for both the feedback loop and the dynamic inversion described below is an accurate measurement or estimate of the side-slip angle. This information is assumed to be available.

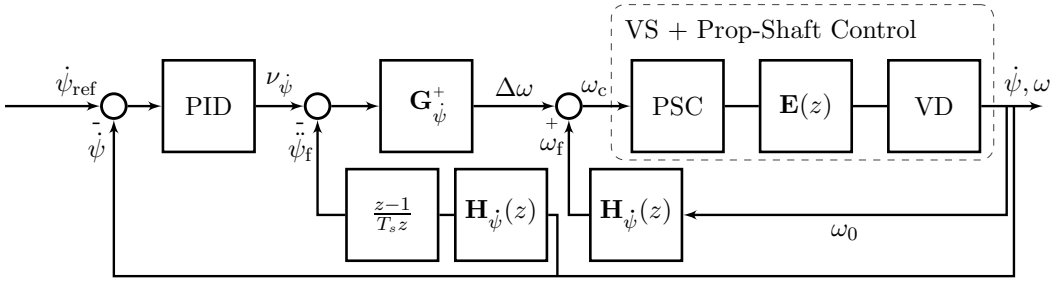

Figure 3. Schematic of the yaw-rate controller

The side-slip angle for non-planar motion is given by,

$$\beta = \arcsin\left(\frac{v_y}{V}\right). \tag{51}$$

Which reduces to equation 52 if the motion of the vehicle is assumed to be planar.

$$\beta = \arctan\left(\frac{v_y}{v_x}\right) \tag{52}$$

Taking the derivative of equation 52 results in,

$$\dot{\beta} = \frac{v_x\dot{v}_y - v_y\dot{v}_x}{v_x^2\left(1 + v_y^2/v_x^2\right)} \tag{53}$$

$$\dot{\beta} = \frac{v_x\dot{v}_y - v_y\dot{v}_x}{V} \tag{54}$$

Once more assuming planar motion, the derivatives of the body velocities are given by equations 55b.

$$\dot{v}_x = A_x + v_y\dot{\psi} \tag{55a}$$

$$\dot{v}_y = A_y - v_x\dot{\psi} \tag{55b}$$

Where A_x and A_y denote the longitudinal and lateral specific force respectively. Substituting equations 55b into equation 54 gives,

$$\dot{\beta} = \underbrace{\frac{A_x v_y - A_y v_x}{V}}_{a_\beta(\mathbf{x},\dot{\mathbf{x}})} + \underbrace{-1}_{b_\beta}\cdot\dot{\psi} \tag{56}$$

If the side-slip derivative is equated to the virtual control and the yaw-rate in equation 56 is treated as control input, it may be inverted to linearize the side-slip dynamics leading to Equation 57.

$$\dot{\psi} = -1\cdot\left(\nu_\beta - \frac{A_x v_y - A_y v_y}{V}\right) \tag{57}$$

Figure 4 provides a schematic of the side-slip angle feedback loop. The linear part of the controller is made up of a simple gain K_β however an integrator term might be

appropriate if the estimate of the lateral velocity proves insufficiently accurate.

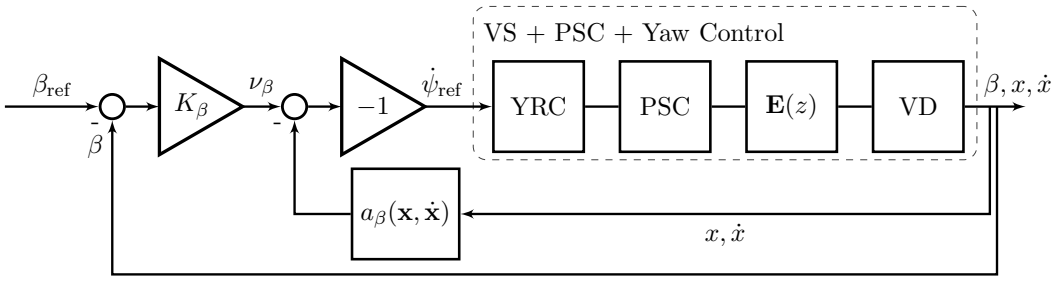

Figure 4. Schematic of the outer side-slip angle inversion loop

4.5. Envelope Protection and Yaw-Rate Set-Point

An envelope protection scheme is used to ensure the vehicle does not leave the stable regions of the state space. The stability of the planar vehicle model can be analyzed graphically inside the side-slip and side-slip-velocity ($\beta - \dot{\beta}$) phase-plane [49] or the side-slip and yaw-rate ($\beta - \dot{\psi}$) phase-plane [21,22]. The ($\beta - \dot{\psi}$) plane reveals that both the maximum yaw-rate and vehicle-side slip are important targets for vehicle stability augmentation systems. The stable region can be approximated using a maximum overall yaw-rate and the vehicle side-slip angle corresponding to the maximum allowable side-slip on the rear axle [21]. Furthermore, in some circumstances it may be appealing to limit lateral tire usage to some degree in order to reduce tire wear and possibly some of the driver workload associated with driving the vehicle at its limits. However, an experienced driver may consider the side-slip bounds too restrictive and looser constraints that allow the driver to push the rear axle past the maximum slip angle may be preferred. Equation 58 gives the bounds on the yaw-rate as adopted from [21].

$$\dot{\psi}_{\max} = \begin{cases} \frac{(F_{y\,\mathrm{f}})_{\max}(1+l_\mathrm{r}/l_\mathrm{f})}{v_x} & \text{if } (F_{y\mathrm{f}})_{\max} \leq \frac{l_\mathrm{r}}{l_\mathrm{f}}(F_{y\mathrm{r}})_{\max} \\ \frac{(F_{y\,\mathrm{r}})_{\max}(1+l_\mathrm{r}/l_\mathrm{f})}{v_x} & \text{if } (F_{y\mathrm{f}})_{\max} > \frac{l_\mathrm{r}}{l_\mathrm{f}}(F_{y\mathrm{r}})_{\max} \end{cases} \tag{58}$$

Where $(F_{y\mathrm{f}})_{\max}$ and $(F_{y\mathrm{f}})_{\max}$ denote the front and rear lateral force potentials respectively. A maximum yaw-rate exists for both directions of a turn and will be denoted by $\dot{\psi}_{\max}$ and $\dot{\psi}_{\min}$. The bounds on the side-slip angle can be approximated by the linearized slip-angle at the rear wheels,

$$\beta_{\max} = \alpha_{\max} + l_\mathrm{r}\dot{\psi} \tag{59}$$

$$\beta_{\min} = \alpha_{\min} + l_\mathrm{r}\dot{\psi} \tag{60}$$

Where the maximum and minimum values correspond to the outside wheel and are determined using the tire-model described in section 3 and the current longitudinal slips.

The side-slip inversion and cascaded nature of the control system allows the bounds on both the side-slip and the yaw-rate to be combined in a straightforward manner. If the reference of the side-slip angle inversion is set to one of the side-slip angle bounds, the output represents the yaw-rate necessary to reach this bound as if the associated

dynamics behave like a simple integrator. Therefore, the output of the side-slip angle inversion can be interpreted as a second set of bounds on the yaw-rate that prevent the rear axle side-slip from reaching undesirable levels. Using equation 57 the new bounds can simply be expressed as,

$$\dot{\boldsymbol{\psi}}_{\beta} = -1 \cdot \left(K_{\beta} \mathbf{e}_{\beta} - \frac{A_x v_y - A_y v_y}{V} \right) \tag{61}$$

Where $\mathbf{e}_{\beta}$ is given by,

$$\mathbf{e}_{\beta} = \begin{bmatrix} \beta_{\max} - \beta_0 \\ \beta_{\min} - \beta_0 \end{bmatrix} \tag{62}$$

The translated side-slip angle bounds are now straightforwardly related to maximum yaw-rate from equation 58 and the current yaw-rate through equation 63. This comparison leads to a controller that does not act inside the safe envelope but tries to intervene as soon as the yaw-rate exceeds any of the bounds described previously.

$$\dot{\psi}_r = \min \left(\max \left(\dot{\psi}_0,\ \dot{\psi}_{lb} \right),\ \dot{\psi}_{ub} \right) \tag{63}$$

The lower bound on the yaw-rate is given by minimum value of the translated side-slip bounds and the minimum attainable value of the steady state yaw-rate (64a). The upper bound on the yaw-rate is defined similarly (64b).

$$\dot{\psi}_{lb} = \min \left(\dot{\boldsymbol{\psi}}_{\beta},\ \dot{\psi}_{\min} \right) \tag{64a}$$

$$\dot{\psi}_{ub} = \max \left(\dot{\boldsymbol{\psi}}_{\beta},\ \dot{\psi}_{\max} \right) \tag{64b}$$

Further note that the gain K_{β}, scales the translated side-slip angle boundaries, with smaller values leading to tighter bounds and higher values to a controller that will intervene later. [21,22] show that the side-slip angle bounds are less critical and therefore K_{β} should be chosen such that the controller does not prevent the driver from reaching maximum lateral tire usage as quickly as possible, possibly allowing for some overshoot.

The current yaw-rate $\dot{\psi}_0$, can be replaced by a set-point from a reference model resulting in a model following controller that acts inside the safe envelope. Equation 65 provides a frequently applied set-point generator derived from the linear-bicycle model [18].

$$\frac{\dot{\psi}_{\mathrm{ss}}}{\delta} = \frac{v_x}{l + -\frac{m}{l} \frac{l_f C_{\alpha \mathrm{f}} - l_r C_{\alpha \mathrm{r}}}{C_{\alpha \mathrm{f}} C_{\alpha \mathrm{r}}} v_{\mathrm{x}}^2} \tag{65}$$

Where $C_{\alpha \mathrm{f}}$ and $C_{\alpha \mathrm{r}}$ denote the lateral slip-stifness of the front and rear axle respectively.

Figure 5 provides a high level overview of the entire control system.

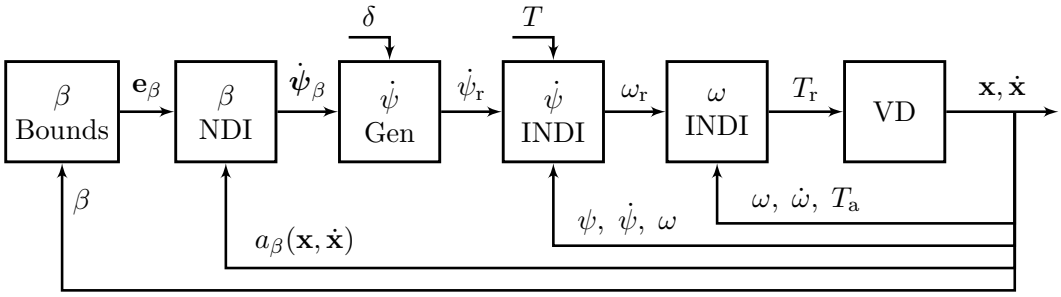

Figure 5. High level overview of the complete control system6

5. Yaw-Rate Loop Control Effectiveness

The control effectiveness in the yaw-rate loop is defined as the partial derivative of the yaw-rate state-equation towards the prop-shaft velocities $\omega_\mathrm{p} = [\omega_{\mathrm{pf}}, \omega_{\mathrm{pr}}]^\mathrm{T}$ and can conveniently be written in matrix form using equation 10.

$$\mathbf{G}_{\dot{\psi}} = \frac{\partial \ddot{\psi}}{\partial \boldsymbol{\omega}_\mathrm{p}} = \frac{\partial \ddot{\psi}}{\partial \boldsymbol{\omega}} \frac{\partial \boldsymbol{\omega}}{\partial \boldsymbol{\omega}_\mathrm{p}} = \mathbf{M}^{-1}{}_{3,3} \mathbf{E}_{3,*} \mathbb{T}_{\mathrm{B,W}} \frac{\partial \mathbf{F}}{\partial \boldsymbol{\omega}} \frac{\partial \boldsymbol{\omega}}{\partial \boldsymbol{\omega}_\mathrm{p}} \tag{66}$$

Where the vector $\mathbf{F}$ denotes the tire-forces in the wheel frame ${}^\mathrm{W}\mathbf{F}$, $\boldsymbol{\omega} = [\omega_{\mathrm{fl}}, \omega_{\mathrm{fr}}, \omega_{\mathrm{rl}}, \omega_{\mathrm{rr}}]^\mathrm{T}$ is the wheel speed vector and $\boldsymbol{\omega}_\mathrm{p} = [\omega_{\mathrm{pf}}, \omega_{\mathrm{pr}}]$ contains the prop-shaft velocities. From equations 19a - 19b, 20a - 20b and the cases described in section 3, it is clear that $\frac{\partial \boldsymbol{\omega}}{\partial \boldsymbol{\omega}_\mathrm{p}}$ does not have a closed form solution. The estimation of this derivative will be treated in a later section, after finding an expression for $\frac{\partial \mathbf{F}}{\partial \boldsymbol{\omega}}$.

5.1. Tire force Jacobian

That traction and braking forces create yaw-moments through load-transfers is well-known. In fact, [11] proposes Direct Yaw-Moment Control (DYC) as a means to compensate for the moments created during accelerating and braking but use a crude estimation. However, Direct Yaw-Moment Control (DYC) implies that each wheel can be actuated individually and as a result, the magnitude of the attainable yaw-moments is large. The effect of load-transfers on the control moments is therefore often considered relatively small and slow in comparison and is usually neglected [27]. The yaw-moments associated with torque increments on a LSD are much smaller and therefore the effect of longitudinal load-transfers has to be incorporated into the control effectiveness.

Assuming steering angles affect the longitudinal components of the wheel forces only marginally, the tire force vector can be expressed implicitly by combining equation 27 and the longitudinal component of the instantaneous load-transfer model (17), resulting in,

$$\bar{\mathbf{F}} = \bar{\mathbf{f}}(\boldsymbol{\omega}, h(\bar{\mathbf{F}})). \tag{67}$$

Where the longitudinal component of the load-transfer model is given by,

$$\mathbf{F}_\mathrm{z} = h(\bar{\mathbf{F}}) = [-\Delta W_x, -\Delta W_x, \Delta W_x, \Delta W_x]^\mathrm{T}, \tag{68}$$

and the tire force vector is re-partitioned into,

$$\bar{\mathbf{F}} = \left[F_{x_{\mathrm{fl}}}, \ldots, F_{x_{\mathrm{rr}}}, F_{y_{\mathrm{fl}}}, \ldots, F_{y_{\mathrm{rr}}}\right]^{\mathrm{T}}. \tag{69}$$

The dependencies of F_{xij} and $F_{y_{ij}}$ on v_{xij} and $v_{y_{ij}}$ have been omitted for reasons of clarity.

Defining the wheel-speed vector $\boldsymbol{\omega}$ as the independent variable, equation 67 can be differentiated implicitly to find the derivative of the tire forces towards the wheel slips incorporating the effect of changing normal loads. Resulting in:

$$\frac{\partial \bar{\mathbf{F}}}{\partial \boldsymbol{\omega}} = \frac{\partial \bar{\mathbf{f}}}{\partial \boldsymbol{\omega}} + \frac{\partial \bar{\mathbf{f}}}{\partial \mathbf{F}_{\mathrm{z}}} \frac{\partial \mathbf{F}_{\mathrm{z}}}{\partial \bar{\mathbf{F}}} \frac{\partial \bar{\mathbf{F}}}{\partial \boldsymbol{\omega}} \tag{70}$$

Solving for $\frac{\partial \bar{\mathbf{F}}}{\partial \boldsymbol{\omega}}$ gives,

$$\frac{\partial \bar{\mathbf{F}}}{\partial \boldsymbol{\omega}} = \left(I - \frac{\partial \bar{\mathbf{f}}}{\partial \mathbf{F}_{\mathrm{z}}} \frac{\partial \mathbf{F}_{\mathrm{z}}}{\partial \bar{\mathbf{F}}}\right)^{-1} \frac{\partial \bar{\mathbf{f}}}{\partial \boldsymbol{\omega}} \tag{71}$$

Where the term $\frac{\partial \bar{\mathbf{f}}}{\partial \boldsymbol{\omega}}$ corresponds to force the Jacobian without load-transfer effects. The matrix between parentheses, from now on referred to as M, accounts for the changes in the normal load distribution following a change in wheel speed.

Due to the partitioning of $\bar{\mathbf{F}}$, the matrix $\frac{\partial \bar{\mathbf{f}}}{\partial \mathbf{F}_{\mathrm{z}}}$ is made up of two diagonal matrices.

$$\frac{\partial \bar{\mathbf{f}}}{\partial \mathbf{F}_{\mathrm{z}}} = \begin{bmatrix} \frac{\partial \mathbf{f}_x}{\partial \mathbf{F}_{\mathrm{z}}} \\ \frac{\partial \mathbf{f}_y}{\partial \mathbf{F}_{\mathrm{z}}} \end{bmatrix} \tag{72}$$

Where,

$$\begin{aligned} \frac{\partial \mathbf{f}_x}{\partial \mathbf{F}_{\mathrm{z}}} &= \mathrm{diag}\begin{pmatrix} \frac{\partial F_{x\,\mathrm{fl}}}{\partial F_{z\,\mathrm{fl}}} & \frac{\partial F_{x\,\mathrm{fr}}}{\partial F_{z\,\mathrm{fr}}} & \frac{\partial F_{x\,\mathrm{rl}}}{\partial F_{z\,\mathrm{rl}}} & \frac{\partial F_{x\,\mathrm{rr}}}{\partial F_{z\,\mathrm{rr}}} \end{pmatrix} \quad \text{and} \\ \frac{\partial \mathbf{f}_y}{\partial \mathbf{F}_{\mathrm{z}}} &= \mathrm{diag}\begin{pmatrix} \frac{\partial F_{y\,\mathrm{fl}}}{\partial F_{z\,\mathrm{fl}}} & \frac{\partial F_{y\,\mathrm{fr}}}{\partial F_{z\,\mathrm{fr}}} & \frac{\partial F_{y\,\mathrm{rl}}}{\partial F_{z\,\mathrm{rl}}} & \frac{\partial F_{y\,\mathrm{rr}}}{\partial F_{z\,\mathrm{rr}}} \end{pmatrix}. \end{aligned}$$

Similarly, the partial derivative $\frac{\partial \mathbf{F}_{\mathrm{z}}}{\partial \bar{\mathbf{F}}}$ can be expressed in block-form as,

$$\frac{\partial \mathbf{F}_{\mathrm{z}}}{\partial \bar{\mathbf{F}}} = \begin{bmatrix} \frac{\partial \mathbf{F}_{\mathrm{z}}}{\partial \mathbf{F}_x} & \mathbf{0} \end{bmatrix}. \tag{73}$$

The block matrix $\frac{\partial \mathbf{F}_{\mathrm{z}}}{\partial \mathbf{F}_x}$ can be simplified further by applying the chain rule a second time and using the specific force as an intermediate variable, resulting in,

$$\frac{\partial \mathbf{F}_{\mathrm{z}}}{\partial \mathbf{F}_x} = \frac{\partial \mathbf{F}_{\mathrm{z}}}{\partial A_x} \frac{\partial A_x}{\partial \mathbf{F}_x}. \tag{74}$$

Where,

$$\frac{\partial \mathbf{F}_{\mathrm{z}}}{\partial A_x} = \begin{bmatrix} -\frac{\partial \Delta W_x}{\partial A_x} \\ -\frac{\partial \Delta W_x}{\partial A_x} \\ \frac{\partial \Delta W_x}{\partial A_x} \\ \frac{\partial \Delta W_x}{\partial A_x} \end{bmatrix} \quad \text{and} \quad \frac{\partial A_x}{\partial \mathbf{F}_x}^{\mathrm{T}} = \frac{1}{m} \begin{bmatrix} 1 \\ 1 \\ 1 \\ 1 \end{bmatrix}. \tag{75}$$

It follows from equations 72 - 73 that M can be written as,

$$M = \left(I - \frac{\partial \bar{\mathbf{f}}}{\partial \mathbf{F}_{\mathrm{z}}} \frac{\partial \mathbf{F}_{\mathrm{z}}}{\partial \bar{\mathbf{F}}} \right) = \begin{bmatrix} I - \frac{\partial \mathbf{f}_x}{\partial \mathbf{F}_{\mathrm{z}}} \frac{\partial \mathbf{F}_{\mathrm{z}}}{\partial A_x} \frac{\partial A_x}{\partial \mathbf{F}_x} & \mathbf{0} \\ -\frac{\partial \mathbf{f}_y}{\partial \mathbf{F}_{\mathrm{z}}} \frac{\partial \mathbf{F}_{\mathrm{z}}}{\partial A_x} \frac{\partial A_x}{\partial \mathbf{F}_x} & I \end{bmatrix} = \begin{bmatrix} A & \mathbf{0} \\ C & I \end{bmatrix} \tag{76}$$

Due to its structure, finding the inverse of matrix M is now relatively straightforward and is given by,

$$M^{-1} = \begin{bmatrix} A^{-1} & \mathbf{0} \\ -CA^{-1} & I \end{bmatrix} \tag{77}$$

The inverse of sub-matrix A can be found by noting that $\frac{\partial \mathbf{F}_z}{\partial A_x} \frac{\partial A_x}{\partial \mathbf{F}_x}$ is in fact the outer-product of two column vectors. This allows the application of the Sherman-Morrison Formula [50], which gives the inverse of the sum of an invertible matrix K and the vector product uv^{T}, in terms of K^{-1} and vectors u and v (78).

$$(K + uv^{\mathrm{T}})^{-1} = K^{-1} - \frac{K^{-1} u v^{\mathrm{T}} K^{-1}}{1 + v^{\mathrm{T}} K^{-1} u} \tag{78}$$

Application of equation 78 to the inverse of sub-matrix A leads to,

$$A^{-1} = \left(I - \frac{\partial \mathbf{f}_x}{\partial \mathbf{F}_{\mathrm{z}}} \frac{\partial \mathbf{F}_{\mathrm{z}}}{\partial A_x} \frac{\partial A_x}{\partial \mathbf{F}_x} \right)^{-1} = I + \frac{1}{|A|} \frac{\partial \mathbf{f}_x}{\partial \mathbf{F}_{\mathrm{z}}} \frac{\partial \mathbf{F}_{\mathrm{z}}}{\partial A_x} \frac{\partial A_x}{\partial \mathbf{F}_x} \tag{79}$$

Where the determinant of A is given by,

$$|A| = 1 - \frac{\partial A_x}{\partial \mathbf{F}_x} \frac{\partial \mathbf{f}_x}{\partial \mathbf{F}_{\mathrm{z}}} \frac{\partial \mathbf{F}_{\mathrm{z}}}{\partial A_x} \tag{80}$$

$$= \left(\frac{\partial F_{x\mathrm{fl}}}{\partial F_{z\mathrm{fl}}} + \frac{\partial F_{x\mathrm{fr}}}{\partial F_{z\mathrm{fr}}} - \frac{\partial F_{x\mathrm{rl}}}{\partial F_{z\mathrm{rl}}} - \frac{\partial F_{x\mathrm{rr}}}{\partial F_{z\mathrm{rr}}} \right) \frac{\partial \Delta W_x}{A_x} + 1 \tag{81}$$

Substituting the result for A^{-1} in $-CA^{-1}$ leads to,

$$-CA^{-1} = \frac{\partial \mathbf{f}_y}{\partial \mathbf{F}_{\mathrm{z}}} \frac{\partial \mathbf{F}_{\mathrm{z}}}{\partial A_x} \frac{\partial A_x}{\partial \mathbf{F}_x} \left(I + \frac{1}{|A|} \frac{\partial \mathbf{f}_x}{\partial \mathbf{F}_{\mathrm{z}}} \frac{\partial \mathbf{F}_{\mathrm{z}}}{\partial A_x} \frac{\partial A_x}{\partial \mathbf{F}_x} \right). \tag{82}$$

Factoring out $|A|$ and bringing $\frac{\partial \mathbf{F}_z}{\partial A_x}\frac{\partial A_x}{\partial \mathbf{F}_x}$ into the parentheses results in,

$$-CA^{-1} = \frac{1}{|A|}\frac{\partial \mathbf{f}_y}{\partial \mathbf{F}_z}\left(\frac{\partial \mathbf{F}_z}{\partial A_x}\frac{\partial A_x}{\partial \mathbf{F}_x} - \left[\frac{\partial \mathbf{F}_z}{\partial A_x}\frac{\partial A_x}{\partial \mathbf{F}_x}\frac{\partial A_x}{\partial \mathbf{F}_x}\frac{\partial \mathbf{f}_x}{\partial \mathbf{F}_z}\frac{\partial \mathbf{F}_z}{\partial A_x} + \frac{\partial \mathbf{F}_z}{\partial A_x}\frac{\partial A_x}{\partial \mathbf{F}_x}\frac{\partial \mathbf{f}_x}{\partial \mathbf{F}_z}\frac{\partial \mathbf{F}_z}{\partial A_x}\frac{\partial A_x}{\partial \mathbf{F}_x}\right]\right). \tag{83}$$

The term within brackets equates to zero, reducing equation 83 to,

$$-CA^{-1} = \frac{1}{|A|}\frac{\partial \mathbf{f}_y}{\partial \mathbf{F}_z}\frac{\partial \mathbf{F}_z}{\partial A_x}\frac{\partial A_x}{\partial \mathbf{F}_x}. \tag{84}$$

Matrix inverse M^{-1} is now given by equation 85.

$$M^{-1} = \begin{bmatrix} I + \frac{1}{|A|}\frac{\partial \mathbf{f}_x}{\partial \mathbf{F}_z}\frac{\partial \mathbf{F}_z}{\partial A_x}\frac{\partial A_x}{\partial \mathbf{F}_x} & \mathbf{0} \\ \frac{1}{|A|}\frac{\partial \mathbf{f}_y}{\partial \mathbf{F}_z}\frac{\partial \mathbf{F}_z}{\partial A_x}\frac{\partial A_x}{\partial \mathbf{F}_x} & I \end{bmatrix} \tag{85}$$

Similarly, $\frac{\partial \bar{\mathbf{F}}}{\partial \boldsymbol{\omega}}$ is straightforwardly expressed in terms of the partial derivatives of $\bar{\mathbf{f}}$ and $\mathbf{F}_z$ only (86).

$$\frac{\partial \bar{\mathbf{F}}}{\partial \boldsymbol{\omega}} = \begin{bmatrix} I + \frac{1}{|A|}\frac{\partial \mathbf{f}_x}{\partial \mathbf{F}_z}\frac{\partial \mathbf{F}_z}{\partial \mathbf{F}_x} & \mathbf{0} \\ \frac{1}{|A|}\frac{\partial \mathbf{f}_y}{\partial \mathbf{F}_z}\frac{\partial \mathbf{F}_z}{\partial \mathbf{F}_x} & I \end{bmatrix} \frac{\partial \bar{\mathbf{f}}}{\partial \boldsymbol{\omega}} \tag{86}$$

The partial derivatives, $\frac{\partial \bar{\mathbf{f}}}{\partial \boldsymbol{\omega}}$, $\frac{\partial \mathbf{f}_x}{\partial \mathbf{F}_z}$ and $\frac{\partial \mathbf{f}_y}{\partial \mathbf{F}_z}$ appearing in equation 86 can either be found analytically or through finite differences, depending on the type of tire-model that is used. In this work these derivatives are found through finite-differences.

The effect of changing lateral load-transfers can be included into the control effectiveness as well. However, these effects are inherently smaller than the longitudinal component discussed previously. The equation that gives the tire-force jacobian including the effect of both longitudinal and lateral load-transfers is given by equation

$$\frac{\partial \bar{\mathbf{F}}}{\partial \boldsymbol{\omega}} = \begin{bmatrix} A^{-1} & \mathbf{0} \\ \mathbf{0} & D^{-1} \end{bmatrix} \begin{bmatrix} I + \frac{P}{|\bar{M}|}\frac{\partial \mathbf{f}_x}{\partial \mathbf{F}_z}\frac{\partial \mathbf{F}_z}{\partial \mathbf{F}_y} & \frac{|A|}{|\bar{M}|}\frac{\partial \mathbf{f}_x}{\partial \mathbf{F}_z}\frac{\partial \mathbf{F}_z}{\partial \mathbf{F}_y} \\ \frac{|D|}{|\bar{M}|}\frac{\partial \mathbf{f}_y}{\partial \mathbf{F}_z}\frac{\partial \mathbf{F}_z}{\partial \mathbf{F}_x} & I + \frac{Q}{|\bar{M}|}\frac{\partial \mathbf{f}_y}{\partial \mathbf{F}_z}\frac{\partial \mathbf{F}_z}{\partial \mathbf{F}_x} \end{bmatrix} \frac{\partial \bar{\mathbf{f}}}{\partial \boldsymbol{\omega}} \tag{87}$$

5.1.1. Separating Slip and Load-Tranfer Effects

Looking at equation 86 and 87 reveals that tire-force Jacobian can be written as a sum of two matrices. Respectively $\frac{\partial \bar{\mathbf{f}}}{\partial \boldsymbol{\omega}}$ and a transformed version of this matrix, corresponding to the force Jacobian without load-transfer effects and a term that accounts for changing vertical wheel loads.

$$\tilde{\mathbf{G}}_{\dot{\psi}} = \mathbf{G}_{\dot{\psi}} + \hat{\mathbf{G}}_{\dot{\psi}} \tag{88}$$

This partition will be used to investigate the impact of load-transfers on the control effectiveness.

5.2. Ratio of wheel-speed increments

The partial derivative of the angular velocities of the wheels towards the prop-shafts velocities is approximated with the ratio of wheel-speed increments in response to a unit torque increment found using a linearized drive-train model (89).

$$\dot{\boldsymbol{\omega}} = \mathbf{J}_a \left.\frac{\partial \mathbf{F}_x}{\partial \boldsymbol{\omega}}\right|_{(\mathbf{x}_0,\,\mathbf{u}_0)} (\boldsymbol{\omega} - \boldsymbol{\omega}_0) + \mathbf{J}_b T_0 = \mathbf{J}_a A^{-1} \left.\frac{\partial \bar{\mathbf{f}}}{\partial \boldsymbol{\omega}}\right|_{(\mathbf{x}_0,\,\mathbf{u}_0)} (\boldsymbol{\omega} - \boldsymbol{\omega}_0) + \mathbf{J}_b T_0. \tag{89}$$

Where matrices $\mathbf{J}_a$ and $\mathbf{J}_b$ reflect the inertial properties of the drive-train and the torque redistribution caused by the limited slip action.

If the differential of a particular axle is locked, i.e., the relative velocity of the left and right wheels is zero, the dynamics of the power-train is of reduced order. From case 2 in section 3 we have $\omega_\mathrm{l} = \omega_\mathrm{r} = \omega_\mathrm{p}$. Therefore, for the locked axle the following relation holds,

$$\left(\frac{\partial \omega_\mathrm{l}}{\partial \omega_\mathrm{p}}\right)_i = \left(\frac{\partial \omega_\mathrm{r}}{\partial \omega_\mathrm{p}}\right)_i = 1 \tag{90}$$

Where subscript $i \in \{\mathrm{f}, \mathrm{r}\}$ denotes that the derivatives appearing in equation 90 belong to either the front or rear power-train.

However, if $(\omega_\mathrm{d})_i \neq 0$ the constraints 19a and 19b do not provide enough information to determine $\frac{\partial \boldsymbol{\omega}}{\partial \boldsymbol{\omega}_\mathrm{p}}$. In this case the derivative will be approximated using the steady-state wheel speed increments of the linearized power-train dynamics in response to a step-input and are given by,

$$\boldsymbol{\omega}_\mathrm{ss} = -\left(\mathbf{J}_a A^{-1} \frac{\partial \bar{\mathbf{f}}}{\partial \omega}\right)^{-1} \mathbf{J}_b \tag{91}$$

The resulting steady state wheel increments $\boldsymbol{\omega}_\mathrm{ss}$ can be used to approximate the elements appearing in $\frac{\partial \boldsymbol{\omega}}{\partial \boldsymbol{\omega}_\mathrm{p}}$. For the front axle this results in,

$$\frac{\partial \omega_\mathrm{fl}}{\partial \omega_\mathrm{pf}} \approx \frac{\Delta \omega_\mathrm{fl}}{\Delta \omega_\mathrm{pf}} = \frac{2\left(2\frac{\partial F_{x\,\mathrm{fl}}}{\partial F_{z\,\mathrm{fl}}} + (1 - r_\mathrm{f})\right)\frac{\partial f_\mathrm{fr}}{\partial \omega_\mathrm{fr}}}{\left(2\frac{\partial F_{x\,\mathrm{fl}}}{\partial F_{z\,\mathrm{fl}}} + (1 - r_\mathrm{f})\right)\frac{\partial f_\mathrm{fr}}{\partial \omega_\mathrm{fr}} + \left(2\frac{\partial F_{x\,\mathrm{fr}}}{\partial F_{z\,\mathrm{fr}}} + (1 + r_\mathrm{f})\right)\frac{\partial f_\mathrm{fl}}{\partial \omega_\mathrm{fl}}} \tag{92}$$

$$\frac{\partial \omega_\mathrm{fr}}{\partial \omega_\mathrm{pf}} \approx \frac{\Delta \omega_\mathrm{fr}}{\Delta \omega_\mathrm{pf}} = \frac{2\left(2\frac{\partial F_{x\,\mathrm{fr}}}{\partial F_{z\,\mathrm{fr}}} + (1 + r_\mathrm{f})\right)\frac{\partial f_\mathrm{fl}}{\partial \omega_\mathrm{fl}}}{\left(2\frac{\partial F_{x\,\mathrm{fl}}}{\partial F_{z\,\mathrm{fl}}} + (1 - r_\mathrm{f})\right)\frac{\partial f_\mathrm{fr}}{\partial \omega_\mathrm{fr}} + \left(2\frac{\partial F_{x\,\mathrm{fr}}}{\partial F_{z\,\mathrm{fr}}} + (1 + r_\mathrm{f})\right)\frac{\partial f_\mathrm{fl}}{\partial \omega_\mathrm{fl}}} \tag{93}$$

The approximate wheel-speed ratios only depend on the local longitudinal slip-stiffnesses, the partial derivatives of the tire-model to the normal loads and the differential-ramps respectively $\frac{\partial f_{ij}}{\partial \omega_{ij}}$, $\frac{\partial f_{ij}}{\partial F_{z\,ij}}$ and $(r_{\mathrm{D_c}})_i$. The dependence of $\boldsymbol{\omega}_\mathrm{ss}$ on the inertias is canceled out due to the left-right symmetry of the power-trains and there is no influence of T_0 due to the linear nature of equation 89. If the locking ratio $(r_{\mathrm{D_c}})_i$ is relatively large, the differential will lock at low longitudinal slip values. This means that the values of $\frac{\partial f_{ij}}{\partial F_{z\,ij}}$ are small compared to the other terms appearing in equations 92 through 93 and may be neglected.

5.3. Evaluation of the Control Effectiveness

Figure 6 provides some insight in the effects of load-transfers on the control effectiveness. The plots appearing in the first column of Figure 6 depict the control effectiveness if no load-transfer effects are present, corresponding to the nominal control effectiveness $\mathbf{G}_{\dot{\psi}}$. Column two illustrates the isolated effect of load-transfers on the control effectiveness, corresponding to $\hat{\mathbf{G}}_{\dot{\psi}}$. The last column represents the combined effect of slip and load-transfer effects.

The yaw-moment resulting from the redistribution of normal loads opposes the direction of the turn as reflected by the second column. This effect is most apparent when the axles are equipped with an open differential corresponding to the first two rows of figure 6. An open differential does not create any yaw-moments through differential torque effects but almost entirely through the decrease of lateral tire forces on the respective axle. On the front axle a decrease of lateral load causes a small yaw-moment opposing the turn (a). Consequently, the nominal control effectiveness is negative throughout most of the operating range apart from a small band of positive control effectiveness, at low input torques, caused by a steering input. However, the moments created by load-transfers are relatively large in the low torque regime, resulting in the complete absence of positive total control effectiveness as illustrated by sub-figure (c). Although the nominal control effectiveness on the rear axle equipped with an open differential is positive everywhere (d), a similar observation can be made about the total yaw-moment which is mostly opposing the direction of the turn (f).

Row three and four of Figure 6 depict the components of the control effectiveness of respectively the front and rear drive-trains equipped with locked axles. Contrary to the case with open differentials, torque increments on a locked axle are not necessarily distributed equally left and right, resulting in yaw-moments in the direction of the turn, illustrated by sub-figure (g) and (j). However, the effect of load-transfers significantly increases the area of negative control effectiveness on the front axle and almost halves the magnitude of the control effectiveness on the rear axle.

Figure 7 illustrates the effect of increasing locking coefficients and the transition from locked to unlocked conditions on the control effectiveness. At low torques the differential slip is leading to the band of negative control effectiveness seen in all of the figures. However moving to larger torques, the control effectiveness exhibits a large discontinuity towards positive control effectiveness across the point of locking. The locking coefficient both increases the size of this discontinuity and the area in which the differential is locked. Note that the zero magnitude isoline almost always coincides with this discontinuity. Consequently, changing the state of the differential almost always results in a sign change of the control effectiveness. Because the state of the differential can be inferred from wheel speed measurements, the direction of the yaw moments is therefore known as well, potentially making the INDI based controller robust against the non-monotonic character of the control effectiveness.

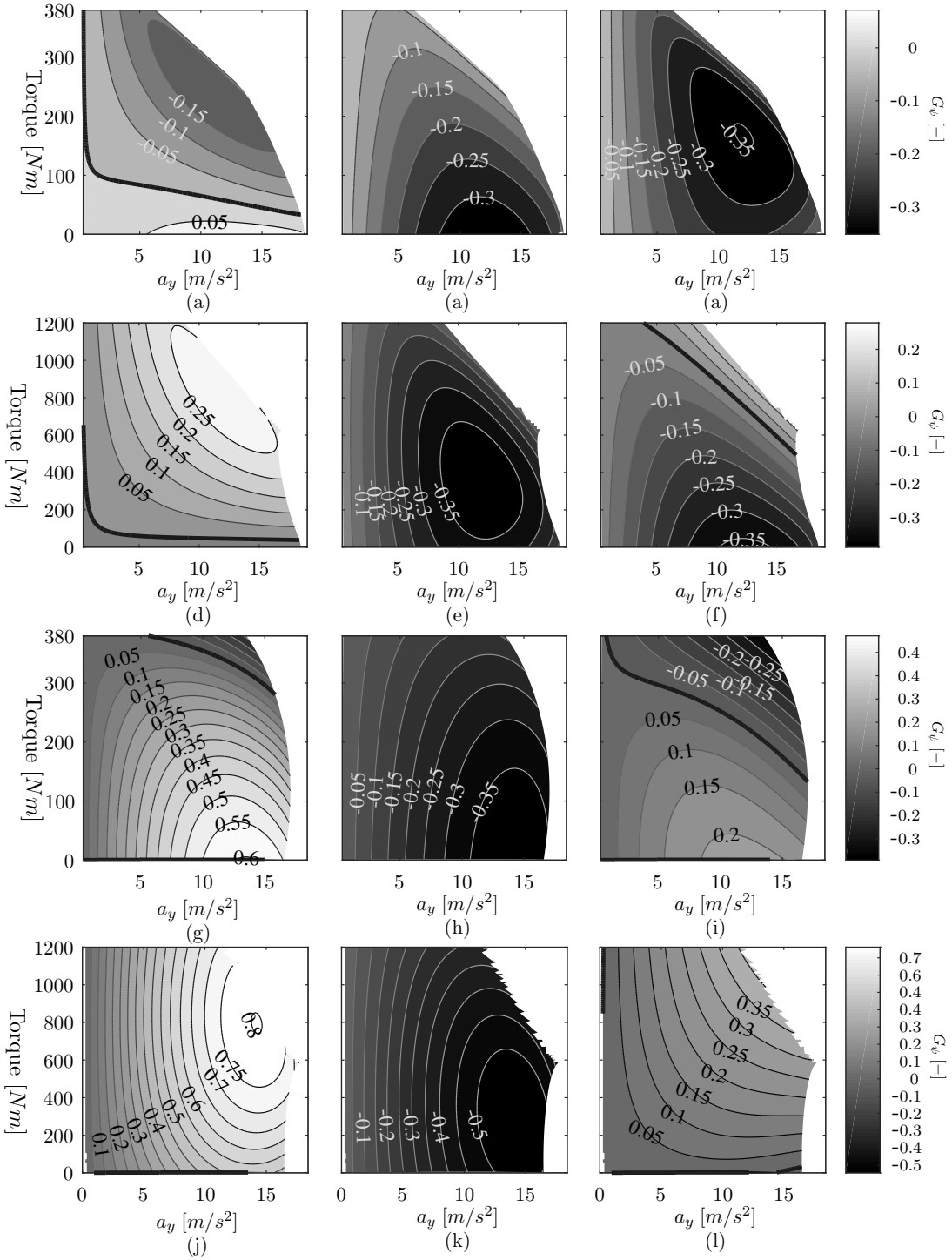

Figure 6. The effect of load-transfers on the control effectiveness. For all plots: $V_x = 30m/s$. First row (a,b,c): Front, Open differential. Second row (d,e,f): Rear, Open differential. Third row (g,h,i): Front, Locked Differential. Last row (j,k,l): Rear, Locked Differential. First column (a,d,g,j): No load transfer effects. Second column (b,e,h,k): Load transfer effect only. Last column (c,f,i,l): Total Control Effectiveness.

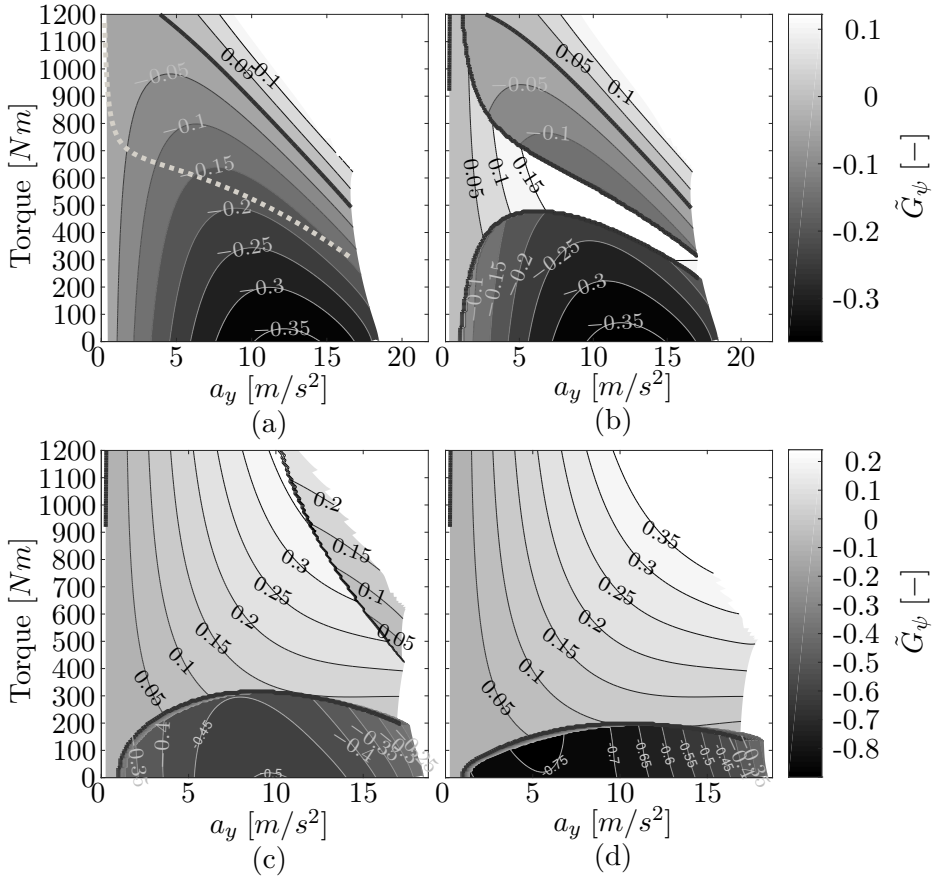

Figure 7. Control Effectiveness calculated for the rear axle at $V_x = 30m/s$ for different locking ratio's. Figure (a): $r_{\mathrm{D_c}} = 0.0$, Figure (b): $r_{\mathrm{D_c}} = 0.01$, Figure (c): $r_{\mathrm{D_c}} = 0.2$ and Figure (d): $r_{\mathrm{D_c}} = 0.5$.

6. Simulation Results

In order to evaluate the performance of the inversion based stability augmentation system, several simulation experiments were performed in conjunction with a high fidelity 40-DOF vehicle model. The model includes a full aerodynamic model and further includes the effects of suspension deformations under loads etc.

6.1. Envelope Control - Slalom Maneuver

The performance of the envelope controller is tested using a sinusoidal steering input which would otherwise result in vehicle spin. The bounds on the vehicle side-slip approximately coincide with the maximum side-slip angle of the rear outside tire. Within the yaw-rate envelope, a linear model is used to generate a yaw-rate set-point. Figure 8 provides an overview of the results of the slalom test. The vehicle starts at a velocity of $18m/s$ and accelerates due to a nominal torque command of $2\,kNm$ until it reaches approximately $60m/s$ at the end of the maneuver. The desired torque distribution such that it approximately minimizes the terminal oversteer/understeer

behavior [18].

Sub-figure (a) depicts the vehicle yaw-rate and the yaw-rate bounds corresponding the maximum and minimum side-slip. The controller is able to sufficiently track the yaw-rate set-point at the boundaries, such that the vehicle side-slip depicted in sub-figure (b) stays within the defined envelope. The time the controller starts decreasing the yaw-rate coincides with the inflection points of the side-slip angle trajectories,i.e., the yaw-rate set-point is such that it decreases the side-slip angle velocity. Sub-figure (c) shows the torques on the front and rear axle along with their desired values. Firstly, the yaw-rate is decreased through an increase of torque on the front axle and secondly by a decrease of drive-torque at the rear axle, corresponding to the signs of the front and rear control-effectiveness depicted in sub-figure (d). Note that as the velocity increases, the front differential starts to lock each time the controller increases the front torque. However, once the front axle locks, the ability to create an understeering moment is diminished, possibly even creating some oversteering moment towards the end of the maneuver. This effect is most clearly reflected in the evolution of the front axle torque; In the last four turns, the front axle torque shows a steep increase followed by a strong drop as a result of the front axle differential subsequently locking and unlocking. The controller is able to effectively handle these non-monotonicities in the control effectiveness as they are relatively straightforward to predict. Sub-figure (h) further demonstrates that the controller is able to maintain a positive acceleration while keeping the vehicle within the boundaries of the safe envelope.

6.2. Effect of Load-Transfers

A second test was done to compare the controller's performance, with and without considering load-transfers. The maneuver is equivalent to the previous experiment. Figure 9 provides the results of the two simulations. The lighter curves correspond to the simulations done with a load-transfer compensated control effectiveness and the darker curves represent the simulation done without taking into account load-transfers. Sub-figure (a) demonstrates that the maneuver without load-transfers eventually results in vehicle spin. This can be explained by examining the control effectiveness of the front and rear axle depicted in Sub-figures (b) and (c).

Initially, neglecting load-transfer effects results in underestimation of the front control effectiveness whereas the rear control effectiveness is overestimated. Although tracking is somewhat compromised, these discrepancies do not immediately result in vehicle instability. However, once the front axle locks at approximately $t = 10.5s$, the estimates of the control effectiveness are of opposite sign. The controller now incorrectly believes that decreasing the front torque will lead to a decrease yaw-rate in the direction of the turn. Moreover, the overestimation of the rear control effectiveness results in a torque decrease on the corresponding axle that only barely results in a stabilizing moment. Only after the front differential starts slipping again, the controller applies the correct torque increase, bringing the vehicle within the safe yaw-rate boundaries. When the front axle locks a second time, the incorrect estimation of the control effectiveness results in vehicle spin. These results demonstrate that including the effect of load-transfers is crucial when dealing with the limited control authority of a Limited Slip Differential.

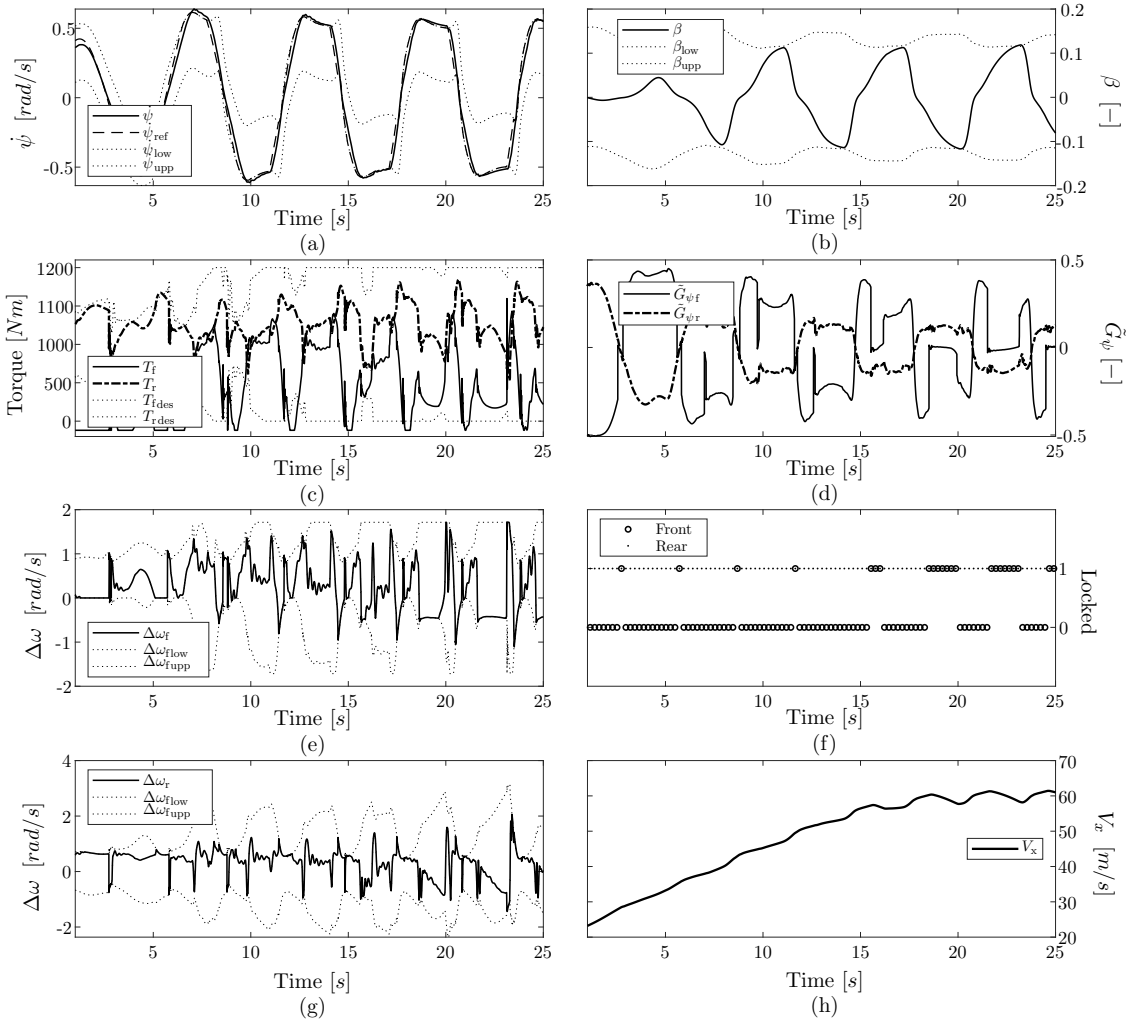

Figure 8. Results of the slalom test in conjunction with the envelope protection system: (a) Vehicle Yaw-Rate, (b) Vehicle Side Slip, (c) Torque Inputs, (d) Control Effectiveness, (e) Control Allocation Front, (f) Differential State, (g) Control Allocation Rear, (h) Velocity in x direction

6.3. Robustness Tests

In order to evaluate the robustness of the controller, several tests were done simulating a sine and dwell maneuver with artificially created model mismatch in the approximate yaw-rate inversion. The alterations are introduced at $5.5s$, half-way into the maneuver, in order create equivalent conditions when the vehicle hits the yaw-rate envelope. RMS values of the yaw-rate error ($\epsilon_{\dot{\psi}} = \dot{\psi}_{\text{ref}} - \dot{\psi}_0$) and the allocated prop-shaft velocity deltas ($\Delta\omega$) are used to quantify the tracking error and control effort respectively. The parameters of the high-fidelity model are unchanged. Therefore, the estimation of the maximum rear axle side-slip remains correct and the effects on the yaw-rate inversion are isolated.

Scaling the control effectiveness of a controller based on INDI, through for example altering the inertia of the system, affects the size of the allocated actuator commands but influences the tracking performance to a much lesser degree [23]. Therefore, the parameters that have been altered in the following tests, the friction coefficient and the location of the center of gravity in lateral and longitudinal directions, affect the

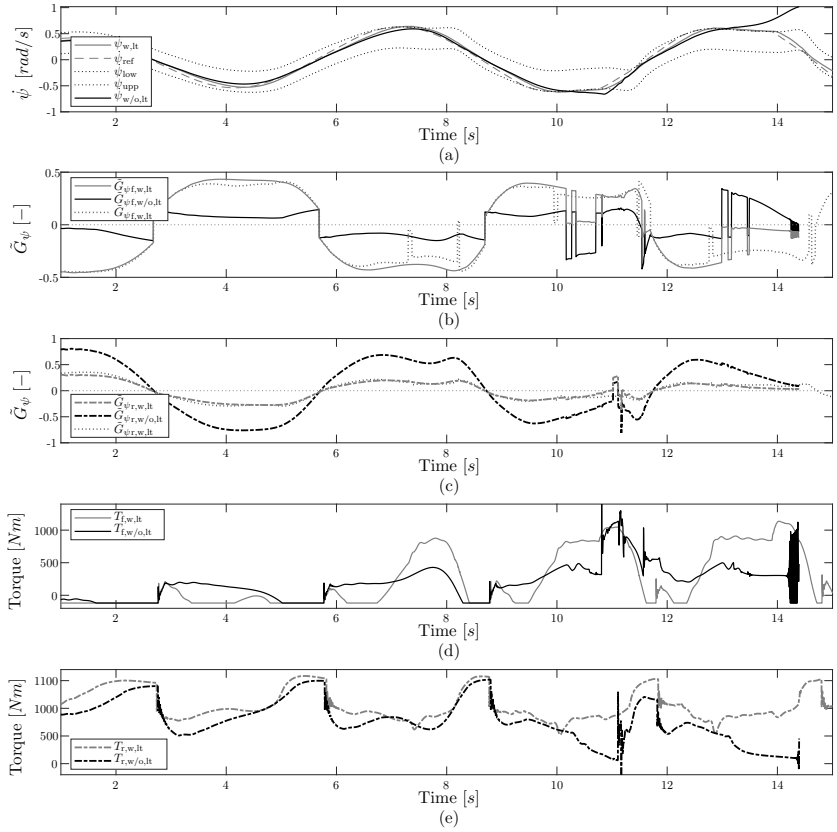

Figure 9. Results of test with load-transfer adjusted control effectiveness: (a) Vehicle Yaw-Rate, (c) Control Effectiveness, (d) Torque Inputs Front, (e) Torque Inputs Rear

control effectiveness asymmetrically.

Figure 10 illustrates the effect of scaling up the friction coefficient (μ) on the control effectiveness and tracking performance. Sub-figure (c) and (d) show the control effectiveness of the front and rear axle respectively. The nominal values are depicted with the dotted line and darker values correspond to trajectories using progressively larger parameter deviations. Although the nominal control effectiveness on both axles is increased, the load-transfer effects become more pronounced resulting in a decrease in overall control effectiveness on the rear and a correspondingly stronger increase on the front axle. At 130% the control effectiveness on the rear axle has shifted to such a degree that it is almost zero in some parts of the maneuver. However, the yaw-rate bounds are overshot slightly and the vehicle stays within the side-slip bounds. At 140 and 150% μ the controller fails to keep the vehicle within the both the yaw-rate and side-slip boundaries.

Table 2a and 2b provide the RMS values of the tracking error and control effort for the different simulations. The tracking error does not grow to large values below a friction coefficient of 30% above of the nominal value. Beyond this value, the control effectiveness on the rear axle is deteriorated to such a degree that the controller is no longer able to track the desired yaw-rate.

Scaling down the coefficient of friction results in a decrease in estimated front control effectiveness. The torque increase on the front axle in response to leaving the yaw-rate envelope is larger, leading to less time spent outside the boundaries. These results

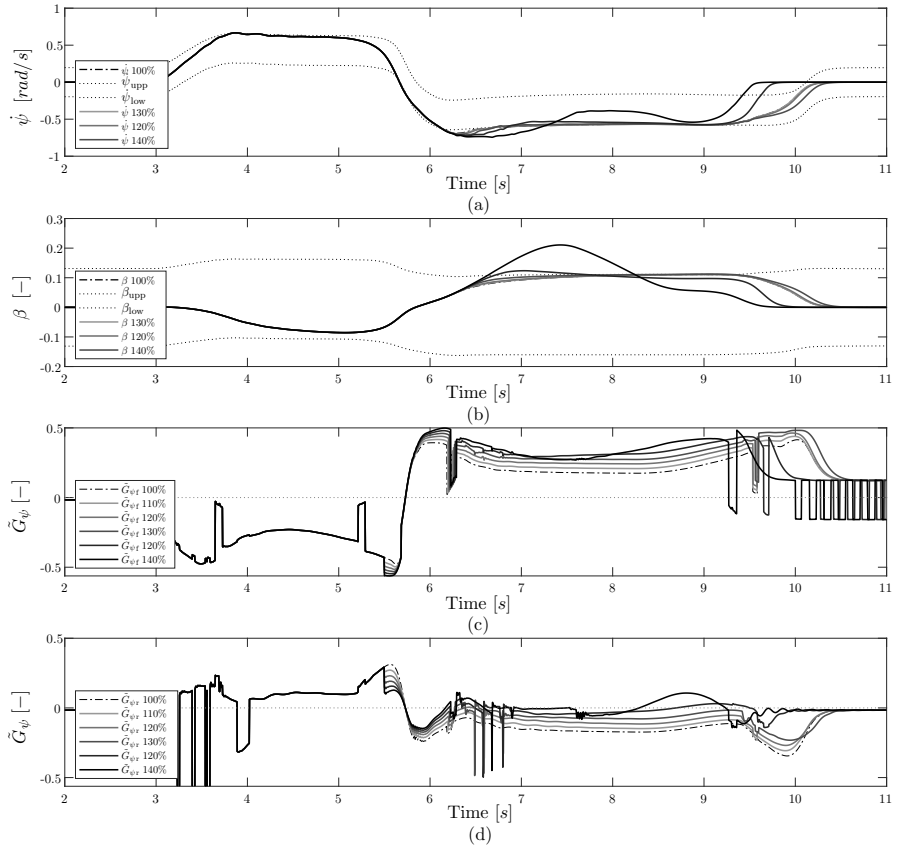

Figure 10. Results of increasing estimated friction coefficient: (a) Vehicle Yaw-Rate, (b) Vehicle Side Slip, (e) Control Effectiveness Front,(e) Control Effectiveness Rear

are illustrated by the smaller values in the first column of table 2a. These smaller values come at the cost of increased control effort reflected by the larger RMS values of the allocated prop-shaft velocity deltas. However, these values are attenuated by the bounds set in the control allocation scheme.

Table 1. RMS values of the tracking error and control effort for simulations with scaled coefficient of friction

	RMS		
	$\epsilon_{\dot{\psi}}$	$\Delta\omega_{\mathrm{f}}$	$\Delta\omega_{\mathrm{f}}$
	rad/s	rad/s	rad/s
% μ	10^{-3}	10^{-1}	10^{-1}
40	2.3	5.56	7.36
50	2.2	5.41	6.48
60	2.7	5.25	6.19
70	3.8	5.10	6.06
80	5.1	4.98	5.95
90	6.3	4.88	5.77

(a)

	RMS		
	$\epsilon_{\dot{\psi}}$	$\Delta\omega_{\mathrm{f}}$	$\Delta\omega_{\mathrm{f}}$
	rad/s	rad/s	rad/s
% μ	10^{-3}	10^{-1}	10^{-1}
100	7.5	4.83	5.63
110	8.5	4.79	5.51
120	10.1	5.10	5.21
130	14.1	5.00	5.27
140	16.0	4.91	5.16
150	19.2	4.86	5.13

(b)

In a second set of simulations the control effectiveness is corrupted by introducing a shift in the location of the center of gravity. Figure 11a and 11b provide the results obtained by respectively shifting the center of gravity to the front and to the left of the vehicle. The maneuver and the time when the parameter changes are introduced are equivalent to the sine and dwell maneuver described previously.

The performance of the controller is only marginally affected by longitudinal shift in

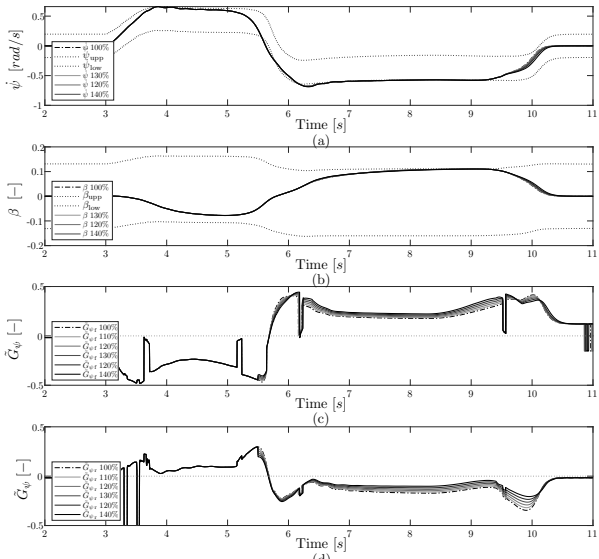

(a) Shifting Cg longitudinally: (a) Vehicle Yaw-Rate, (b) Vehicle Side Slip, (c) Control Effectiveness Front,(d) Control Effectiveness Rear

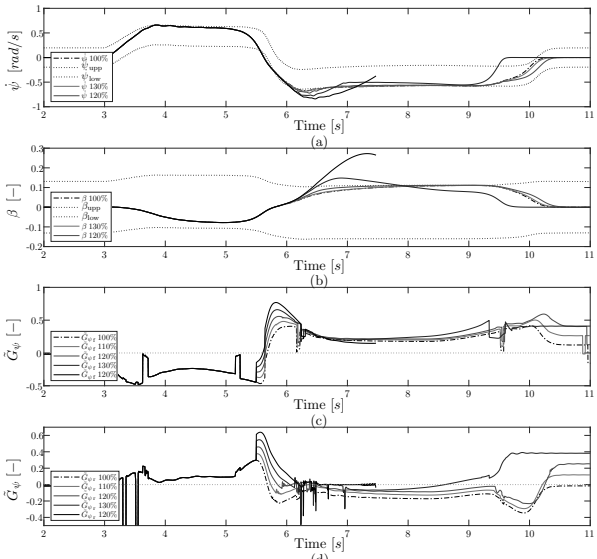

(b) Shifting Cg Laterally:(a) Vehicle Yaw-Rate, (b) Vehicle Side Slip, (c) Control Effectiveness Front,(d) Control Effectiveness Rear

Figure 11.

center of gravity location, reflected by the tracking error values in table 3a. The effects of changing lateral loads due to changes in prop-shaft velocity are much smaller than those caused by longitudinal tire forces. Therefore, the effect of a longitudinal shift of the center of gravity on the control effectiveness is small. A shift in lateral location of the center of gravity would therefore have a much stronger effect on the control effectiveness. Table 3b provides the tracking error and control effort of the simulations done with a lateral shift in center of gravity. Although the tracking performance drops more quickly, it takes a shift of 30% before the controller is not able to keep the vehicle within the side-slip bounds. Note that this point coincides with the time when the estimated control effectiveness is of different sign compared to the nominal value.

Table 2. RMS values of the tracking error and control effort for simulations with shifted center of gravity

	RMS		
	$\epsilon_{\dot{\psi}}$	$\Delta\omega_{\mathrm{f}}$	$\Delta\omega_{\mathrm{f}}$
	rad/s	rad/s	rad/s
% $d_{\mathrm{cg}}x$	10^{-3}	10^{-1}	10^{-1}
100	4.8	0.500	0.541
110	4.97	0.487	0.546
120	5.7	0.494	0.551
130	6.2	0.542	0.552
140	6.61	0.483	0.564

(a)

	RMS		
	$\epsilon_{\dot{\psi}}$	$\Delta\omega_{\mathrm{f}}$	$\Delta\omega_{\mathrm{f}}$
	rad/s	rad/s	rad/s
% $d_{\mathrm{cg}}y$	10^{-3}	10^{-1}	10^{-1}
100	4.8	0.500	0.541
110	6.1	0.505	0.551
120	16.5	0.546	0.621
130	46.0	0.591	0.566
140	143.1	0.650	0.855

(b)

7. Discussion and Concluding Remarks

Most stability augmentation systems rely on either differential drive, differential braking, active steering, or a combination thereof. This work investigated the possibilities

of stabilizing and controlling a high performance vehicle with just the front and rear differentials in conjunction with a controller based on INDI. To this end, a cascaded side-slip and yaw-rate envelope protection system was developed in combination with a model following yaw-rate controller that acts inside the bounds of the safe envelope. The presented simulation results suggest that INDI can effectively be applied to the stabilization of an LMP1 race car.

The model dependencies in the inner-loop are significantly reduced compared to conventional inversion techniques. A difficult inversion of a drive-train and tire model can be avoided by substitution with a measurement or estimate of the angular acceleration. The remaining approximate dynamic inversion depends solely on the inertial properties of the drive-train. A PCH scheme in combination with a first order reference model is used to protect from actuator saturation and provides a reliable derivative of the prop-shaft velocity reference.

INDI further allows the approximate inversion of the yaw-rate dynamics through feedback of the yaw-acceleration, directly including the locally linearized effects of the tire characteristics. The control allocation problem that remains is straightforwardly solved using weighted least squares and is suitable for real time applications. Furthermore, the effects of load-transfers have been included in the calculation of the control effectiveness. These reveal that the relatively low control authority associated with the front and rear limited slip differentials, necessitate the inclusion of load-transfer effects on the created yaw-moments. The attenuating effects of load-transfers on the control effectiveness, particularly on the rear axle, are shown to be of such magnitude that the oversteering capabilities of open differential are completely diminished in a large part of the state-space. The importance of including load-transfers in the control effectiveness was further reinforced by comparing the performance of a controller that did not incorporate load-transfer effects with a controller that used the control effectiveness suggested in this paper. The results demonstrate that neglecting load-transfer effects can lead to misinterpreting the sign of the control effectiveness, resulting in degraded controller performance.

An outer-loop consisting of an exact inversion of the vehicle side-slip allows the bounds on the side-slip to be interpreted in the yaw-rate domain. The resulting limits on the yaw-rate correspond to the values needed to stay within the side-slip envelope. A simulation of a slalom maneuver in conjunction with a high-fidelity vehicle model demonstrates that the controller is capable of effectively keeping the vehicle within the safe envelope while still maintaining the a forward acceleration, crucial in high performance applications.

Robustness of the stability augmentation system against model uncertainties in the yaw-rate inversion was demonstrated through introducing model imperfections while simulating a sine and dwell maneuver. Underestimation of the overall friction coefficient was demonstrated to have little effect on the tracking performance, even showing a performance increase, at the cost of increased control effort. Overestimation of the friction coefficient has a larger detrimental effect on controller performance. However, these effects stay small enough to maintain vehicle stability below 30% above the nominal friction value. Furthermore, shifting the center of gravity in longitudinal direction was shown to have very little effect on tracking performance as most of the induced yaw-moments are the result of longitudinal tire-forces. A shift of center of gravity location in lateral direction therefore has a stronger effect but stayed marginal below a shift of 30%. The robustness tests conducted in this work were specifically aimed at isolating the effects on the yaw-rate inversion loop. In reality over or underestimation of for example the friction coefficient also influences the safe bounds on the vehicle

side-slip and yaw-rate, but these have not been considered here.

Considering the favorable results obtained in simulation with the approximate inversion based envelope controller presented in this work, there are several opportunities for future research. Firstly, the bounds on the side-slip and yaw-rate that were implemented only approximate the stable envelope, and more elaborate methods might be able to determine these bounds more accurately. A third opportunity would be to test the performance of the controller in conjunction with a (side-slip) state-estimator and sensor noise, as these can affect the controller performance negatively. Lastly, human in the loop tests could be performed in order to determine if the controller increases the abilities of a driver controlling the vehicle in limit conditions and whether this leads to reductions in driver work-load.

References

[1] Van Zanten A, Erhardt R, Pfaff G. Vdc, the vehicle dynamics control system of bosch. SAE Technical Paper; 1995. Cited By 21.

[2] Milliken WF, Milliken DL. Race car vehicle dynamics. Vol. 400. Society of Automotive Engineers Warrendale; 1995.

[3] Tchamna R, Youn I. Yaw rate and side-slip control considering vehicle longitudinal dynamics. International Journal of Automotive Technology. 2013;14(1):53–60. Cited By 21.

[4] Cho W, Yoon J, Kim J, et al. An investigation into unified chassis control scheme for optimised vehicle stability and manoeuvrability. Vehicle System Dynamics. 2008; 46(SUPPL.1):87–105. Cited By 64.

[5] Drakunov SV, Ashrafi B, Rosiglioni A. Yaw control algorithm via sliding mode control. In: Proceedings of the American Control Conference, 2000.; Vol. 1; IEEE; 2000. p. 580–583.

[6] Delli Colli V, Tomassi G, Scarano M. "single wheel" longitudinal traction control for electric vehicles. IEEE Transactions on Power Electronics. 2006;21(3):799–808. Cited By 45.

[7] Hsu YHJ, Gerdes JC. Stabilization of a steer-by-wire vehicle at the limits of handling using feedback linearization. In: Proceedings of IMECE2005; 2005.

[8] Fredriksson J, Andreasson J, Laine L. Wheel force distribution for improved handling in a hybrid electric vehicle using nonlinear control. In: Decision and Control, 2004. CDC. 43rd IEEE Conference on; Vol. 4; IEEE; 2004. p. 4081–4086.

[9] Andreasson J, Bünte T. Global chassis control based on inverse vehicle dynamics models. Vehicle System Dynamics. 2006;44(sup1):321–328.

[10] Weiskircher T, Müller S. Control performance of a road vehicle with four independent single-wheel electric motors and steer-by-wire system. Vehicle system dynamics. 2012; 50(sup1):53–69.

[11] Shibahata Y, Shimada K, Tomari T. Improvement of vehicle maneuverability by direct yaw moment control. Vehicle System Dynamics. 1993;22(5-6):465–481.

[12] Di Cairano S, Tseng H, Bernardini D, et al. Vehicle yaw stability control by coordinated active front steering and differential braking in the tire sideslip angles domain. IEEE Transactions on Control Systems Technology. 2013;21(4):1236–1248. Cited By 62.

[13] Tahami F, Kazemi R, Farhanghi S. A novel driver assist stability system for all-wheel-drive electric vehicles. IEEE Transactions on Vehicular Technology. 2003;52(3):683–692. Cited By 85.

[14] Yim S, Choi J, Yi K. Coordinated control of hybrid 4wd vehicles for enhanced maneuverability and lateral stability. IEEE Transactions on Vehicular Technology. 2012; 61(4):1946–1950. Cited By 30.

[15] Van Zanten AT. Evolution of electronic control systems for improving the vehicle dynamic behavior. In: In Proceedings of the International Symposium on Advanced Vehicle Control (AVEC; Citeseer; 2002.

[16] Klomp M. Longitudinal force distribution and road vehicle handling [dissertation]. Chalmers University of Technology; 2010.
[17] Piyabongkarn D, Lew J, Rajamani R, et al. On the use of torque-biasing systems for electronic stability control: Limitations and possibilities. IEEE Transactions on Control Systems Technology. 2007;15(3):581–589. Cited By 34.
[18] Klomp M. On drive force distribution and road vehicle handling-a study of understeer and lateral grip [dissertation]; 2007.
[19] Uffelmann F. Automotive stability and handling dynamics in cornering and braking maneuvers. Vehicle System Dynamics. 1983;12(4-5):203–223.
[20] Motoyama S, Uki H, ISODA Manager K, et al. Effect of traction force distribution control on vehicle dynamics. Vehicle System Dynamics. 1993;22(5-6):455–464.
[21] Beal CE. Applications of model predictive control to vehicle dynamics for active safety and stability. Stanford University; 2011.
[22] Bobier CG, Gerdes JC. Staying within the nullcline boundary for vehicle envelope control using a sliding surface. Vehicle System Dynamics. 2013;51(2):199–217.
[23] Sieberling S, Chu Q, Mulder J. Robust flight control using incremental nonlinear dynamic inversion and angular acceleration prediction. Journal of Guidance, Control, and Dynamics. 2010;33(6):1732–1742. Cited By 76.
[24] Bacon B, Ostroff A. Reconfigurable flight control using nonlinear dynamic inversion with a special accelerometer implementation. In: AIAA Guidance, Navigation, and Control Conference and Exhibit; 2000. Cited By 14.
[25] Smith P. A simplified approach to nonlinear dynamic inversion based flight control. In: 23rd Atmospheric Flight Mechanics Conference; 1998. p. 762–770. Cited By 0.
[26] Slotine JJE, Li W, et al. Applied nonlinear control. Vol. 199. prentice-Hall Englewood Cliffs, NJ; 1991.
[27] Jonasson M, Andreasson J, Jacobson B, et al. Global force potential of over-actuated vehicles. Vehicle system dynamics. 2010;48(9):983–998.
[28] Jonasson M. Exploiting individual wheel actuators to enhance vehicle dynamics and safety in electric vehicles [dissertation]. KTH Royal Institute of Technology; 2009.
[29] Abe M. Vehicle handling dynamics: theory and application. Butterworth-Heinemann; 2015.
[30] Pacejka H. Tire and vehicle dynamics. Elsevier; 2005.
[31] Forstinger M, Bauer R, Hofer A. Modelling and simulation of passive limited-slip differentials. IFAC-PapersOnLine. 2015;48(1):502–507.
[32] Morselli R, Zanasi R, Sandoni G. Detailed and reduced dynamic models of passive and active limited-slip car differentials. Mathematical and Computer Modelling of Dynamical Systems. 2006;12(4):347–362.
[33] Zanasi R, Sandoni G, Morselli R. Simulation of variable dynamic dimension systems: the clutch example. In: Control Conference (ECC), 2001 European; IEEE; 2001. p. 3149–3154.
[34] Reiner J, Balas GJ, Garrard WL. Flight control design using robust dynamic inversion and time-scale separation. Automatica. 1996;32(11):1493–1504.
[35] Schumacher C, Khargonekar P, McClamroch N. Stability analysis of dynamic inversion controllers using time-scale separation. In: Guidance, Navigation, and Control Conference and Exhibit; 1998. p. 4322.
[36] Snell S, Enns D, Garrard W. Nonlinear inversion flight control for a supermaneuverable aircraft. Journal of Guidance, Control, and Dynamics. 1992;15(4):976–984. Cited By 351.
[37] Abe M, Kano Y, Suzuki K, et al. Side-slip control to stabilize vehicle lateral motion by direct yaw moment. JSAE review. 2001;22(4):413–419.
[38] Shi J, Li X, Lu T, et al. Development of a new traction control system for vehicles with automatic transmissions. International Journal of Automotive Technology. 2012; 13(5):743–750. Cited By 3.
[39] Smeur E, Chu Q, De Croon G. Adaptive incremental nonlinear dynamic inversion for attitude control of micro air vehicles. Journal of Guidance, Control, and Dynamics. 2016; 39(3):450–461. Cited By 1.

[40] Johnson EN. Limited authority adaptive flight control [dissertation]. School of Aerospace Engineering, Georgia Institute of Technology; 2000.
[41] Lombaerts T, Looye G, Chu Q, et al. Pseudo control hedging and its application for safe flight envelope protection. In: AIAA Guidance, Navigation, and Control Conference; 2010. Cited By 4.
[42] Simplicio P, Pavel M, van Kampen E, et al. An acceleration measurements-based approach for helicopter nonlinear flight control using incremental nonlinear dynamic inversion. Control Engineering Practice. 2013;21(8):1065–1077. Cited By 26.
[43] Bodson M. Evaluation of optimization methods for control allocation. Journal of Guidance, Control, and Dynamics. 2002;25(4):703–711.
[44] Virnig J, Bodden D. Multivariable control allocation and control law conditioning when control effectors limit. In: Guidance, Navigation, and Control Conference; 1994. p. 3609.
[45] Bordingnon KA, Durham WC. Closed-form solutions to constrained control allocation problem. Journal of Guidance, Control, and Dynamics. 1995;18(5):1000–1007.
[46] Enns D. Control allocation approaches. In: Guidance, Navigation, and Control Conference and Exhibit; 1998. p. 4109.
[47] Härkegård O. Backstepping and control allocation with applications to flight control [dissertation]. Linköpings universitet; 2003.
[48] Petersen JA, Bodson M. Constrained quadratic programming techniques for control allocation. IEEE Transactions on Control Systems Technology. 2006;14(1):91–98.
[49] Inagaki S, Kshiro I, Yamamoto M. Analysis on vehicle stability in critical cornering using phase-plane method. In: International Symposium on Advanced Vehicle Control (1994: Tsukuba-shi, Japan). Proceedings of the International Symposium on Advanced Vehicle Control 1994; 1994.
[50] Sherman J, Morrison WJ. Adjustment of an inverse matrix corresponding to a change in one element of a given matrix. The Annals of Mathematical Statistics. 1950;21(1):124–127.

Appendix A. Control effectiveness and Lateral Load-transfers

A.1. Lateral Load-Transfers

The effect of changing lateral load-transfers can be included into the control effectiveness but is inherently smaller than the load-transfer effects discussed so far. Furthermore, the equations become significantly more complicated and contain more uncertainties on account of equations 15a - 15b. Nevertheless, to properly evaluate effects the full effect of load-transfers on the control effectiveness and for reasons of completeness, the equations are given here.

If lateral load-transfers are included, equation 68 changes to,

$$\begin{aligned}\mathbf{F}_{\mathrm{z}} = h(\bar{\mathbf{F}}) = &\left[-\Delta W_x, -\Delta W_x, \Delta W_x, \Delta W_x\right]^{\mathrm{T}} + \\ &\left[-\Delta W_{y_{\mathrm{f}}}, \Delta W_{y_{\mathrm{f}}}, -\Delta W_{y_{\mathrm{r}}}, \Delta W_{y_{\mathrm{r}}}\right]^{\mathrm{T}}.\end{aligned} \tag{A1}$$

The partial derivative $\frac{\partial \mathbf{F}_{\mathrm{z}}}{\partial \bar{\mathbf{F}}}$ is now a full matrix, given by equation A2.

$$\frac{\partial \mathbf{F}_{\mathrm{z}}}{\partial \bar{\mathbf{F}}} = \begin{bmatrix} \frac{\partial \mathbf{F}_{\mathrm{z}}}{\partial \bar{\mathbf{F}}_x} & \frac{\partial \mathbf{F}_{\mathrm{z}}}{\partial \bar{\mathbf{F}}_y} \end{bmatrix} \tag{A2}$$

Where the block-matrix $\frac{\partial \mathbf{F}_z}{\partial \mathbf{F}_y}$ can be expressed as outer product of two vectors (A3).

$$\frac{\partial \mathbf{F}_z}{\partial \mathbf{F}_y} = \frac{\partial \mathbf{F}_z}{\partial A_y}\frac{\partial A_y}{\partial \mathbf{F}_y} \tag{A3}$$

Where,

$$\frac{\partial \mathbf{F}_z}{\partial A_y} = \begin{bmatrix} -\frac{\partial \Delta W_{y_f}}{\partial A_y} \\ \frac{\partial \Delta W_{y_f}}{\partial A_y} \\ -\frac{\partial \Delta W_{y_r}}{\partial A_y} \\ \frac{\partial \Delta W_{y_r}}{\partial A_y} \end{bmatrix} \quad \text{and} \quad \frac{\partial A_y}{\partial \mathbf{F}_y}^{\mathrm{T}} = \frac{1}{m}\begin{bmatrix} 1 \\ 1 \\ 1 \\ 1 \end{bmatrix}. \tag{A4}$$

Using equations 72, 74, A2 and A3 matrix M is rewritten to include the effects of lateral load-transfers, resulting in,

$$\bar{M} = \left(I - \frac{\partial \bar{\mathbf{f}}}{\partial \mathbf{F}_z}\frac{\partial \mathbf{F}_z}{\partial \bar{\mathbf{F}}}\right) = \begin{bmatrix} I - \frac{\partial \mathbf{f}}{\partial \mathbf{F}_z}\frac{\partial \mathbf{F}_z}{\partial A_x}\frac{\partial A_x}{\partial \mathbf{F}_x} & -\frac{\partial \mathbf{f}}{\partial \mathbf{F}_z}\frac{\partial \mathbf{F}_z}{\partial A_y}\frac{\partial A_y}{\partial \mathbf{F}_y} \\ -\frac{\partial \mathbf{g}}{\partial \mathbf{F}_z}\frac{\partial \mathbf{F}_z}{\partial A_x}\frac{\partial A_x}{\partial \mathbf{F}_x} & I - \frac{\partial \mathbf{g}}{\partial \mathbf{F}_z}\frac{\partial \mathbf{F}_z}{\partial A_y}\frac{\partial A_y}{\partial \mathbf{F}_y} \end{bmatrix} = \begin{bmatrix} A & B \\ C & D \end{bmatrix} \tag{A5}$$

In a manner similar to the method described above, by repeated application of the Sherman-Morrison formula, the inverse of matrix $\bar{M}$ can be found. Resulting in the following expression,

$$\bar{M}^{-1} = \begin{bmatrix} A^{-1} & \mathbf{0} \\ \mathbf{0} & D^{-1} \end{bmatrix} \begin{bmatrix} I + \frac{P}{|\bar{M}|}\frac{\partial \mathbf{f}}{\partial \mathbf{F}_z}\frac{\partial \mathbf{F}_z}{\partial \mathbf{F}_y} & \frac{|A|}{|\bar{M}|}\frac{\partial \mathbf{f}}{\partial \mathbf{F}_z}\frac{\partial \mathbf{F}_z}{\partial \mathbf{F}_y} \\ \frac{|D|}{|\bar{M}|}\frac{\partial \mathbf{g}}{\partial \mathbf{F}_z}\frac{\partial \mathbf{F}_z}{\partial \mathbf{F}_x} & I + \frac{Q}{|\bar{M}|}\frac{\partial \mathbf{g}}{\partial \mathbf{F}_z}\frac{\partial \mathbf{F}_z}{\partial \mathbf{F}_x} \end{bmatrix}. \tag{A6}$$

Where inverse of sub-matrix D is given by equation A7.

$$D^{-1} = I + \frac{1}{|D|}\frac{\partial \mathbf{g}}{\partial \mathbf{F}_z}\frac{\partial \mathbf{F}_z}{\partial \mathbf{F}_y} \tag{A7}$$

And the determinant of D,

$$|D| = 1 - \frac{\partial A_y}{\partial \mathbf{F}_y}\frac{\partial \mathbf{f}}{\partial \mathbf{F}_z}\frac{\partial \mathbf{F}_z}{\partial A_y}. \tag{A8}$$

Scalars P and Q are given by equation A9 and A10 respectively.

$$P = \frac{\partial A_x}{\partial \mathbf{F}_x}\frac{\partial \mathbf{g}}{\partial \mathbf{F}_z}\frac{\partial \mathbf{F}_z}{\partial A_x} \tag{A9}$$

$$Q = \frac{\partial A_y}{\partial \mathbf{F}_y}\frac{\partial \mathbf{f}}{\partial \mathbf{F}_z}\frac{\partial \mathbf{F}_z}{\partial A_y} \tag{A10}$$

Finally, the determinant of $\bar{M}$ can be expressed as,

$$\left|\bar{M}\right| = |A|\,|D| - PQ. \tag{A11}$$

With the inverse of matrix $\bar{M}$ known the control effectiveness, including the effect of changing lateral and longitudinal load-transfers, is now easily found using equation 71.

$$\frac{\partial \bar{\mathbf{F}}}{\partial \boldsymbol{\omega}} = \begin{bmatrix} A^{-1} & \mathbf{0} \\ \mathbf{0} & D^{-1} \end{bmatrix} \begin{bmatrix} I + \frac{P}{|\bar{M}|} \frac{\partial \mathbf{f}}{\partial \mathbf{F}_z} \frac{\partial \mathbf{F}_z}{\partial \mathbf{F}_y} & \frac{|A|}{|\bar{M}|} \frac{\partial \mathbf{f}}{\partial \mathbf{F}_z} \frac{\partial \mathbf{F}_z}{\partial \mathbf{F}_y} \\ \frac{|D|}{|\bar{M}|} \frac{\partial \mathbf{g}}{\partial \mathbf{F}_z} \frac{\partial \mathbf{F}_z}{\partial \mathbf{F}_x} & I + \frac{Q}{|\bar{M}|} \frac{\partial \mathbf{g}}{\partial \mathbf{F}_z} \frac{\partial \mathbf{F}_z}{\partial \mathbf{F}_x} \end{bmatrix} \frac{\partial \bar{\mathbf{f}}}{\partial \boldsymbol{\omega}} \tag{A12}$$

Part II

Thesis

Chapter 1

Introduction

The World Endurance Championship (WEC) features some of the most technologically advanced race cars that exist today. The Le Mans Prototype 1 (LMP1) class of race cars compete in races lasting from 6 up to 24 hours, the most famous being the *'24h of Le Mans'*. The WEC stands out from other high performance race classes in that it allows certain technologies to be used that have otherwise been prohibited. Where most championships have banned the use of modern driver assist technologies like Traction Control (TC), the WEC a race class that revolves around technology and strategy, permits a restricted form to be used. In this project, Incremental Nonlinear Dynamic Inversion (INDI) a control technology first developed for aerospace applications is investigated outside its usual context and will be applied to the traction and stability control problem of an LMP1 race car.

Traction Control systems regulate the longitudinal wheel slip to an optimal value for maximum traction and can be used to prevent excessive wheel spin. Systems that regulate traction or braking forces to stabilize or control the vehicle in lateral direction, are loosely referred to as Electronic Stability Control (ESC) systems (Rajamani, 2011). Traction and stability control systems are developed for consumer cars with the goal of increased safety in limit conditions, where the average driver would lose control of the vehicle (Van Zanten, 2000). However, even an experienced race driver operating a car at the very limit of the stable envelope could benefit from such a system.

Road vehicle control design is inherently difficult because of the highly nonlinear and complex nature of the vehicle dynamics. Traction Control systems that can be found on consumer vehicles, prevent the driver from entering the highly nonlinear region of the state-space entirely. However, in the context of high performance race cars, this highly nonlinear region is exactly what the driver is after (Milliken & Milliken, 1995). In other words, the control system should increase the driver's abilities to keep the race car in this part of the state space, where nonlinearities and high accelerations govern the vehicle dynamics.

Another intrinsic difficulty in Traction Control design is the uncertainty of the dynamics of the tire-road interaction. A lot of time and effort is spent on identifying and modeling tire characteristics which change with road conditions, tire temperatures and tire wear. These

nonlinear and uncertain dynamics demand a more complex and at the same time robust control system design than can be expected for a regular consumer car.

Electronic Stability Control systems rely on a number of different actuators to regulate the driving force at each wheel. The most common implementation in road vehicles involves using the hydraulic braking system to reduce traction force on a given axle or wheel, other mechanisms use engine/motor torque control or an active differential (Manning & Crolla, 2007). The LMP1 car under consideration is able to control the traction force on each axle through regulating the torque supplied by two separate motors, one at each axle. The drive shafts on both axles are driven through a limited slip differential which means that wheel slips can not be controlled individually, making pure torque vectoring impossible. However, because the car is operated in the highly combined slip range of the tire, the lateral dynamics of the car can be controlled by regulating traction forces which in turn affect the lateral forces generated by each tire. (H. Pacejka, 2005).

The aim of the proposed research project is to contribute to the development of a robust Traction Control system for an LMP1 race car. For this purpose, a technique that has recently been developed in the aerospace industry called Incremental Nonlinear Dynamic Inversion will be investigated (Sieberling, Chu, & Mulder, 2010). This sensor based technique has favorable robustness characteristics compared to classical nonlinear dynamic inversion and can be applied, with relative ease, to a much wider range of highly nonlinear systems, with control variables that do not appear affine in the state equations. These properties make it a suitable candidate for the design of a high performance TC system.

Chapter 2

Background

2-1 Literature Review

The first traction control systems were mainly developed to maximize traction forces in on-throttle situations by avoiding wheel-spin in a similar way that anti-lock brake systems prevent the wheel from locking up during braking (Tomizuka & Hedrick, 1995). Although different methods can be used to regulate the driving force, the most frequently used mechanism involves using the vehicle's braking system. Other implementations control engine torque, or more recently an active differential, to control wheel-slip (Rajamani, 2011).

Traction control systems later evolved into stability control systems that regulate the traction force to influence the lateral dynamics of the vehicle. The lateral stability of the vehicle is governed by the vehicle side-slip and/or vehicle yaw rate. Inagaki, Kshiro, & Yamamoto, 1994 used phase plane analysis in the side-slip - side-slip velocity ($\beta - \dot{\beta}$) plane to identify the stable regions of the open-loop vehicle dynamics. Another such method focuses on the slide-slip - yaw-rate ($\beta - \dot{\psi}$) plane Bobier, 2012. Most vehicle stability control systems therefore, employ some form or combination of yaw-rate or side slip control to ensure vehicle stability.

Today, vehicle stability control systems can be categorized into direct yaw-moment control, in which individual wheel forces are controlled to create a corrective yaw moment, active steering systems that control the steering angle to influence the lateral dynamics, or active suspension systems that control the wheel vertical loads (Manning & Crolla, 2007). This review is primarily focused on traction control systems and stability control systems that regulate traction forces only, as other approaches like active steering and suspension systems are banned from the WEC. Because a novel control strategy is investigated, this section surveys the control strategies that have previously been applied to traction and stability control.

2-1-1 Traction Control

Several control methods have been used for the low level traction control problem. Delli Colli, Tomassi, & Scarano, 2006 presented a longitudinal fuzzy wheel slip controller that tracks a

friction gradient based on throttle paddle position. They introduce a simple friction estimator that effectively copes with changing road conditions. The estimated friction slope is used in two controller designs that are based on fuzzy logic and sliding modes techniques respectively and require a simple tuning approach.

Shi, Li, Lu, & Zhang, 2012 developed a wheel slip controller based on feedback linearization that tracks the slip ratio for maximum longitudinal force. The longitudinal slip set point is generated using a simple gradient ascent method that finds the wheel slip for which an estimated longitudinal friction per longitudinal slip gradient goes to zero,i.e., longitudinal slip for which longitudinal force is maximized. Feedback linearization is done on a quarter car model for which the control variable naturally appears affine in the output. A sliding mode controller for the wheel slip error is added to provide robustness against modeling errors.

To avoid the discontinuous control or chattering that is accompanied with first order sliding mode techniques, Amodeo, Ferrara, Terzaghi, & Vecchio, 2010 propose a second order sliding mode wheel slip controller in which discontinuous behavior is restricted to the derivative of the control. A sliding mode observer that estimates the maximum friction coefficient is incorporated to create a controller that is less sensitive to changing road conditions.

There are several ways the traction force can be regulated. To compare the performance of two actuators on a front wheel drive and a four wheel drive car, Song & Boo, 2004 designed sliding mode controllers based on differential braking, engine torque regulation and a combination of the two. The effect of the controllers during turning maneuvers was investigated using a driver model and a fixed longitudinal slip set point. They found that the low level controllers had a large effect on vehicle stability without considering the lateral dynamics of the system and that the integrated method demonstrated the highest performance.

The previously presented methods only controlled the wheel and slip dynamics and looked at the resulting longitudinal dynamics of the car. However, the traction forces have a large influence on the lateral dynamics through the combined slip characteristics of tires (H. B. Pacejka & Bakker, 1992). Park & Kim, 1999 demonstrated that the lateral stability of the car can be improved by considering this combined slip behavior, on a front wheel driven car, without direct feedback on the lateral vehicle states. They designed a traction control system that uses a varying slip set point based on the estimated side-slip of the driven tires. A PI controller is used to regulate the throttle position to attain the desired slip ratio. Although the paper does not state the slip tracking performance of the control scheme, the turning performance and understeering properties of the vehicle are improved compared to fixed slip ratio traction controllers.

2-1-2 Vehicle Stability/dynamics Control

One of the first commercially available vehicle stability control systems is that of Bosch (Van Zanten, Erhardt, & Pfaff, 1995). This early system creates a correcting yaw moment by introducing a traction force difference between left and right wheels through the braking system to stabilize the vehicle in situations where a regular driver could potentially lose control. The direct yaw moment control (Shibahata, Shimada, & Tomari, 1993) approach is used in the majority of stability control systems that are discussed in literature. Although the braking system can not be employed directly by the traction control system of the LMP1 race car (FIA, 2016), the control strategies are largely the same.

One of the most widely proposed control techniques in literature is Sliding Mode Control (SMC). Drakunov, Ashrafi, & Rosiglioni, 2000 created a yaw control algorithm based on sliding mode techniques for a vehicle model with unknown slip characteristics. The controller distributes braking torques between left and right wheels to create a control moment. Both the longitudinal and lateral friction forces are assumed to be unknown nonlinear functions. The longitudinal force is assumed to depend on longitudinal velocity and wheel speed whereas the lateral force is assumed to depend on lateral velocity only. This general structure results in an uncertainty in the sign of the applied torque in the sliding mode control scheme. A periodic switching function is applied to overcome this problem and it is shown that yaw rate tracking is possible without extensive knowledge of the tire characteristics.

Yaw rate tracking alone is not guaranteed to result in a stable vehicle because in some cases the side-slip angle tends to diverge (Rajamani, 2011). An alternative approach is to track a side-slip angle target instead. Abe, Kano, Suzuki, Shibahata, & Furukawa, 2001 propose a controller that tracks the side-slip response of a bicycle model at constant velocity. A sliding controller is used to minimize the error between the measured side-slip and the desired response. Under the proposed conditions the side-slip angle reference tracking method's stabilizing performance is shown to be higher than the performance of yaw rate reference tracking method. Tchamna & Youn, 2013 present an integrated yaw rate and vehicle side-slip controller based on differential braking, which does not incorporate the usual simplifying assumptions such as constant longitudinal velocity and small side-slip angles. Instead, the full equations for the derivative of the side-slip angle are used. The proposed sliding mode surface incorporates both a yaw rate and a vehicle side-slip tracking error. They demonstrate that a trade-off exists between side-slip angle and yaw rate reference tracking but that the side-slip angle is most important from a stability point of view.

One of the downsides of using braking forces to influence the yaw response of a vehicle, is its negative effect on the longitudinal velocity. In order to overcome this problem Cho, Yoon, Kim, Hur, & Yi, 2008 investigated control strategy based on sliding mode techniques in combination with a control allocation algorithm. The brake force is allocated to each wheel through a numerical optimal control law, based on the Karush-Kuhn-Tucker conditions, that minimizes the unwanted longitudinal deceleration. Yim, Choi, & Yi, 2012 present a linear computational efficient weighted pseudo inverse control allocation algorithm with a similar objective that can run in real time. The weights of the pseudo inverse were chosen such that the yaw rate error and longitudinal velocity delta were minimized over a simulated maneuver. The resulting algorithm is simple and fast, but its weights are static thus might not yield the same results for every maneuver.

Apart from the sliding mode approaches that were discussed above, several other control techniques have been proposed in literature. Di Cairano, Tseng, Bernardini, & Bemporad, 2013 investigate a model predictive control architecture for a driver requested yaw rate tracking controller based on active front steering and differential braking. One of the downsides of model predictive control is that most implementations are computationally heavy. In order to run on common automotive electronic control units, an offline prediction model is created using a bicycle model at constant velocity and a piecewise affine approximation of the tire slip behavior. A hybrid model predictive controller is designed to track a desired yaw rate and to keep the tire side slip angles within acceptable bounds. Tahami, Kazemi, & Farhanghi, 2003 introduced a completely different, fuzzy logic based, stability system for all-wheel drive electric vehicles. The system is split between a high level fuzzy yaw rate controller and indi-

vidual low level fuzzy wheel speed controllers. A neural network is trained using sine wave maneuvers on different velocities to create a nonlinear yaw rate reference generator that uses inputs from a fuzzy vehicle speed estimator and the current steering angle. The yaw rate controller uses the yaw rate reference and the measured yaw rate acceleration to calculate a torque difference between left and right driven wheels to attain the desired yaw rate.

2-1-3 Front to Rear torque distribution

The techniques discussed so far regulated traction force trough differential braking for cars with combustion engines and driving torque distribution strategies for electric vehicles. Differential braking is not allowed in the WEC therefore, the traction force can only be influenced by controlling the front and rear motor torque the LMP1 car. Because the LMP1 car operates in the highly nonlinear and combined slip region of the tire during cornering, longitudinal forces have a significant effect on lateral forces. Furthermore, accelerating and braking actions have a large effect on the distribution of lateral forces through longitudinal load-transfers. The magnitude and distributions of front and rear driving torques therefore have a considerable effect on handling and stability characteristics (Uffelmann, 1983; Motoyama, Uki, ISODA Manager, & YUASA Manager, 1993).

Klomp, 2007 examines the front to rear torque distribution at specific longitudinal accelerations for different drive-line configurations taking into account longitudinal load-transfers. For moderate to large longitudinal accelerations, the front to rear drive distribution that results in the largest possible lateral acceleration, corresponds to that which balances front and rear axle yaw-moment potentials.

Piyabongkarn, Lew, Rajamani, Grogg, & Yuan, 2007 investigate distributing the front and rear driving torques, as a means for yaw stability control. The tested system is a four wheel drive passenger car with an initially front axle driven configuration with a variable torque transfer to the rear axle. An electronically controlled limited slip differential is used to transfer torque from left to right. The torque biasing system is demonstrated to be able to create an oversteering yaw moment during on-throttle situations. A low level controller was able to meet the yaw moment demand of a high level yaw controller by distributing the driving forces with proposed system.

2-1-4 Dynamic Inversion Techniques in Automotive

Hsu & Gerdes, 2005 present a stability controller based on feedback linearization for a steer-by-wire vehicle. A simple pure-slip piece-wise defined tire model is used to facilitate the inversion of a constant velocity bicycle model. The resulting controller is uniquely defined for different regions of lateral tire-slip for each wheel and combinations thereof and is demonstrated to outperform a simple linear controller.

One of the difficulties with the inversion of a vehicle model arises from the modeling of tire-force characteristics. Accurate tire modeling requires the consideration of highly nonlinear saturation and combined slip effects. The resulting equations are typically not invertible and cause control variables to appear in a non-affine manner. Consequently, dynamic inversion techniques applied to road-vehicle control frequently incorporate some (nonlinear) solver to find the control variables.

A common approach to circumvent the inversion of a complex tire-model, uses the total vehicle body forces as intermediate or virtual control variables. The subsequent distribution of tire forces results in an inherently nonlinear optimization problem. Fredriksson, Andreasson, & Laine, 2004 adopt this method to allow for the inversion of the vehicle state equations in a controller of an over-actuated vehicle. The proposed control allocation problem simultaneously solves the problem of non-affine control inputs and the distribution of control effort among the actuators. Nonlinear constraints are included that prevent using any tires past their limit, however a solver was not specified. Weiskircher & Müller, 2012 assume that any tire force can be obtained and propose a linear straightforward control allocation strategy solely based on car geometry. A downside of this approach is that no tire or actuator limits can be considered. Andreasson & Bünte, 2006 handle the nonlinearities arising in a similar context by linearizing the associated equations and solving a subsequent weighted least squares control allocation problem.

2-2 Knowledge Gaps and Contributions

The majority of the methods presented in literature on stability control employ robust nonlinear control strategies such as sliding mode techniques. SMC offers robustness against uncertain tire characteristics due to changing road conditions and un-modeled vehicle dynamics. However, sliding mode techniques commonly result in a discontinuous control signal, which can be an important downside in some applications. Furthermore, Sliding Mode (SM) techniques that result in smooth control signals, performs ideally when provided with accurate bounds on model uncertainties (Slotine, Li, et al., 1991).

Feedback Linearization (FBL) is difficult to apply to the stability control of a car due to the structure of the nonlinear vehicle dynamic equations and its inherit sensitivity to modeling errors. The only examples of FBL for traction control are on quarter car models in pure slip conditions, which limits their applicability outside the context of simulations. For vehicle stability control, inversion techniques typically involve some nonlinear optimization problem to solve for the control inputs due to uninvertible tire models. Linearizations can be used to yield algorithms that can be solved in real time. However, all these methods suffer from very little robustness against modeling errors, inherent to feedback linearization or nonlinear dynamic inversion techniques.

INDI is an approximate, sensor based form of FBL, developed for aerospace applications, which does not have the inherent limitations of regular FBL (Sieberling et al., 2010). FBL has been demonstrated to be robust against modeling errors. Its favorable robustness properties and simplicity make it a very interesting candidate for the automotive stability augmentation. Chapter 3 provides a short introduction to INDI. No examples of this control technique have been found in the field of automotive control. Exploring this technique outside the usual context of aerospace applications by applying and adjusting it to the stability control problem of a race car is considered the main contribution of the proposed work to the existing body of knowledge.

Additionally, the effectiveness of actuating the front and rear axle is studied in detail and a method is presented which incorporates load-transfer effects in the effectiveness directly.

2-3 Research Questions and Objectives

In this section, the project objective is defined and broken down into sub-goals. The objective and the sub-goals which make up the research framework have been used to formulate the main research question which is in turn split into sub-questions.

2-3-1 Project Objective

The main objective of the proposed research project can be stated as follows,

> *Contribute to the development of a vehicle control system of an LMP1 race car by designing a robust traction control system and stability augmentation system based on Incremental Nonlinear Dynamic Inversion*

Several sub-goals are identified which together should be sufficient to achieve the main objective of the project.

- Perform literature research on relevant topics
  - Perform literature research on the vehicle and tire dynamics
  - Perform literature research on stability and traction control
  - Perform literature research on (Incremental) Nonlinear Dynamic Inversion
- Design a prototype control system and show the feasibility of the proposed controller
  - Establish the control objective
  - Create a vehicle model with sufficient fidelity for design of prototype controller
  - Design a prototype stability augmentation controller
  - Perform a verification and validation step for model and prototype controller
  - Asses controllability of the system in different regions of the state space
- Incorporate the torque demand of the driver in the control design by implementing a control allocation method
- Implement the controller on a high definition vehicle model provided by Audi Sport and adjust methods if necessary
  - Perform a verification and validation step for the final controller
  - Perform performance and robustness tests on the final controller to evaluate the efficacy and robustness of the proposed control method

2-3-2 Project Research Question

The main research question relating to the main objective of the proposed project can be stated as follows,

> *What is an effective and robust control design of a traction and stability control system for an Le Mans Prototype 1 based on Incremental Nonlinear Dynamic Inversion?*

The proposed research question is split up in two sub-questions. The first question relates to the structure of the control system and the second to the efficacy and robustness of the method.

- What control structure, based on Incremental Nonlinear Dynamic Inversion, achieves the stability and traction control objective?
  - What is the control objective, in terms of controlled variables, of the vehicle stability control problem?
  - Is the system Time-Scale separable?
  - If the system is Time-Scale separable, what control structure should be chosen i.e. what are the intermediate variables?
  - What type of inversion loop is needed for each intermediate variable? i.e. exact, approximate or incremental?
  - Does Psuedo Control Hedging improve the performance of the inner loop?
  - What type of control allocation method, effectively constrains the total applied torque to the drivers torque demand and avoids excessive wheel spin?
- What is the performance of the designed control system based on Incremental Nonlinear Dynamic Inversion?
  - What is the performance of the controller in terms of the classic performance measures such as rise-time, overshoot, control error for each loop.
  - What is the performance of the controller in terms of system specific performance measures?
    - What is the effect of longitudinal load-transfer on controller performance?
    - What is the effect of switching states of the limited slip differential, i.e., locked versus open on controller performance?
    - What is the effect of vertical wheel load disturbances on controller performance?
  - Is the controller robust against model uncertainties and actuator/sensor delays?
    - What is the influence of uncertainties in the tire model on controller performance?
    - What is the influence of uncertainties in the location of the center of gravity on controller performance?
    - What is the influence of uncertainties in the vehicle inertia on controller performance?

2-4 Thesis Outline

The structure of the remaining chapters of this work is as follows: Firstly, chapter two offers a broad survey of the available literature on traction and stability control in an automotive context in section one. The following section identifies possible knowledge gaps and elaborates how this work contributes to the existing body of knowledge. Lastly, the research objective and research question are formalized and subsequently broken down into sub-goals and sub-questions in section three.

Chapter three provides a short introduction into feedback linearization or nonlinear dynamic inversion and its incremental form INDI. Chapter four presents the planar seven degree of freedom vehicle model, utilized during preliminary control structure design and evaluation of the control effectiveness, in three sections. The first section describes the body dynamics in the relevant reference frames. Section two provides a detailed description of a switched order limited slip differential model and a well know semi empirical tire model is elaborated in section three.

Chapter five presents the structure of the proposed cascaded control system. The first section identifies the different time scales present in the vehicle dynamics, which are then related to the different control loops. The following section describes the prop-shaft velocity control loop and introduces an aerospace control concept known as pseudo control hedging (Johnson, 2000). Section three describes the yaw-rate loop and presents an efficient active-set weighted least squares control allocation algorithm (Härkegård, 2003). Section four presents the side-slip loop and the corresponding dynamic inversion. Lastly, the envelope protection system is described.

Chapter six elaborates the calculation of the yaw-rate control effectiveness. Section one presents the calculation of the tire-force jacobian and introduces a method to incorporate the effect of varying load-transfers in the control effectiveness directly. Section two offers a method for the approximation of the wheel speed increments depending on the state of the limited slip differential. An elaborate discussion of the magnitude, sign and important influencing states and parameters of the control effectiveness, in different quasi-steady state driving conditions, is presented in section three.

Chapter 3

Incremental Nonlinear Dynamic Inversion

This section gives an introduction to the control approach which is to be used in the proposed project. The vehicle dynamics will not be discussed in this document as exploring this control strategy in the context of automotive control is the focus of the project. First a short introduction to classical Nonlinear Dynamic Inversion is given, then the incremental form is discussed.

3-1 Feedback Linearization/ Nonlinear Dynamic Inversion

Consider the nonlinear system 3-1 in which the control input appears affine in the state equations.

$$\begin{aligned} \dot{\mathbf{x}} &= \mathbf{f}(\mathbf{x}) + \mathbf{G}(\mathbf{x})u \\ y &= h(\mathbf{x}) \end{aligned} \tag{3-1}$$

Nonlinear Dynamic Inversion or Feedback Linearization amounts to finding a state transformation $z = T(x)$ and a suitable control input mapping $u = a(x) + b(x)\nu$ which creates a linear differential relation between the output y and the new control input ν (Slotine et al., 1991). This section discusses the Single-Input Single-Output (SISO) case for a system with relative degree one.

The first step is to find a direct relation between the output y and the input u. This is done by differentiating the relation $y = h(\mathbf{x})$, r times until the input appears directly in the equation. Differentiating once, results in equation 3-2.

$$\begin{aligned} \frac{dh(\mathbf{x})}{dt} &= \frac{\partial h(\mathbf{x})}{\partial \mathbf{x}} \frac{\mathbf{x}}{dt} = \nabla h(\mathbf{x})\dot{\mathbf{x}} = \nabla h(\mathbf{x})[\mathbf{f}(\mathbf{x}) + \mathbf{G}(\mathbf{x})u] \\ &= \nabla h(\mathbf{x})\mathbf{f}(\mathbf{x}) + \nabla h(\mathbf{x})\mathbf{G}(\mathbf{x})u = L_f h(\mathbf{x}) + L_g h(\mathbf{x})u \end{aligned} \tag{3-2}$$

Where $L_f h(\mathbf{x})$ and $L_g h(\mathbf{x})$ are the Lie derivatives of the smooth scalar function h with respect to the vector fields $\mathbf{f}$ and $\mathbf{G}$ respectively. Assuming that $L_g h(\mathbf{x}) = 0$ a direct relation between input and output has not yet been found. Continuing the differentiation process leads to,

$$\frac{d^i h(\mathbf{x})}{dt^i} = L_f^i h(\mathbf{x}) + L_g L_f^{i-1} h(\mathbf{x}) u \tag{3-3}$$

If after differentiating r times, $L_g L_f^{r-1} h(\mathbf{x}) \neq 0$, i.e., the relative degree of the system is r, we have found a direct relationship between the output y and the input u. (3-4)

$$y^i = L_f^i h(\mathbf{x}) + L_g L_f^{i-1} h(\mathbf{x}) u \tag{3-4}$$

Equating the right hand side in equation 3-4 to ν and inverting, results in a mapping between ν and u that renders a linear differential relation between the output y and the new input ν. (3-6)

$$u = (L_g L_f^{i-1} h(\mathbf{x}))^{-1} (\nu - L_f^i h(\mathbf{x})) \tag{3-5}$$

$$\dot{y} = \nu \tag{3-6}$$

Now classical linear control techniques can be used to design a controller for the transformed system described by equation 3-6. The SISO case, discussed here, is readily extended to the MIMO.

3-2 Incremental Nonlinear Dynamic Inversion

Incremental Nonlinear Dynamic Inversion (INDI) is an approximate, sensor based, form of Nonlinear Dynamic Inversion (Sieberling et al., 2010), sometimes also referred to as approximate (Bacon & Ostroff, 2000) or simplified Feedback Linearization (Smith, 1998). INDI can be applied to the general nonlinear system (3-7) and starts by approximating the state equations by a Taylor series expansion (3-8).

$$\dot{\mathbf{x}} = \mathbf{f}(\mathbf{x}, \mathbf{u}) \tag{3-7}$$

$$\dot{\mathbf{x}} \approx \mathbf{f}(\mathbf{x}_0, \mathbf{u}_0) + \left.\frac{\partial \mathbf{f}(\mathbf{x}, \mathbf{u})}{\partial \mathbf{x}}\right|_{(\mathbf{x}_0, \mathbf{u}_0)} (\mathbf{x} - \mathbf{x}_0) + \left.\frac{\partial \mathbf{f}(\mathbf{x}, \mathbf{u})}{\partial \mathbf{u}}\right|_{(\mathbf{x}_0, \mathbf{u}_0)} (\mathbf{u} - \mathbf{u}_0) + \text{h.o.t.} \tag{3-8}$$

By neglecting higher order terms and realizing that for high control rates the term $(\mathbf{x} - \mathbf{x}_0)$ vanishes, equation 3-8 simplifies to,

$$\dot{\mathbf{x}} \approx \mathbf{f}(\mathbf{x}_0, \mathbf{u}_0) + \left.\frac{\partial \mathbf{f}(\mathbf{x}, \mathbf{u})}{\partial \mathbf{u}}\right|_{(\mathbf{x}_0, \mathbf{u}_0)} (\mathbf{u} - \mathbf{u}_0). \tag{3-9}$$

Further, noting that

$$\mathbf{f}(\mathbf{x}_0, \mathbf{u}_0) = \dot{\mathbf{x}}_0, \tag{3-10}$$

and defining the control effectiveness as,

$$\mathbf{G}(\mathbf{x}_0, \mathbf{u}_0) = \left.\frac{\partial \mathbf{f}(\mathbf{x}, \mathbf{u})}{\partial \mathbf{u}}\right|_{(\mathbf{x}_0, \mathbf{u}_0)}, \tag{3-11}$$

equation 3-9 simplifies to,

$$\dot{\mathbf{x}} \approx \dot{\mathbf{x}}_0 + \underbrace{\mathbf{G}(\mathbf{x}_0, \mathbf{u}_0)}_{\text{Control Effectiveness}}(\mathbf{u} - \mathbf{u}_0). \tag{3-12}$$

Where $\dot{\mathbf{x}}_0$ is the state derivative measured at time $t = t_0$.

In a similar way to exact NDI, by equating the right hand side of equation 3-12 to ν and inverting, one ends up with a mapping between the original control input u and the virtual control ν (3-13), which results in a linear differential relation between the state $\mathbf{x}$ and ν (3-14).

$$\Delta\mathbf{u} = \mathbf{G}^{-1}(\mathbf{x}_0, \mathbf{u}_0)(\nu - \dot{\mathbf{x}}_0) \tag{3-13}$$

$$\dot{\mathbf{x}} = \nu \tag{3-14}$$

Note that contrary to standard NDI the mapping (3-13) results in a control increment only. The new control input can be calculated with equation 3-15.

$$\mathbf{u} = \Delta\mathbf{u} + \mathbf{u}_0 \tag{3-15}$$

Where $\mathbf{u}_0$ is the actuator state as measured at time $t = t_0$.

There are several advantages of Incremental Nonlinear Dynamic Inversion compared to exact Nonlinear Dynamic Inversion. Fist of all, only the model component related to the effect of the actuator on the dynamics, or control effectiveness matrix (3-12), is needed for the inversion. Second, the method is robust against modeling errors in the control effectiveness. Sieberling et al., 2010 show that the inverted system stays linear in case of model uncertainties, as opposed to the inverted system using classic NDI. Modeling errors will result in lower performance but will not cause the linear control law to break down. Finally INDI can be applied to the more general nonlinear system (3-7) as opposed to Nonlinear Dynamic Inversion (NDI) which works for nonlinear systems in which the control input appears affine in the equations (3-1).

3-3 Psuedo Control Hedging

Recently, INDI has been investigated in combination with Psuedo Control Hedging (PCH) (Simplicio, Pavel, Kampen, & Chu, 2013). The technique was originally designed to cope with actuator limits in the context of adaptive control (Johnson & Calise, 2000), and later applied to NDI by Holzapfel & Sachs, 2004, adjusts a reference model in case of unachievable commands.

3-4 Adaptive INDI

Another recent development is the use of an adaptive element in conjunction with INDI. Smeur, Chu, & De Croon, 2016 designed an attitude controller for a quadcopter that identified the control effectiveness matrix online, further reducing the method's reliance on a vehicle model. Smeur et al., 2016 further introduces a method to deal with signal delays introduced by differentiating angular rates for use in the INDI inversion loops.

Chapter 4

Vehicle Model

This chapter describes two-track 7-DOF vehicle model that was used for the calculation of the control effectiveness and the feasibility study in the preliminary phase of this thesis. It captures the most important aspects and nonlinearities that arise in vehicle dynamics and is therefore sufficient to asses the feasibility of the method.

The motion is assumed to completely planar. Furthermore, the roll and pitch angles are assumed to be small and the corresponding dynamics fast enough to approximate these states and the associated wheel normal loads, by their steady state values (Abe, 2015). The model incorporates the widely adopted Magic Formula tire model for the determination of the steady state wheel forces (H. B. Pacejka & Bakker, 1992). The behavior of the front and rear Limited Slip Differential (LSD) is described by a relatively detailed model as these parts have a large influence on the overall vehicle dynamics and later the control effectiveness calculation.

4-1 Two Track Vehicle Model

Figure 4-1 depicts the three states corresponding to the translational and rotational motion of the vehicle. In the body fixed reference frame (F_b), v_x and v_y stand for the longitudinal and lateral velocity respectively. The yaw-rate is denoted by $\dot{\psi}$. Alternatively, the vehicle motion can described in the path fixed reference frame (F_v) by the velocity V and the side-slip angle β.

The figure further depicts the individual wheel forces ${}^{w}F_{xij}$ and ${}^{w}F_{yij}$ in their respective wheel frames (F_{wij}). Where subscripts $i \in \{\mathrm{f}, \mathrm{r}\}$ and $j \in \{\mathrm{l}, \mathrm{r}\}$ denote the front or rear and left or right wheel respectively. The wheel forces, slip angles ϕ_{ij} and steering angles δ_{ij} are drawn in accordance with ISO8855, 2011. The lengths $2w_{\mathrm{f}}$ and $2w_{\mathrm{r}}$ stand for the front and rear track widths. Lastly, the front and rear parts of the wheelbase are denoted by l_{f} and l_{r} respectively.

The equations of motion for the planar vehicle model, excluding the states that describe the

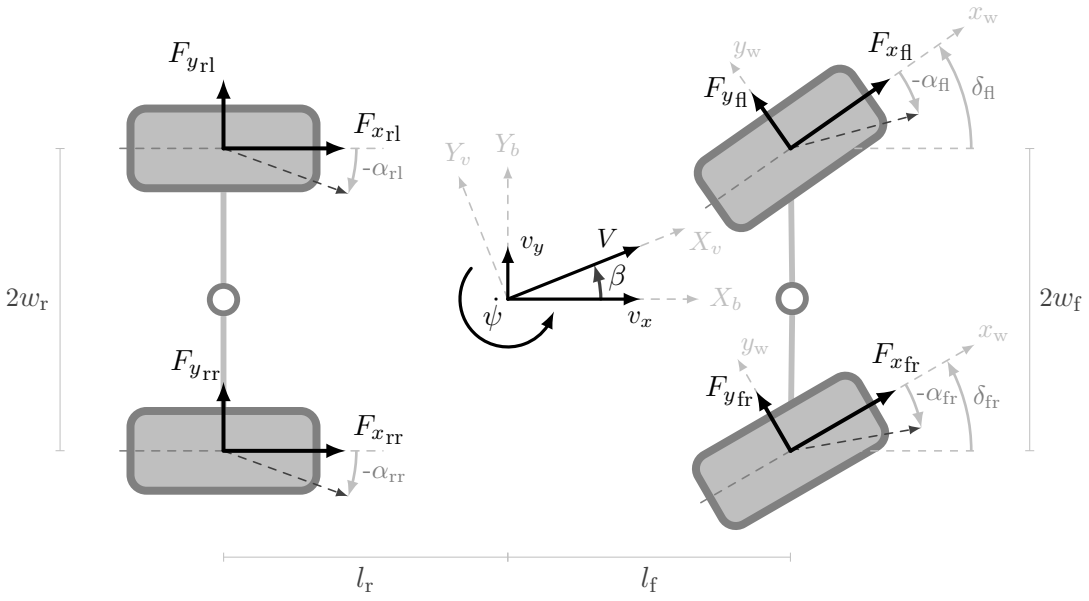

Figure 4-1: Two-track vehicle model

axle dynamics, are given by equations (4-1a)-(4-1c).

$$m(\dot{v}_x - v_y\dot{\psi}) = (F_{x_{\mathrm{fl}}} + F_{x_{\mathrm{fr}}})\cos\delta - (F_{y_{\mathrm{fl}}} + F_{y_{\mathrm{fr}}})\sin\delta + F_{x_{\mathrm{rl}}} + F_{x_{\mathrm{rr}}} \tag{4-1a}$$

$$m(\dot{v}_y + v_x\dot{\psi}) = (F_{x_{\mathrm{fl}}} + F_{x_{\mathrm{fr}}})\sin\delta + (F_{y_{\mathrm{fl}}} + F_{y_{\mathrm{fr}}})\cos\delta + F_{y_{\mathrm{rl}}} + F_{y_{\mathrm{rl}}} \tag{4-1b}$$

$$\begin{aligned} I_{zz}\ddot{\psi} \;&= -w_1\cos\delta(F_{x_{\mathrm{fl}}} - F_{x_{\mathrm{fr}}}) + l_1\cos\delta(F_{x_{\mathrm{fl}}} + F_{x_{\mathrm{fr}}}) - w_2(F_{x_{\mathrm{rl}}} - F_{x_{\mathrm{rr}}}) \\ &\quad + w_1\sin\delta(F_{y_{\mathrm{fl}}} - F_{y_{\mathrm{fr}}}) + l_1\cos\delta(F_{y_{\mathrm{fl}}} + F_{y_{\mathrm{fr}}}) - l_2(F_{y_{\mathrm{rl}}} + F_{y_{\mathrm{rr}}}) \end{aligned} \tag{4-1c}$$

Where m is the vehicle mass, I_{zz} is the moment of inertia around the z axis, $\dot{v}_x$ and $\dot{v}_y$ are the longitudinal and lateral accelerations respectively and $\ddot{\psi}$ is the yaw-acceleration.

Defining the state vector as $\mathbf{x}_{\mathrm{B}} = \begin{bmatrix} v_x & v_y & \dot{\psi} \end{bmatrix}^{\mathrm{T}}$, the equations (4-1a)-(4-1c) can be compactly expressed in matrix form as (Jonasson, 2009; Klomp, 2010),

$$\dot{\mathbf{x}_{\mathrm{B}}} = \mathbf{M}^{-1}\mathbf{E}\,{}^{\mathrm{B}}\mathbf{F} - c. \tag{4-2}$$

Where $\mathbf{M} = \mathrm{diag}\,(m, m, I_{zz})$, ${}^{\mathrm{B}}\mathbf{F} = \begin{bmatrix} {}^{b}F_{x_{\mathrm{fl}}} & {}^{b}F_{y_{\mathrm{fl}}} & \dots & {}^{b}F_{x_{\mathrm{rr}}} & {}^{b}F_{y_{\mathrm{rr}}} \end{bmatrix}^{\mathrm{T}}$, $c = \begin{bmatrix} -v_y\dot{\psi} & v_x\dot{\psi} & 0 \end{bmatrix}^{\mathrm{T}}$ and $\mathbf{E}$ is given by,

$$\mathbf{E} = \begin{bmatrix} 1 & 0 & 1 & 0 & 1 & 0 & 1 & 0 \\ 0 & 1 & 0 & 1 & 0 & 1 & 0 & 1 \\ -w_{\mathrm{f}} & l_{\mathrm{f}} & w_{\mathrm{f}} & l_{\mathrm{f}} & -w_{\mathrm{r}} & -l_{\mathrm{r}} & w_{\mathrm{r}} & -l_{\mathrm{r}} \end{bmatrix}. \tag{4-3}$$

The tire forces that occur in the local wheel frames must be rotated to the body frame. The transformation of the front-left tire forces from the wheel to the body frame ($F_w \rightarrow F_b$) front left wheel is as follows.

$$\begin{aligned} {}^{\mathrm{B}}\mathbf{F}_{\mathrm{fl}} &= \mathbb{T}_{\mathrm{B,W_{fl}}}\,{}^{\mathrm{W}}\mathbf{F}_{\mathrm{fl}} \\ \begin{bmatrix} {}^{b}F_{x_{\mathrm{fl}}} \\ {}^{b}F_{y_{\mathrm{fl}}} \end{bmatrix} &= \begin{bmatrix} \cos\delta_{\mathrm{fl}} & -\sin\delta_{\mathrm{fl}} \\ \sin\delta_{\mathrm{fl}} & \cos\delta_{\mathrm{fl}} \end{bmatrix} \begin{bmatrix} {}^{w}F_{x_{\mathrm{fl}}} \\ {}^{w}F_{y_{\mathrm{fl}}} \end{bmatrix} \end{aligned} \tag{4-4}$$

Where δ_{fl} denotes the steering angle of the front left wheel. The transformation of the complete set of tire forces, ${}^{\text{W}}\mathbf{F} = \begin{bmatrix} {}^{w}F_{x_{\text{fl}}} & {}^{w}F_{y_{\text{fl}}} & \dots & {}^{w}F_{x_{\text{rr}}} & {}^{w}F_{y_{\text{rr}}} \end{bmatrix}^{\text{T}}$, from their respective wheel frames to the body frame is given by,

$$ {}^{\text{B}}\mathbf{F} = \mathbb{T}_{\text{B,W}}\, {}^{\text{W}}\mathbf{F}. \tag{4-5} $$

Where,

$$ \mathbb{T}_{\text{B,W}} = \text{diag}\left(\mathbb{T}_{\text{B,W}_{\text{fl}}}, \mathbb{T}_{\text{B,W}_{\text{fr}}}, \mathbb{T}_{\text{B,W}_{\text{rl}}}, \mathbb{T}_{\text{B,W}_{\text{rr}}}\right) \tag{4-6} $$

If the equations of motion are expressed in terms of the velocity V and the side-slip angle β instead, equation (4-2) changes to,

$$ \dot{\mathbf{x}_{\text{B}}} = \mathbf{M}^{-1}\mathbf{E}\, {}^{\text{V}}\mathbf{F} - c \tag{4-7} $$

Where the new state vector $\mathbf{x}_{\text{B}} = \begin{bmatrix} V & \beta & \dot{\psi} \end{bmatrix}^{\text{T}}$, ${}^{\text{V}}\mathbf{F}$ are the forces and moments expressed in the velocity frame F_v, $\mathbf{M} = \text{diag}\left(m, m\,V, I_{\text{zz}}\right)$ and finally $c = \begin{bmatrix} 0 & \dot{\psi} & 0 \end{bmatrix}^{\text{T}}$.

The force transformation from the body frame to the velocity frame ($F_b \rightarrow F_v$) is given by,

$$ {}^{\text{V}}\mathbf{F} = \mathbb{T}_{\text{V,B}}\, {}^{\text{B}}\mathbf{F} \tag{4-8} $$

$$ \begin{bmatrix} {}^{v}F_x \\ {}^{v}F_y \end{bmatrix} = \begin{bmatrix} \cos\beta & \sin\beta \\ -\sin\beta & \cos\beta \end{bmatrix} \begin{bmatrix} {}^{b}F_x \\ {}^{b}F_y \end{bmatrix} $$

4-2 Normal Loads

The main/dominant assumptions of this model relate to the roll and pitch states. In the context of high performance racing, which features vehicles with stiff suspensions and low centers of gravity, these states and the associated time-constants can be assumed small (Milliken & Milliken, 1995). The roll and pitch angles can therefore be approximated by their steady state values which allows the corresponding dynamics to be omitted. Consequently, the wheel normal load distribution is approximated by its steady state value as well. Two models, for respectively the lateral and longitudinal load transfers, are used to estimate the normal forces (Abe, 2015). The front and rear roll-stiffness values, $K_{\phi\text{f}}$ and $K_{\phi\text{r}}$, are assumed to be constant. Furthermore, the location front and rear roll-centers, h_{f} and h_{r}, are assumed to be unchanging. Using these assumptions, the lateral load transfer at the front and rear axles are approximated by equations 4-9a and 4-9b.

$$ \Delta W_{y_{\text{f}}} = A_y \frac{m}{2w_{\text{f}}} \left(\frac{K_{\phi\text{f}}}{K_{\phi\text{f}} + K_{\phi\text{r}} - m\,h_{\text{s}}} + \frac{l_{\text{r}}}{l} h_{\text{f}} \right) \tag{4-9a} $$

$$ \Delta W_{y_{\text{r}}} = A_y \frac{m}{2w_{\text{r}}} \left(\frac{K_{\phi\text{r}}}{K_{\phi\text{f}} + K_{\phi\text{r}} - m\,h_{\text{s}}} + \frac{l_{\text{f}}}{l} h_{\text{r}} \right) \tag{4-9b} $$

Where, A_y is the specific force in lateral direction, h_{s} denotes the vertical distance between the roll-axis and the center of gravity and l stands for the wheel base.

The longitudinal load transfer can be calculated with equation 4-10.

$$ \Delta W_x = A_x \frac{h\,m}{l} \tag{4-10} $$

Where, A_x is the specific force in longitudinal direction and h is the height of the center of gravity.

The normal loads for each wheel can now be calculated with equations 4-11a - 4-11d.

$$F_{z\mathrm{fl}} = \frac{1}{2}\frac{mgl_\mathrm{r}}{l_\mathrm{f}+l_\mathrm{r}} - \Delta W_{y_\mathrm{f}} - \Delta W_x \tag{4-11a}$$

$$F_{z\mathrm{fr}} = \frac{1}{2}\frac{mgl_\mathrm{r}}{l_\mathrm{f}+l_\mathrm{r}} + \Delta W_{y_\mathrm{f}} - \Delta W_x \tag{4-11b}$$

$$F_{z\mathrm{rl}} = \frac{1}{2}\frac{mgl_\mathrm{f}}{l_\mathrm{l}+l_\mathrm{r}} - \Delta W_{y_\mathrm{r}} + \Delta W_x \tag{4-11c}$$

$$F_{z\mathrm{rr}} = \frac{1}{2}\frac{mgl_\mathrm{f}}{l_\mathrm{l}+l_\mathrm{r}} + \Delta W_{y_\mathrm{r}} + \Delta W_x \tag{4-11d}$$

Where the first terms in the above equations represent the static normal load distribution.

4-3 Tire Model

Tire behavior plays an essential role in vehicle dynamics analysis. It is one of the most dominant factors for the overall vehicle performance and one of the main sources of nonlinearities in the vehicle's handling characteristics. Therefore, a lot of time and effort is spent to identifying the tire-force/slip characteristics by race teams. One of the most widely adopted steady state tire models is the empirical Magic Formula (MF) (H. B. Pacejka & Bakker, 1992). In this thesis a semi empirical technique based on force normalization and pure MF force curves adopted from (H. Pacejka, 2005) is used.

In reality tire forces are a result of a complex interplay of tire deformations and adhesion and/or sliding effects at the tire-road interface (Svendenius, 2007). In empirical models like the MF or even physics based brush models, several quantities are used that reflect the state of the tire-road interaction as well as possible. If camber, turnslip, pressure effects etc. are not considered, tire forces are often described as functions of practical longitudinal slip κ_{ij}, practical lateral slip α_{ij} and the normal load F_{zij} (4-12)-(4-12).

$$F_{xij} = f(F_{zij}, \kappa_{ij}, \alpha_{ij}) \qquad i \in \{\mathrm{f,r}\},\ j \in \{\mathrm{l,r}\} \tag{4-12}$$

$$F_{y_{ij}} = g(F_{zij}, \kappa_{ij}, \alpha_{ij}) \tag{4-13}$$

The longitudinal slip or sometimes called slip ratio, is defined as the ratio between the slip velocity $v_{sxij} = v_{xij} - \omega_{ij}R_e$ and the x or longitudinal component of the wheel center's velocity expressed in the wheel frame v_{xij} (4-14). The lateral slip or tire side-slip angle is defined by the ratio of lateral and longitudinal component of the wheel center's velocity, respectively $v_{y_{ij}}$ and v_{xij} (4-15).

$$\kappa_{ij} = -\frac{v_{xij} - \omega_{ij}R_e}{v_{xij}} \tag{4-14}$$

$$\tan\alpha_{ij} = -\frac{v_{y_{ij}}}{v_{xij}} \tag{4-15}$$

Where ω is wheel angular velocity and the effective rolling radius R_e is free-rolling wheel radius defined as $R_e \equiv \frac{v_x}{\omega}\big|_{(\kappa=0)}$. The longitudinal and lateral velocity of the (front left) wheel

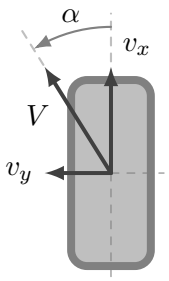

(a) Wheel side-slip angle

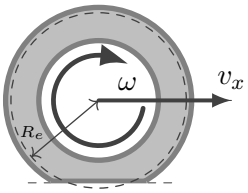

(b) Wheel slip ratio

centers, with respect to the ground, expressed in the respective wheel frame, are given by equation 4-16.

$$\begin{aligned}
\begin{bmatrix} {}^{w}v_{x_{\text{fl}}} \\ {}^{w}v_{y_{\text{fl}}} \end{bmatrix} &= \begin{bmatrix} \cos\delta_{\text{fl}} & \sin\delta_{\text{fl}} \\ -\sin\delta_{\text{fl}} & \cos\delta_{\text{fl}} \end{bmatrix} \begin{bmatrix} 1 & 0 & -w_f \\ 0 & 1 & l_f \end{bmatrix} \begin{bmatrix} v_x & v_y & \dot{\psi} \end{bmatrix}^{\text{T}} \\
{}^{\text{W}}\mathbf{v}_{\text{fl}} &= \begin{bmatrix} \cos\delta_{\text{fl}} & \sin\delta_{\text{fl}} \\ -\sin\delta_{\text{fl}} & \cos\delta_{\text{fl}} \end{bmatrix} \begin{bmatrix} {}^{b}v_{x_{\text{fl}}} \\ {}^{b}v_{y_{\text{fl}}} \end{bmatrix} \\
{}^{\text{W}}\mathbf{v}_{\text{fl}} &= \left(\mathbb{T}_{\text{B,W}_{\text{fl}}}\right)^{\text{T}} {}^{\text{B}}\mathbf{v}_{\text{fl}}
\end{aligned} \tag{4-16}$$

Collecting all the wheel velocities in the vector ${}^{\text{W}}\mathbf{v} = [v_{x_{\text{fl}}}\, v_{y_{\text{fl}}}\, v_{x_{\text{fr}}} \ldots v_{x_{\text{rr}}}\, v_{y_{\text{rr}}}]^{\text{T}}$, and noting the structure of the matrix $\mathbf{E}$, the calculation of the all the wheel velocities can be conveniently written as,

$${}^{\text{W}}\mathbf{v} = \left(\mathbb{T}_{\text{B,W}}\right)^{\text{T}} \mathbf{E}^{\text{T}} \mathbf{x}_{\text{B}}. \tag{4-17}$$

4-3-1 Magic formula and Similarity Method

The similarity method is based on the premise that the pure force-slip characteristic for *different* conditions looks approximately the same when normalized. The force-slip characteristic is normalized at some reference normal force, after which the normalized curved can be appropriately scaled to represent different driving conditions. H. Pacejka, 2005 uses a MF like function as a reference but other characteristic curves could in principle be employed.

In pure lateral or longitudinal slip the MF is given by equation 4-18.

$$F_i(\phi) = D_i \sin\left[C_{i_0} \arctan\left\{B_i\phi - E_{i_0}(B_i\phi - \arctan(B_i\phi))\right\}\right] \quad i \in \{x, y\},\ \phi \in \{\alpha, \kappa\} \tag{4-18}$$

In this work, the shape parameters C_{i_0} and E_{i_0} are defined at some the nominal load F_{z_0} and assumed constant throughout the operating range of the tire. The stiffness factor B_i and peak force D_i are given by,

$$B_i = C_{F_i}/(C_{i_0} D_i) \tag{4-19}$$

$$D_i = \mu_i F_z \tag{4-20}$$

The remaining parameters μ_i and C_{F_i}, denote the friction coefficient and the initial force-slip slope or slip stiffness, respectively.

One might expect the slip stiffness and the peak force to vary proportionally with the normal load. Instead, both increase less than proportional with normal load, i.e, the friction coefficient decreases as the normal load increases. This effect, observed with pneumatic tires and

usually referred to as tire load sensitivity, has a large effect on vehicle performance through load transfers. Both the friction coefficient and the slip stiffness are therefore modeled as functions of normal load. Equations 4-21 and 4-22 describe the lateral slip stiffness and friction coefficient.

$$C_{Fy}(F_z) = c_{y1} F_{z0} \sin\left[c_{y2} \arctan\left\{F_z/(c_{y3} F_{z0})\right\}\right] \tag{4-21}$$

$$\mu_y(F_z) = \mu_{y0} + c_{y4}\left(F_z - F_{z0}\right)/F_{z0} \tag{4-22}$$

Where μ_{y0} stands for the nominal friction coefficient. The longitudinal slip stiffness $C_{F\kappa}$ and friction coefficient μ_x are described by equations 4-23 and 4-24.

$$C_{Fx}(F_z) = F_z\left(c_{x1} + c_{x2}\left(F_z - F_{z0}\right)/F_{z0}\right) e^{c_{x3}(F_z - F_{z0})/F_{z0}} \tag{4-23}$$

$$\mu_x(F_z) = \mu_{x0} + c_{x4}\left(F_z - F_{z0}\right)/F_{z0} \tag{4-24}$$

The parameters c_{i1} - c_{i4} can be found through tire testing.

Nondimensionalization and Rescaling

The non-dimensionalized reference curve is obtained by first normalizing equation 4-18 with the nominal peak force D_i, subsequently multiplying its argument ϕ with the nominal slip stiffness C_{Fi} and lastly dividing ϕ by the peak force (4-25). The resulting normalized force-slip characteristic is given by equation 4-26.

$$F_{i\mathrm{n}}(\phi) = \frac{1}{\mu_{i0} F_{z0}} F_i \left(\frac{C_{Fi0}}{\mu_{i0} F_{z0}}\phi\right)\Bigg|_{F_z = F_{z0}} \tag{4-25}$$

$$F_{i\mathrm{n}}(\phi) = \sin\left[1/B_{i\mathrm{n}} \arctan\left\{B_{i\mathrm{n}}\phi - E_{i0}\left(B_{i\mathrm{n}}\phi - \arctan(B_{i\mathrm{n}}\phi)\right)\right\}\right] \tag{4-26}$$

Where the new coefficient $B_{i\mathrm{n}} = 1/C_{i0}$ and E_{i0} is equivalent to its previous definition.

By appropriately rescaling equation 4-26, the pure slip curves can be obtained for different normal loads. The normalized slip curve is first multiplied by the peak force under the new driving conditions $\mu_i(F_z)F_z$, next the argument ϕ normalized by the slip stiffness $C_{Fi}(F_z)$ and finally, ϕ is multiplied by the peak force. The resulting relation can be used to evaluate the wheel forces in pure slip under different normal loads (4-27).

$$F_i(\phi, F_z) = \left(\mu_i(F_z)\cdot F_z\right)\cdot F_{i\mathrm{n}}\left(\frac{\mu_i(F_z)\cdot F_z}{C_{Fi}(F_z)}\phi\right) \tag{4-27}$$

Combined Slip

So far only pure slip conditions have been considered. In order to model combined slip, the theoretical slip values σ_x and σ_y are defined as,

$$\sigma_x = \frac{\kappa}{1+\kappa} = \frac{\omega R_e - v_x}{\omega R_e} \tag{4-28}$$

$$\sigma_x = \frac{\tan\alpha}{1+\kappa} = -\frac{v_y}{\omega R_e} \tag{4-29}$$

The magnitude of the slip vector σ is given by equation 4-30.

$$\sigma = \sqrt{\sigma_x^2 + \sigma_y^2} \tag{4-30}$$

Using the slip magnitude, the longitudinal and lateral force in combined slip can now be approximated with equations 4-31 and 4-32.

$$F_{xij} = f(F_{zij}, \sigma_{xij}, \sigma_{xij}) = (\mu_x(F_z) \cdot F_z)\frac{\sigma_x}{\sigma} F_{x\mathrm{n}}\left(\sigma_{eq}^x\right) \qquad i \in \{\mathrm{f,r}\},\ j \in \{\mathrm{l,r}\} \tag{4-31}$$

$$F_{y_{ij}} = g(F_{zij}, \sigma_{xij}, \sigma_{xij}) = (\mu_y(F_z) \cdot F_z)\frac{\sigma_y}{\sigma} F_{y_\mathrm{n}}\left(\sigma_{eq}^y\right) \tag{4-32}$$

Where the equivalent theoretical slip values σ_{eq}^x and σ_{eq}^y are given by equations 4-33 and 4-34.

$$\sigma_{eq}^x = \frac{\mu_x(F_z) \cdot F_z}{C_{Fx}(F_z)}\sigma \tag{4-33}$$

$$\sigma_{eq}^y = \frac{\mu_y(F_z) \cdot F_z}{C_{Fy}(F_z)}\sigma \tag{4-34}$$

Dynamic Tire Behavior

Tire forces do not occur instantaneously. Instead, tires require a certain rolling distance to build up tire forces. During this time, sliding and adhesion phenomena in the contact patch settle and the carcass deflection -through which forces are transferred from the contact patch to the wheel rim, reaches a steady state. A simple way to approximate the transient tire behavior is by introducing first order dynamics to the slip build-up (Svendenius, 2007). Assuming small slips, no camber angle and neglecting damping effects in the tire carcass, the tire dynamics may be approximated by equation 4-35.

$$\frac{l_i}{v_x}\dot{\phi} = \phi - \phi' \qquad i \in \{x, y\}\ ,\ \phi \in \{\alpha, \kappa\} \tag{4-35}$$

In the time constant of this low-pass filter, l_i is referred to as the relaxation length. Under the assumed conditions the relaxation length can be related to the slip stiffness C_{Fi} and carcass deflection stiffness in the corresponding direction $C_{\mathrm{c}i}$ as,

$$l_i \approx \frac{C_{Fi}(F_z)}{C_{\mathrm{c}i}}. \tag{4-36}$$

In reality the tire dynamics are more complex but this approach serves as a good first order approximation of the tire dynamics. In the context of vehicle stability control, tire dynamics can be compared to a form of actuator dynamics and might be significant at lower speeds. However, because its small time-constant, this effect is most often neglected.

4-4 Limited Slip Differential Model

The differential is an integral part of most road vehicles. It connects the left and right wheels on a driven axle with the prop-shaft coming from the engine and is responsible for distributing

the engine torque over both sides. The design of a differential greatly this influences this torque split and therefore the dynamic behavior of the vehicle.

The open differential distributes the input torque evenly over both tires while allowing the wheels to rotate independently if inertial forces of the internal gearing are neglected. This in contrast with a rigid axle or spool, which constrains the wheels to rotate at the same velocity. Especially in tight corners, this causes the inside wheel to 'drag' along the road surface resulting in high slips and accelerated tire-wear.

However, the extra degree of freedom of an open differential comes with a downside. In situations where one of the wheels loses traction, the wheel with the least traction will start to accelerate quickly. The rapid acceleration of the power-train results in a decline of torque experienced at the differential. Not much later, the power limit of the engine will be reached and the input torque at the differential will decrease accordingly. The wheel with grip will experience the same torque reductions, leading to a decrease in overall longitudinal acceleration. This is an obvious disadvantage when trying to accelerate on slippery surfaces with low traction. A similar situation occurs when accelerating out of a corner and one of the inside wheels experiences low traction due to large load transfers. This highly undesirable effect can be mediated by using a limited slip differential which allows some torque to be transferred from the faster spinning wheel to the slower spinning wheel.

Figure 4-3 shows a cross-section of an open differential. The prop-shaft's rotation, denoted by ω_s, is transferred to the differential casing through the drive gear. In an open differential the casing is not directly attached to the drive-shafts. Instead, its rotation ω_c causes the pinions J_d to move around axis A-B. It is this rotation that in turn causes the two drive-shafts to rotate with velocities ω_l and ω_r, through a bevel gear set. Because angular velocity of the pinion, ω_d, is unconstrained, the torque distribution is kept equal and the relative velocity of both axles is not restricted as mentioned before. In a limited slip differential an extra load path from the casing to the drive-shafts is created using some friction based system. In a Salisbury type differential the pinion is not directly attached to the differential casing. Rather, the differential casing first moves two halves of an insert that is forced to rotate with the casing but can translate along axis A-B. When the two halves rotate, they move the pinion similar to the open differential described before. The force on the interface between the two inserts and the pinion also pushes the two halves away from each other, compressing a clutch pack assembly attached to the casing and the drive-shafts. The resulting friction force opposes the relative velocity of the drive axles and tries to make them and the differential casing move as one. Another way of looking at this is that, compared to the open differential, some torque is transferred from the faster rotating wheel to the slower rotating wheel. Figure 4-4 shows how the two halves are pushed outward. The angle of the ramp influences the ratio of the two force components and thus determines how strong the clutch pack is compressed and therefore how much force can be transferred. Note that the angle of the two ramps can be different, resulting in distinct locking ratios for coasting and driving.

4-4-1 Model Description

The limited slip differential model described in this chapter is adopted from Forstinger, Bauer, & Hofer, 2015; Morselli, Zanasi, & Sandoni, 2006. The system under consideration features two LSDs in the front and rear of the car. Although the specifications of the front and rear

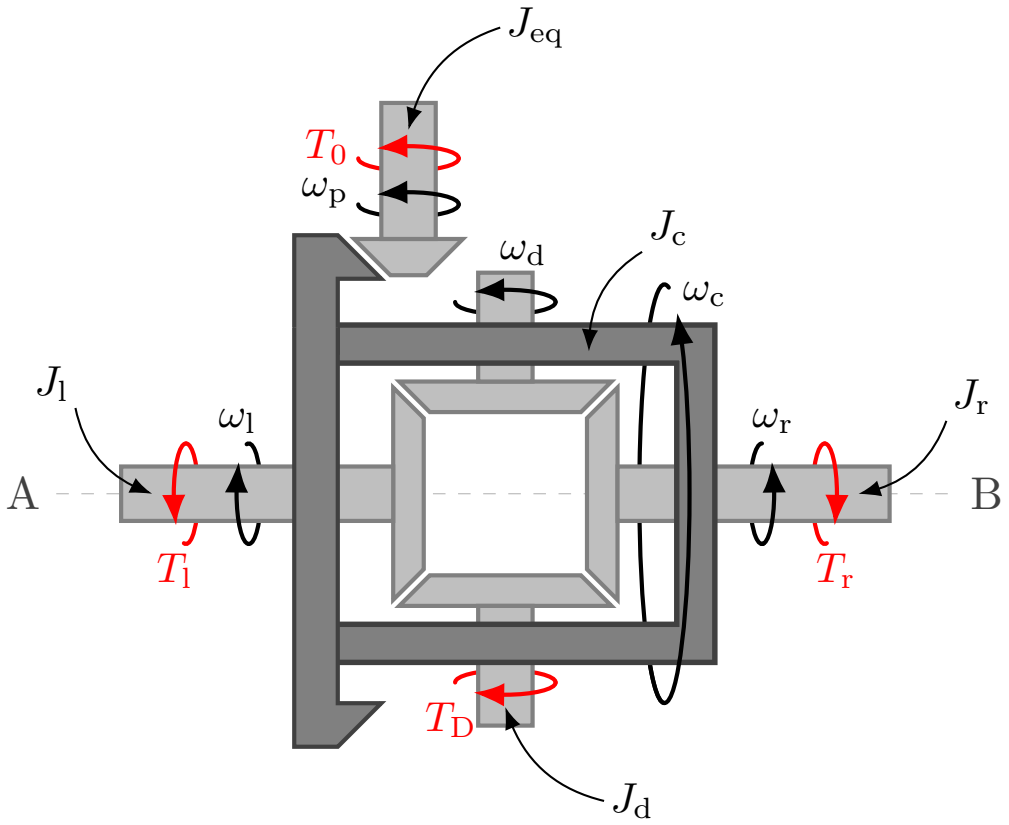

Figure 4-3: Cross section of an open differential

power-trains are distinct, they can be modeled in the same way and therefore the model is treated here only once.

Assuming that all the gear ratios depicted in Figure 4-3 are 1 : 1, the structure is infinitely stiff and no backlash is present, the motion of the differential satisfies the following constraints.

$$\omega_s = \omega_c \tag{4-37}$$
$$\omega_l = \omega_p + \omega_d \tag{4-38}$$
$$\omega_r = \omega_p - \omega_d \tag{4-39}$$

Another equivalent but more intuitive set of constraints can be obtained by adding and subtracting equation 4-38 and 4-39, resulting in relations 4-40 and 4-41.

$$2\omega_p = \omega_l + \omega_r \tag{4-40}$$
$$2\omega_d = \omega_l - \omega_r \tag{4-41}$$

Equation 4-40 and 4-37 state that both the prop-shaft and the differential-casing rotate at the average angular velocity of the left and right drive-shaft. The pinions, J_d, rotate at half angular velocity delta between the left and the right axle as can be seen from Equation 4-41. The complete state of the differential can now be described by just two variables. For reasons that will become clear later, the set of state-variables is chosen to be $\{\omega_p, \omega_d\}$.

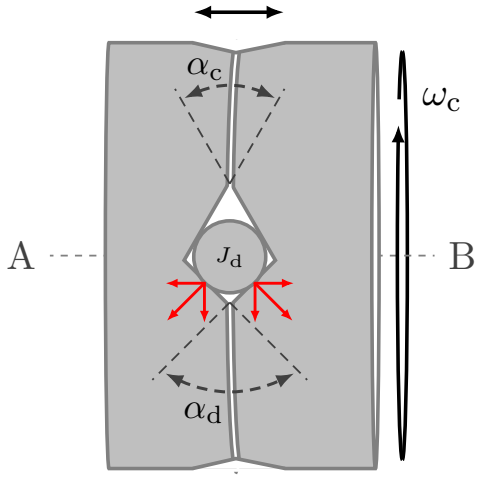

Figure 4-4: Salisbury type differential inserts

Limited slip action can be modeled by a friction force, T_D, that counteracts the motion of J_d or in other words resists the relative motion between the left and the right drive-shafts. Similarly, by adding a friction force, T_L, to the prop-shaft the remaining friction losses are included. The equations of motion for the differential are now given by,

$$\begin{aligned}\dot{\omega}_p = &- \frac{(2J_l - J_d)\,T_r + (2J_r - J_d)\,T_l}{D} \\ &+ \frac{(J_l + J_r + J_d)\,(T_s - T_L)}{D} - \frac{(J_l - J_r)\,T_D}{D}\end{aligned} \tag{4-42}$$

$$\begin{aligned}\dot{\omega}_d = &\frac{(2J_l - J_d)\,T_r - (2J_r - J_d)\,T_l}{D} \\ &- \frac{(J_l + J_r + J_d)\,T_D}{D} + \frac{(J_l - J_r)\,(T_s - T_L)}{D}\end{aligned} \tag{4-43}$$

Where the denominator is given by,

$$D = 4J_lJ_r + (J_l + J_r)\,J_d + (J_l + J_r + J_d)\,(J_s + J_c) \tag{4-44}$$

Assuming an infinitely stiff connection between the differential and the wheels, the inertia of the right and the left wheels and their respective drive shafts can be lumped into J_l and J_r. The input torques T_l and T_r now represent the external torques resulting from the left and right tire forces respectively. Assuming $J_l = J_r = J$, the last terms of both equation 4-42 and 4-43 vanish. The cross dependence of the two states on the friction forces disappears and the state equations are given by,

$$\dot{\omega}_p = \frac{T_s - T_l - T_r - T_L}{2J + J_c + J_p} \tag{4-45}$$

$$\dot{\omega}_d = \frac{-T_D - T_l + T_r}{2J + J_d} \tag{4-46}$$

The effect of the locking torque T_D and the friction loss T_L on the torque distribution, can be examined in steady state by equating equations 4-45 and 4-46 to zero and solving for T_l

and T_r. The resulting steady state wheel torques are given by,

$$T_{\mathrm{l}_{\mathrm{ss}}} = 1/2\,(T_\mathrm{p} - T_\mathrm{L} - T_\mathrm{D}) \tag{4-47}$$

$$T_{\mathrm{r}_{\mathrm{ss}}} = 1/2\,(T_\mathrm{p} - T_\mathrm{L} + T_\mathrm{D}) \tag{4-48}$$

These equations reveal why the limited slip differential is said to transfer torque from one wheel to another.

4-4-2 Friction,Sliding or Sticking and Order Reduction

The friction forces are approximated with a coulomb friction model and a distinction is made between static and kinetic friction. If the left and the right axles have nonzero relative velocity ($\omega_\mathrm{l} \neq \omega_\mathrm{r}$), i.e., the LSD is slipping, the friction force T_D is given by equation 4-49.

$$T_{\mathrm{D_c}} = \max\left(T_{\mathrm{D_{c0}}}, r_{\mathrm{D_c}} \cdot |T_\mathrm{s}|\right) \cdot \mathrm{sng}\left(\omega_\mathrm{d}\right) \tag{4-49}$$

Where $T_{\mathrm{D_{c0}}}$ is a minimum constant term depending on the preload settings of the differential. The second term, $r_{\mathrm{D_c}} \cdot |T_\mathrm{s}|$, represents the friction force resulting from a driving or coasting torque. The factor $r_{\mathrm{D_c}}$ depends on, e.g, friction surface size and the angle of the ramps depicted in figure 4-4. The friction force F_L is modeled in a similar manner, with a constant minimum friction force and a component that depends on the input torque T_s (4-50).

$$T_{\mathrm{L_c}} = \max\left(T_{\mathrm{L_{c0}}}, r_\mathrm{L} \cdot |T_\mathrm{s}|\right) \cdot \mathrm{sng}\left(\omega_0\right) \tag{4-50}$$

From equations 4-46 and 4-49 can be deduced that if the differential is slipping and the condition

$$|T_{\mathrm{D_c}}| \geq |T_\mathrm{r} - T_\mathrm{l}| \tag{4-51}$$

continues to hold, $\omega_\mathrm{d} \to 0$ in finite time. Or in other words, if the maximum friction force is larger in magnitude than the resultant moment of the left and right input torques, the relative velocity both drive-shafts will be brought to zero. Once ω_d reaches zero, it enters a sliding mode, where the sliding condition is enforced by the switching function in equation 4-49. Simulating this sliding mode can be troublesome because ideally the switching should be instantaneous and occur at infinite frequency (Slotine et al., 1991).

Alternatively, the model order be adjusted to account for sticking and sliding conditions. Once their relative velocity is zero, the left and right drive-shafts move as a single body. The equations that describe the 'sticking' motion are therefore of reduced order as long they are represented by an average motion and $n-1$ relative motions (Zanasi, Sandoni, & Morselli, 2001). This further reinforces the choice for $\{\omega_\mathrm{p}, \omega_\mathrm{d}\}$ as opposed to $\{\omega_\mathrm{l}, \omega_\mathrm{r}\}$ as state variables.

Under sticking conditions, the friction force is bounded by its maximum static value, $F_{\mathrm{D_{max}}}$. Static forces $F_{\mathrm{D_{max}}}$ and $F_{\mathrm{L_{max}}}$ are defined similar to the kinetic friction described before. The magnitude and direction of T_D will be such that the relative velocity remains zero, i.e., such that $\dot{\omega}_\mathrm{d} = 0$ as long as the moment required does not exceed $F_{\mathrm{D_{max}}}$.

Morselli et al., 2006; Forstinger et al., 2015 describe four cases based on the sticking or slipping conditions of a differential. Assuming that $J_\mathrm{l} = J_\mathrm{r} = J$ and the transmission ratios are $1:1$ the of the cross dependence of the two states on the friction forces disappears. The cases described here are therefore simplified.

- Case 1: $\omega_\mathrm{p} \neq 0, \omega_\mathrm{d} \neq 0$
  Both states are non-zero, therefore no sticking of the moving parts occurs. The motion of the differential is described by both equations (4-45) and (4-46). Therefore, the differential torque transfer and torque due to friction losses are given by,
  $$T_\mathrm{D} = T_{\mathrm{D_c}}$$
  $$T_\mathrm{L} = T_{\mathrm{L_c}}$$

- Case 2: $\omega_\mathrm{p} \neq 0, \omega_\mathrm{d} = 0$
  The prop-shaft's rotational velocity is non-zero and friction force T_L is given by it's dynamic value,
  $$T_\mathrm{L} = T_{\mathrm{L_c}}.$$
  The relative velocity between the left and right wheel is zero, the differential is said to be locked. Substituting $\omega_\mathrm{d} = 0$ into constraints 4-38 and 4-39 gives $\omega_\mathrm{l} = \omega_\mathrm{r} = \omega_\mathrm{p}$, i.e., the bodies of the prop-shaft and the wheels move as one. The associated dynamics can now be described by a single equation (4-45) or in other words, the order of the system is reduced by one.

  As long as the torque required to maintain this condition ($\dot{\omega}_\mathrm{d} = 0$) is less than the maximum static friction force, the relative velocity between the left and right wheel stays zero. The required torque follows from equation 4-46 and is simply given by,
  $$\tilde{T_\mathrm{D}} = -T_\mathrm{l} + T_\mathrm{r} \tag{4-52}$$
  The resulting friction force can now be expressed as,
  $$T_\mathrm{D} = \begin{cases} \tilde{T_\mathrm{D}} & \text{if,} \quad |\tilde{T_\mathrm{D}}| \leq F_{\mathrm{D_{max}}} \\ F_{\mathrm{D_{max}}} \mathrm{sgn}(\tilde{T_\mathrm{D}}) & \text{otherwise.} \end{cases} \tag{4-53}$$

- case 3: $\omega_\mathrm{p} = 0, \omega_\mathrm{d} \neq 0$
  This case is very similar to case 2. The torque transfer T_D is given by its dynamic value,
  $$T_\mathrm{D} = T_{\mathrm{D_c}}.$$
  The friction loss torque T_L is given by,
  $$T_\mathrm{L} = \begin{cases} \tilde{T_\mathrm{L}} & \text{if,} \quad |\tilde{T_\mathrm{L}}| \leq F_{\mathrm{L_{max}}} \\ F_{\mathrm{L_{max}}} \mathrm{sgn}(\tilde{T_\mathrm{L}}) & \text{otherwise.} \end{cases} \tag{4-54}$$
  Where, from equation 4-45,
  $$\tilde{T_\mathrm{L}} = T_\mathrm{in} - T_\mathrm{l} - T_\mathrm{r} \tag{4-55}$$
  The reduced order dynamics are described by equation 4-46.

- case 4: $\omega_\mathrm{p} = 0, \omega_\mathrm{d} = 0$
  This case is the least interesting from a control design perspective. Both states are zero and remain zero if the maximum friction forces are large enough. Under the previously stated assumptions, no cross-coupling exists between the states and friction forces and the friction forces are simply given by equation 4-53 and 4-54.

The cases descried above determine the torque distribution created by limited slip differential and therefore have a large influence on the vehicle dynamics. Specifically, switching from case 1 to 2 and vice versa will play a dominant role in the choice of control system structure and the determination of the control effectiveness.

4-4-3 Power-Train

To include the inertia of the combustion engine, motor-generator-unit and the transmission, equations 4-45 and 4-46 are rewritten as,

$$\dot{\omega}_{\mathrm{p}} = \frac{K_{\mathrm{t}} T_0 - T_{\mathrm{l}} - T_{\mathrm{r}} - T_{\mathrm{L}}}{J_{\mathrm{eq}} + J_{\mathrm{s}} + 2J + J_{\mathrm{c}}} \tag{4-56}$$

$$\dot{\omega}_{\mathrm{d}} = \frac{-\tilde{T}_{\mathrm{D}} - T_{\mathrm{l}} + T_{\mathrm{r}}}{2J + J_{\mathrm{d}}} \tag{4-57}$$

Where the constant K_{t}, is the total transmission gain and J_{eq} is an equivalent inertia that includes both the inertia of the power-unit and transmission, incorporating the effect transmission-ratios. The torque T_0 represents the torque acting on the power-unit.

So far it was assumed that this input-torque and the torque experienced at the differential, resulting in friction torque $T_{\mathrm{D_c}}$, are equal. In reality, $T_{\mathrm{D_c}}$ is not a function of the input torque T_0 directly, but should be discounted by the inertial effects arising from the power-unit and transmission during transients. The resulting friction torque $\tilde{T}_{\mathrm{D_c}}$ is given by,

$$\tilde{T}_{\mathrm{D_c}} = \max\left(T_{\mathrm{D_{c0}}}, r_{\mathrm{D_c}} \cdot \left| \frac{K_{\mathrm{t}} T_0 \cdot 2J_{\mathrm{w}} + (T_{\mathrm{l}} + T_{\mathrm{r}})(J_{\mathrm{s}} + J_{\mathrm{eq}} + J_{\mathrm{c}})}{2J + J_{\mathrm{s}} + J_{\mathrm{eq}} + J_{\mathrm{c}}} \right| \right) \cdot \mathrm{sgn}(\omega_{\mathrm{d}}) \tag{4-58}$$

Note that although equation 4-58 replaces equation 4-49, the cases described above are unaffected.

Chapter 5

Controller Design

The objective of the control system is to aid the driver in achieving the fastest lap times or more specifically to decrease the workload associated with controlling a high performance vehicle at the edge of its stable envelope, while maintaining or even increasing the performance of the driver. To this end, a cascaded side-slip and yaw-rate envelope protection system is developed in combination with a model following yaw-rate controller that acts inside the stable region of the state-space. A control allocation algorithm protects the tires from being overused while stabilizing the vehicle and reaching an overall torque request. This chapter firstly discusses the basic structure of the control system and its individual parts in separate sections. The concluding section provides a description of the envelope protection system and the yaw-rate set-point generator.

5-1 Cascaded control structure

A prerequisite for the use of a cascaded control structure is the existence of different time scales in the controlled dynamical system (). Time scale separation occurs when a system exhibits 'fast' and 'slow' dynamics and is extensively studied in the context of singular perturbed system analysis (Kokotovic, O'malley, & Sannuti, 1976). Loosely speaking it means that in the slow time scale, the fast dynamics can be approximated by their steady state value. Inversely, in the fast time scale, the slow dynamics are approximately constant. This principle can be used in control system design by controlling the slow and the fast dynamics separately and letting the output of the fast dynamics serve as the input for the slow dynamics. In other words the set-point of the fast feedback loop is the output of the slower or outer feedback loop.

In general this greatly simplifies the design an inversion based controller, which would otherwise involve the repeated differentiation and subsequent inversion of equations 4-2, 4-45 and 4-46 including the tire model. The nature of INDI ordinarily requires a cascaded structure if the control input does not directly appear in the time derivative of the controlled output, further reinforcing the choice of control system structure.

Time-scale separation in combination with inversion techniques has been used successfully in aircraft control where the existence of different time scales between the aerodynamic angles and the angular rates (Snell, Enns, & Garrard, 1992; Reiner, Balas, & Garrard, 1996) or the attitude angles and angular rates (Sieberling et al., 2010), is well-established. Most of the references on automotive stability control included here assume that the dynamics associated with controlling the wheel forces are fast enough to be separated from the yaw dynamics or can be neglected entirely. If a form of traction control is used to regulate the wheel forces, the dynamics of the entire power-train should be considered when making this assumption. The equivalent inertia of the power train, that is including the engine/mgu inertia and transmission ratios, might slow down the dynamics such that the separation between the bandwidths of the power-train and yaw dynamics becomes too small. On the other hand Schumacher, Khargonekar, & McClamroch, 1998 prove that in the case of a constant outer-loop set-point, sufficient time scale separation can be achieved by speeding up the inner-loop by increasing the associated gains.

Table 5-1: Estimated bandwidths of the power-train and yaw dynamics

	Front (V=30.2 m/s, $\dot{\psi}$=0.135 rad/s)	*Rear* (V=29.9 m/s, $\dot{\psi}$=0.119 rad/s)
	bandwidth ω_{bw} rad/s	bandwidth ω_{bw} rad/s
ω_{p}	126.58	232.56
$\dot{\psi}$	18.52	19.87

Although the instantaneous bandwidth separation between the body and power-train dynamics is not constant throughout the state-space of the nonlinear vehicle model, table 5-1 provides some insight into the separation between these subsystems at a nominal quasi-steady state condition. The estimated bandwidths approximately differ by a factor 7 and 12 for the front and rear axle respectively. Although the front drive train has markedly less inertia than the rear, the high gear ratio in the front leads to a high effective inertia and a relatively low bandwidth. Both ratios are assumed to be large enough to adopt a cascaded control structure. Therefore, the proposed structure is such that the prop-shaft velocities, yaw-rate and side-slip are controlled in respectively an inner-loop, middle-loop and outer-loop. The following sections elaborate the design of each loop separately.

5-2 Prop-Shaft Velocity Controller

The inner loop of the proposed structure controls the prop shaft velocities on the front and rear axles. Rather than controlling the wheel speeds directly, the wheel-speeds are therefore influenced indirectly through the front and rear differentials. Chapter 6 explains how the desired moments required for yaw-rate can still be achieved. The low level controller incorporates a INDI control scheme based on the state equations 4-56 that describe the dynamics of the power-train.

$$\dot{\omega}_{\text{p}} = \frac{K_{\text{t}} T_0 - T_{\text{l}} - T_{\text{r}} - T_{\text{L}}}{J_{\text{eq}} + J_{\text{p}} + 2J + J_{\text{c}}}$$

Combining the front and rear prop-shaft dynamics in a single equation, neglecting the friction forces and linearizing around $\boldsymbol{\omega}_{\mathrm{s}0}$ results in,

$$\dot{\boldsymbol{\omega}}_{\mathrm{p}} = \dot{\boldsymbol{\omega}}_{\mathrm{p}0} + \mathbf{J}\left.\frac{\partial \mathbf{F}_x}{\partial \boldsymbol{\omega}_{\mathrm{s}}}\right|_{(\mathbf{x}_0,\,\mathbf{u}_0)} (\boldsymbol{\omega}_{\mathrm{p}} - \boldsymbol{\omega}_{\mathrm{p}0}) + \mathbf{J}K_{\mathrm{t}}(T_{\mathrm{s}} - T_{\mathrm{p}0}). \tag{5-1}$$

Where the prop-shaft velocity vector is given by $\boldsymbol{\omega}_{\mathrm{p}} = [\omega_{\mathrm{sf}},\, \omega_{\mathrm{pr}}]^{\mathrm{T}}$ and the drive torque vector $T_{\mathrm{p}} = \left[T_{\mathrm{pf}},\, T_{\mathrm{p_r}}\right]^{\mathrm{T}}$. The second term of equation 5-1 is the result of linearizing the wheel toques, T_{l} and T_{r}. Therefore, matrix $\frac{\partial \mathbf{F}_x}{\partial \boldsymbol{\omega}_{\mathrm{p}}}$ contains a linearization of the tire force characteristics as described in Chapter 4. Furthermore, diagonal matrices $\mathbf{J}$ and K_{t} have the corresponding inertia's and transmission ratio's on their diagonals respectively. Lastly, $\dot{\boldsymbol{\omega}}_{\mathrm{p}0}$ denotes the current prop-shaft angular acceleration.

Corresponding to the methods described in Chapter 3, by letting $\dot{\omega}_{\mathrm{p}}$ be the virtual control ν_ω, equation 5-1 can be used to find a linear differential relation between the controlled variable ω_{p} and ν_ω. Furthermore, if the control rate is sufficiently high, the time-scale separation principle dictates that the term containing the linearized tire model can be neglected as the change in prop-shaft velocity over each time-step becomes negligible compared to the changes in the control input, i.e. $(\boldsymbol{\omega}_{\mathrm{p}} - \boldsymbol{\omega}_{\mathrm{p}_0}) \approx \mathbf{0}$. The resulting relation can be solved for the control increment ΔT_{p} giving,

$$\Delta T_{\mathrm{s}} = K_{\mathrm{t}}^{-1}\mathbf{J}^{-1}\left(\nu_\omega - \dot{\boldsymbol{\omega}}_{\mathrm{p}0}\right) \tag{5-2}$$

Torque increment ΔT_{s} represents the torque increment required to reach the desired propshaft acceleration set by the virtual control. The commanded torque is therefore given by,

$$T_{\mathrm{pc}} = T_{\mathrm{pf}} + \Delta T_{\mathrm{p}}. \tag{5-3}$$

Where T_{pf} is the current measured or estimated current torque set-point.

If Equation 5-2 and 5-3 are applied to 5-1, the equation is approximately linearized. In other words, under the aforementioned assumptions an approximate linear differential relation exists between the prop-shaft velocity and the virtual control, i.e.,

$$\dot{\omega}_{\mathrm{p}} \approx \nu_\omega. \tag{5-4}$$

Therefore, a simple linear controller suffices to control the system with ν_ω. In the prop-shaft velocity loop, this linear controller is a simple gain K_ω. Note that the approximate linearization does not depend on the tire-forces and therefore does not necessitate the inversion of a complex tire-model as required by NDI, greatly simplifying the inversion process. Furthermore, matrix $\mathbf{J}$ and K_{t} depend solely on the transmission ratio's and equivalent inertia's and therefore what gear the car is in, but are otherwise constant.

However, Equation does 5-2 require differentiating a measurement or estimate of the prop-shaft velocity as no direct prop-shaft acceleration measurement is available. To facilitate the differentiation of a potentially noisy signal, the prop-shaft velocity measurement is filtered by a second order low-pass filter, $\mathbf{H}(z)$. Smeur et al., 2016 demonstrate that $\mathbf{H}(z)$ has to be applied to the measurement or estimate of the current control input in order to guarantee the stability of the system.

A schematic of the control structure is presented in Figure 5-1. The block $\mathbf{E}(z)$ represents the actuator dynamics, comprising the behavior of both the electric motor in the front and the combustion engine in the rear of the car, which are assumed to be known. Block **VD** corresponds to the remaining vehicle dynamics and the effectiveness $\mathbf{J}K_{\mathrm{t}}$ is abbreviated as $\mathbf{G}_\omega$. Note that the subscripts have been dropped where it did not cause any ambiguity.

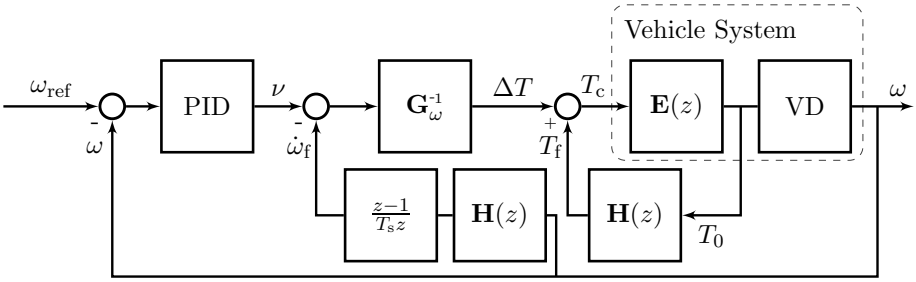

Figure 5-1: Schematic of the Prop-Shaft velocity controller

5-2-1 Pseudo Control Hedge

The prop-shaft velocity controller further incorporates Psuedo Control Hedging (PCH), a technique first introduced in the context of Model Reference Adaptive Control (MRAC) to address the problems associated with model adaptation in the presence of actuator (rate-) saturation (Johnson, 2000). A reference model or command filter is adjusted or 'hedged' with the error between the commanded and actual virtual control signals such that reference signal more closely resembles the system dynamics permissible by the actuator. In case of MRAC the adaptive element is prevented from adjusting in areas of actuator (rate-) saturation and is kept from compensating for linear actuator dynamics.

PCH has been demonstrated advantageous outside the context of adaptive control. Lombaerts, Looye, Chu, & Mulder, 2010 proposed PCH in conjunction with NDI as means for flight envelope protection and PCH improved controller performance when used with INDI in the presence actuator dynamics and saturation (Simplicio et al., 2013).

In case of a first order linear reference model, the hedged reference dynamics are given by,

$$\dot{\mathbf{x}}_{\text{r}} = K_{\text{p}}(\mathbf{x}_{\text{c}} - \mathbf{x}_{\text{r}}) - \boldsymbol{\nu}_{\text{h}}. \tag{5-5}$$

Where the diagonal gain matrix K_{p} is chosen such that the time constant of the command filter reflects the desired dynamics of the controlled system. The PCH signal ν_{h}, when used in conjunction with INDI, is simply given by equation 5-6 (Simplicio et al., 2013).

$$\boldsymbol{\nu}_{\text{h}} = \mathbf{G}(\mathbf{u}_{\text{c}} - \mathbf{u}_{\text{a}}) \tag{5-6}$$

The reference model that is used in the prop-shaft velocity loop is hedged by the delta between the commanded and the actual torque. An accurate prop-shaft torque estimate is assumed to be available from either a power-train model or a direct measurement. The dynamics of the implemented command filter are therefore given by,

$$\dot{\boldsymbol{\omega}}_{\text{ref}} = K_{\text{p}}(\boldsymbol{\omega}_{\text{c}} - \boldsymbol{\omega}_{\text{ref}}) - \mathbf{G}_{\omega}(T_{\text{c}} - T_{\text{a}}) \tag{5-7}$$

Where $\boldsymbol{\omega}_{\text{c}}$ and $\boldsymbol{\omega}_{\text{ref}}$ are the commanded and filtered reference prop-shaft velocities respectively. Similarly, T_{c} and T_{a} denote the commanded and actual torques.

Figure 5-2 provides a schematic of the control structure of the prop-shaft velocity controller including the PCH.

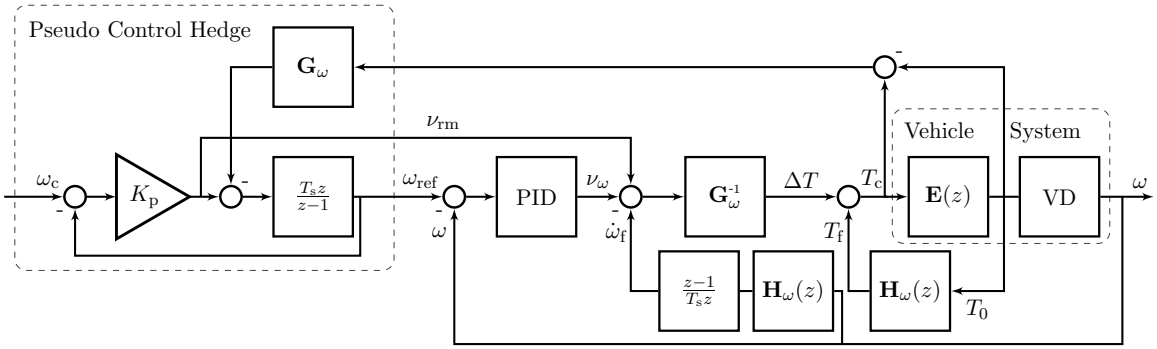

Figure 5-2: A schematic of the prop-shaft velocity controller including the Psuedo Control Hedging (PCH)

5-3 Yaw Rate Control

This section describes the control structure of the yaw-velocity loop based on INDI. Letting $\ddot{\psi}$ be the virtual control ν_ψ in equation 4-1c and subsequently solving for the control input $\boldsymbol{\omega}_{\mathrm{s}}$, results a nonlinear mapping between ν_ψ and $\boldsymbol{\omega}_{\mathrm{s}}$ which produces a linear differential relation between the yaw-rate and the virtual control. Consequently, once this nonlinear map is found, a simple linear controller suffices to control the system with ν_ψ. However, Equation 4-1c reveals that constructing such a map would require the full inversion of a tire-model. Moreover, the control variable $\boldsymbol{\omega}_{\mathrm{p}}$ does not appear affine in 4-1c, i.e., the controlled system has the more general form 3-7. Determining the control input once the virtual control is known, would therefore require solving a nonlinear optimization problem. The problem can be simplified by linearizing the corresponding equations (Andreasson & Bünte, 2006) or by neglecting the nonlinear nature of tire model by using the tire forces as pseudo control inputs and solving for the tire-slips at a later time (Weiskircher & Müller, 2012).

However, these methods only result in approximate feedback linearizations and are characterized by the usual shortcomings of NDI or FBL described in Chapter 3. A different approach would be to linearize the system before inverting the equations, resulting in the robust and straightforward method of INDI (Sieberling et al., 2010).

Linearizing equation 4-2 results in the approximate yaw-rate equations in matrix form.

$$\ddot{\psi} \approx \ddot{\psi}_0 + \mathbf{M}^{-1}{}_{3,3}\mathbf{E}_{3,*}\mathbb{T}_{\mathrm{B,W}}\left(\frac{\partial \mathbf{F}}{\partial \mathbf{x}}\left(\mathbf{x}-\mathbf{x}_0\right)+\frac{\partial \mathbf{F}}{\partial \boldsymbol{\omega}_{\mathrm{p}}}\left(\boldsymbol{\omega}_{\mathrm{p}}-\boldsymbol{\omega}_{\mathrm{p0}}\right)\right) \tag{5-8}$$

Where $\ddot{\psi}_0$, the yaw-acceleration at the time of linearization, can be substituted with a measurement or estimate of the state derivative. The vector $\mathbf{x}$ denotes the state vector and the definition of matrix $\mathbf{M}$, $\mathbf{E}$ and $\mathbb{T}_{\mathrm{B,W}}$ can be found in Chapter 4. Lastly, matrix $\frac{\partial \mathbf{F}}{\partial \mathbf{x}}$ and $\frac{\partial \mathbf{F}}{\partial \boldsymbol{\omega}_{\mathrm{p}}}$ denote the partial derivatives of the tire-forces towards the state vector and the prop-shaft velocities respectively.

Analogous to the inversion of the prop-shaft velocity loop, assuming that the control rate is sufficiently high, such that the state increment over one sample time is much smaller than

the control increment, equation 5-8 simplifies to,

$$\ddot{\psi} \approx \ddot{\psi}_0 + \mathbf{M}^{-1}{}_{3,3}\mathbf{E}_{3,*}\mathbb{T}_{\mathrm{B,W}}\frac{\partial \mathbf{F}}{\partial \boldsymbol{\omega}_{\mathrm{p}}}\Delta\boldsymbol{\omega}_{\mathrm{p}} \tag{5-9}$$

$$\ddot{\psi} \approx \ddot{\psi}_0 + \mathbf{G}_{\psi}\Delta\boldsymbol{\omega}_{\mathrm{p}} \tag{5-10}$$

Where the control effectiveness is abbreviated as $\mathbf{G}_{\psi}$. Equating $\ddot{\psi}$ to ν_{ψ} and solving for $\Delta\boldsymbol{\omega}_{\mathrm{p}}$ yields a mapping between $\Delta\boldsymbol{\omega}_{\mathrm{p}}$ and ν_{ψ} which once applied to equation 4-1c results in an approximate linear differential relation between $\ddot{\psi}$ and ν_{ψ}. A simple linear controller then suffices to control the system with ν_{ψ}.

$$(\nu_{\psi} - \ddot{\psi}_0) = \mathbf{G}_{\psi}\Delta\boldsymbol{\omega}_{\mathrm{p}} \tag{5-11}$$

$$\hat{\nu} = \mathbf{G}_{\psi}\Delta\boldsymbol{\omega}_{\mathrm{p}} \tag{5-12}$$

However, the columns of $\mathbf{G}_{\psi}$ are not linearly independent and therefore equation 5-12 may not have a unique solution in $\Delta\boldsymbol{\omega}_{\mathrm{p}}$. The problem of finding a suitable set of control commands that satisfy equation 5-12 is commonly referred to as control allocation and the method applied in this thesis will be treated in the subsequent section.

5-3-1 Control Allocation

A typical approach to finding a distinct solution to the control allocation problem 5-12 is to simultaneously minimize the deviation from some desired input (Bodson, 2002). In conjunction with an incremental control law, the deviation to some desired control increment $\Delta\boldsymbol{\omega}_{\mathrm{p_d}}$ can be minimized instead. Where $\Delta\boldsymbol{\omega}_{\mathrm{p_d}}$ can be chosen such that it reflects some feed-forward torque or slip distribution associated with maximizing the lateral acceleration as described in (Klomp, 2007). Note that setting the desired control increment to zero does not necessarily wash out the control signal over time but rather minimizes the control rate of change.

If the l_2-norm is used as a measure for the error between the control input and a desired value, the control allocation problem can be cast into,

$$\underset{\Delta\boldsymbol{\omega}_{\mathrm{p}}}{\arg\min} \left\| W_{\mathrm{s}} \left(\Delta\boldsymbol{\omega}_{\mathrm{p}} - \Delta\boldsymbol{\omega}_{\mathrm{d}}\right)\right\|_2 \tag{5-13a}$$

$$\text{subject to } \mathbf{G}_{\psi}\Delta\boldsymbol{\omega}_{\mathrm{p}} = \hat{\nu} \tag{5-13b}$$

$$\Delta\underline{\boldsymbol{\omega}_{\mathrm{p}}} \leq \Delta\boldsymbol{\omega}_{\mathrm{p}} \leq \Delta\overline{\boldsymbol{\omega}_{\mathrm{p}}} \tag{5-13c}$$

Where the weighting matrix W_{s} prioritizes the different actuators and equation 5-13c constrains the solution such that it does not violate any actuator rate or position limits. The actuator rate limits are related to the maximum and minimum realizable prop-shaft rotational accelerations and the sample time t_s as,

$$\Delta\overline{\omega_{\mathrm{p_r}}} = \dot{\omega}_{\mathrm{s}\,\max}(T_{\max}) \cdot t_s \tag{5-14}$$

$$\Delta\underline{\omega_{\mathrm{p_r}}} = \dot{\omega}_{\mathrm{s}\,\min}(T_{\min}) \cdot t_s \tag{5-15}$$

Where $\Delta\underline{\omega_{\mathrm{p_r}}}$ and $\Delta\overline{\omega_{\mathrm{p_r}}}$ depend on the maximum available drive torque and engine drag respectively. Furthermore, prop-shaft velocities that saturate the longitudinal slip on one of

the wheels are taken as absolute limits are transcribed to an incremental form by subtracting the current prop-shaft velocity as,

$$\Delta\overline{\omega_{\mathrm{p}_\sigma}} = \max\left(\omega_{\mathrm{s}\,\mathrm{sat}}(\sigma_{xij}, \sigma_{xij})\right) - \omega_{\mathrm{p}0} \tag{5-16}$$

$$\Delta\underline{\omega_{\mathrm{p}_\sigma}} = \min\left(\omega_{\mathrm{s}\,\mathrm{sat}}(\sigma_{xij}, \sigma_{xij})\right) - \omega_{\mathrm{p}0} \tag{5-17}$$

If the actuator constraints 5-13c are omitted problem 5-13 has an exact solution given by equation 5-18 (Enns, 1998; Härkegård, 2003).

$$\Delta\boldsymbol{\omega}_{\mathrm{p}} = \Delta\boldsymbol{\omega}_{\mathrm{p_d}} + W_{\mathrm{s}}^{-1}\mathbf{G}_{\psi}^{\mathrm{T}}\left(\mathbf{G}_{\psi}W_{\mathrm{s}}^{-1}\mathbf{G}_{\psi}^{\mathrm{T}}\right)^{-1}\left(\hat{\nu} - \Delta\boldsymbol{\omega}_{\mathrm{p_d}}\mathbf{G}_{\psi}\right) \tag{5-18}$$

Although equation 5-18 does not consider any actuator limits, it is straightforwardly modified to approximate the solution to the constrained problem. Firstly , the solution to equation 5-18 is calculated and subsequently clipped such that it does not violate 5-13c. Then, a new control input is calculated using only the remaining control effectors such that it satisfies the residual virtual control. This process is repeated until the solution satisfies equations 5-13 or all the actuators have been saturated. Methods that modify the solution in this way are commonly referred to as Redistributed Pseudo Inverse (RPI) (Virnig & Bodden, 1994) or Cascaded Generalized Inverse (GCI) methods (Bordingnon & Durham, 1995) and are widely used due to their simplicity and low computational burden. However, GCI methods do not always converge to the optimal solution as demonstrated by Bodson, 2002; Härkegård, 2003. Active-set methods do not suffer from this inherent problem and can be demonstrated to converge to the optimal solution in a finite number of steps (Petersen & Bodson, 2006).

This work includes the Weighted Least Squares (WLS) control allocation algorithm, an active-set method described by Härkegård, 2003. It optimizes a modified objective in which the constraint or primary control objective 5-13b is augmented using a parameter γ that reflects the relative importance of the two terms. The resulting problem is given by equations 5-19

$$\arg\min_{\Delta\boldsymbol{\omega}_{\mathrm{p}}} \left\|W_{\mathrm{s}}\left(\Delta\boldsymbol{\omega}_{\mathrm{p}} - \Delta\boldsymbol{\omega}_{\mathrm{d}}\right)\right\|_2 + \gamma\left\|W_v\left(\mathbf{G}_{\psi}\Delta\boldsymbol{\omega}_{\mathrm{p}} - \hat{\nu}\right)\right\|_2 \tag{5-19a}$$

$$\text{subject to } \Delta\underline{\boldsymbol{\omega}_{\mathrm{p}}} \leq \Delta\boldsymbol{\omega}_{\mathrm{p}} \leq \Delta\overline{\boldsymbol{\omega}_{\mathrm{p}}} \tag{5-19b}$$

Which can be compactly written as,

$$\arg\min_{\Delta\boldsymbol{\omega}_{\mathrm{p}}} \left\|\begin{bmatrix}\gamma W_{\nu}\mathbf{G}_{\psi} \\ W_{\mathbf{u}}\end{bmatrix}\Delta\boldsymbol{\omega}_{\mathrm{p}} - \begin{bmatrix}\gamma W_{\nu}\hat{\nu} \\ W_{\mathbf{u}}\mathbf{e}_{\omega_{\mathrm{d}}}\end{bmatrix}\right\|_2 \tag{5-20a}$$

$$\text{subject to } C\Delta\boldsymbol{\omega}_{\mathrm{p}} \geq U \tag{5-20b}$$

Where matrix C and U are chosen such that they reflect the constraints 5-13c and $\mathbf{e}_{\omega_{\mathrm{d}}} = \Delta\boldsymbol{\omega}_{\mathrm{p}} - \Delta\boldsymbol{\omega}_{\mathrm{d}}$ denotes the error between calculated and the desired control increment.

Active-set methods iteratively find the solution to problem 5-19 by treating the inequality constraints belonging to the active-set $\mathcal{W}$, i.e. those inequality constraints for which the condition $C\Delta\omega_{\mathrm{p}} = 0$ holds at the current iteration, as equality constraints. By disregarding the remaining inequality constraints a much simpler equality constraint problem can be solved at each iteration. The optimally of every intermediate solution is checked by examining the Lagrange multipliers given by equation 5-21.

$$\lambda = C_0\begin{bmatrix}\gamma W_{\nu}\mathbf{G}_{\psi} \\ W_{\mathbf{u}}\end{bmatrix}^{\mathrm{T}}\left(\begin{bmatrix}\gamma W_{\nu}\mathbf{G}_{\psi} \\ W_{\mathbf{u}}\end{bmatrix}\Delta\boldsymbol{\omega}_{\mathrm{p}} - \begin{bmatrix}\gamma W_{\nu}\hat{\nu} \\ W_{\mathbf{u}}\mathbf{e}_{\omega_{\mathrm{d}}}\end{bmatrix}\right) \tag{5-21}$$

If the optimal solution has not been found, WLS contains heuristics for removing or adding constraints from or to the working-set. Algorithm 1 provides the necessary steps in pseudo code to finding a solution to 5-19 as described by (Härkegård, 2003).

Algorithm 1 Weighted Least Squares Control Allocation (Härkegård, 2003)

1: **for** i = 1...n **do**
2: Given $\Delta\boldsymbol{\omega}_{\mathrm{p}}^{k}$, find the optimal perturbation $\mathbf{p}^{k}$, while treating the equality constraints $\mathcal{W}$ as equality constraints and disregarding the constraints outside $\mathcal{W}$, such that,

$$\min_{\mathbf{p}} \left\| \begin{bmatrix} \gamma W_{\nu} \mathbf{G}_{\dot{\psi}} \\ W_{\mathbf{u}} \end{bmatrix} \left(\Delta\boldsymbol{\omega}_{\mathrm{p}}^{k} + \mathbf{p}^{k} \right) - \begin{bmatrix} \gamma W_{\nu} \hat{\nu} \\ W_{\mathbf{u}} \mathbf{e}_{\omega_{\mathrm{d}}}^{k} \end{bmatrix} \right\| \tag{5-22}$$

$$\text{subject to } \Delta\underline{\boldsymbol{\omega}_{\mathrm{p}}} \leq \Delta\boldsymbol{\omega}_{\mathrm{p}} \leq \Delta\overline{\boldsymbol{\omega}_{\mathrm{p}}} \tag{5-23}$$

is minimized.
3: **if** $\Delta\boldsymbol{\omega}_{\mathrm{p}}^{k+1} = \Delta\boldsymbol{\omega}_{\mathrm{p}}^{k} + \mathbf{p}^{k}$ is feasible **then**
4: Compute the Lagrange multipliers λ for $\Delta\boldsymbol{\omega}_{\mathrm{p}}^{k+1}$
5: **if** all multipliers corresponding inequality constraints in $\mathcal{W}$, $\lambda \geq 0$ **then**
6: $\Delta\boldsymbol{\omega}_{\mathrm{p}}^{k+1}$ is optimal.
7: **else**
8: Remove the constraint corresponding to the most negative λ from $\mathcal{W}$
9: **else**
10: Determine the maximum step length α such that $\Delta\boldsymbol{\omega}_{\mathrm{p}}^{k+1} = \Delta\boldsymbol{\omega}_{\mathrm{p}}^{k} + \alpha\mathbf{p}^{k}$ is feasible.

Figure 5-3 provides a schematic of the yaw-rate loop described in this section. Similar to the controller described in the previous section, the measured yaw-rate and prop-shaft velocity are filtered using the same second order low-pass filter which reflects the time bandwidth of the yaw-rate response of the vehicle. Lastly, the block that is responsible for control allocation is represented by $\mathbf{G}^{+}_{\dot{\psi}}$.

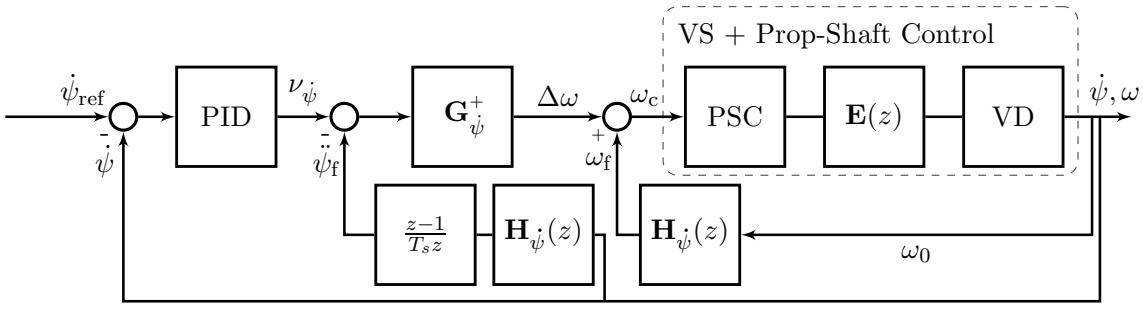

Figure 5-3: Schematic of the yaw-rate controller

5-4 Side-Slip Control

The outer-loop of the control system is formed by a dynamic inversion and feedback path of the vehicle side-slip angle. Contrary to the prop-shaft velocity and yaw-rate loops, the

side-slip angle inversion can be made exact as demonstrated by Sieberling et al., 2010. A prerequisite for both feedback and the dynamic inversion described below, is an accurate measurement or estimation of the side-slip angle and is assumed to be available.

The calculations can be somewhat simplified if planar motion is assumed. The side-slip angle for non-planar motion is given by,

$$\beta = \arcsin\left(\frac{v_y}{V}\right) \tag{5-24}$$

$$\tag{5-25}$$

Which reduces to equation 5-27 if the motion of the vehicle is assumed to be planar.

$$\beta = \arctan\left(\frac{v_y}{v_x}\right) \tag{5-26}$$

$$\tag{5-27}$$

Taking the derivative of equation 5-27 results in,

$$\dot{\beta} = \frac{v_x\dot{v}_y - v_y\dot{v}_x}{v_x^2\left(1 + v_y^2/v_x^2\right)} \tag{5-28}$$

$$\dot{\beta} = \frac{v_x\dot{v}_y - v_y\dot{v}_x}{V} \tag{5-29}$$

$$\tag{5-30}$$

Once more assuming planar motion, the derivatives of the body velocities are given by equations 5-31b.

$$\dot{v}_x = A_x + v_y\dot{\psi} \tag{5-31a}$$

$$\dot{v}_y = A_y - v_x\dot{\psi} \tag{5-31b}$$

Where A_x and A_y denote the longitudinal and lateral specific force respectively. Substituting equations 5-31b into equation 5-30 gives,

$$\dot{\beta} = \underbrace{\frac{A_x v_y - A_y v_x}{V}}_{a_\beta(\mathbf{x},\dot{\mathbf{x}})} + \underbrace{-1}_{b_\beta}\cdot\dot{\psi} \tag{5-32}$$

By letting the derivative of the side-slip angle, $\dot{\beta}$ be the virtual control ν_β for the side-slip inversion loop, a nonlinear map can be constructed which results in a linear differential relation between ν_β and $\dot{\beta}$. Equation 5-33 provides the inversion that lets the side-slip angle be controlled by the yaw-rate.

$$\dot{\psi} = -1 \cdot \left(\nu_\beta - \frac{A_x v_y - A_y v_y}{V}\right) \tag{5-33}$$

Figure 5-4 provides a schematic of the side-slip angle feedback loop. The linear part of the controller is made up of a simple gain K_β however an integrator term might be appropriate if the estimate of the lateral velocity proves insufficiently accurate.

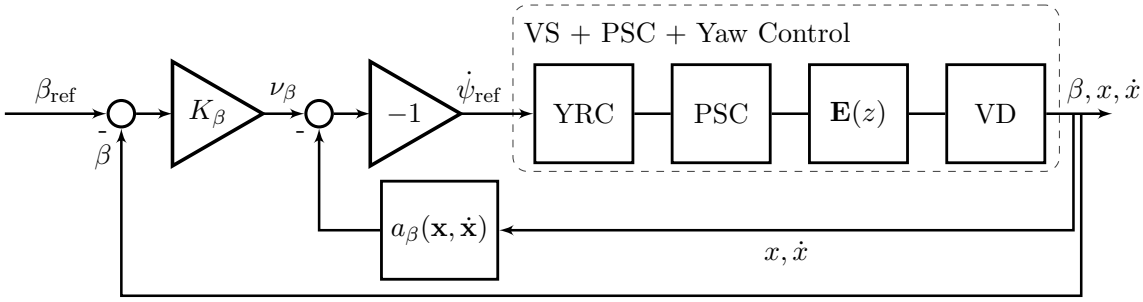

Figure 5-4: Schematic of the outer side-slip angle inversion loop

5-5 Envelope Protection and Yaw-Rate Set-Point

This section describes the bounds on the yaw-rate and vehicle side-slip angle that are used in the envelope control scheme and the yaw-rate controller acting inside the envelope. Beal, 2011 demonstrates, using phase-plane analysis, that the yaw-rate is an important target for vehicle stability augmentation systems as most unstable trajectories caused by steering inputs first result in a steep increase of yaw-rate past a certain maximum value after which the side-slip angle grows rapidly and the vehicle spins. However, some disturbances may increase the side-slip to large values before resulting in vehicle instability (). Beal, 2011 therefore suggests using the maximum rear axle slip-angle as a bound on the vehicle side-slip to prevent instabilities in those circumstances. An advantage of these bounds is that they tend to scale naturally with the vehicle speed and yaw-rate much like the stable region of state-space. Furthermore, in some circumstances it may be appealing to limit lateral tire usage to some degree in order to reduce tire wear and possibly some of the workload associated with driving the vehicle at its limits. However, an experienced driver may consider these bounds too restrictive and looser constraints that allow the driver to push the rear axle past the maximum slip angle may be preferred.

Although more elaborate methods may exist that can be used to more accurately define safe and stable regions of the state-space, these are considered outside the scope of the current work and will not be discussed here. Therefore, the bounds on the yaw-rate and side-slip angle that were described in the work of Beal, 2011 have been applied in the envelope controller. Equation 5-34 gives the bounds on the yaw-rate.

$$\dot{\psi}_{\max} = \begin{cases} \frac{(F_{y\mathrm{f}})_{\max}(1+l_{\mathrm{r}}/l_{\mathrm{f}})}{v_x} & \text{if } (F_{y\mathrm{f}})_{\max} \leq \frac{l_{\mathrm{r}}}{l_{\mathrm{f}}}(F_{y\mathrm{r}})_{\max} \\ \frac{(F_{y\mathrm{r}})_{\max}(1+l_{\mathrm{r}}/l_{\mathrm{f}})}{v_x} & \text{if } (F_{y\mathrm{f}})_{\max} > \frac{l_{\mathrm{r}}}{l_{\mathrm{f}}}(F_{y\mathrm{r}})_{\max} \end{cases} \tag{5-34}$$

Where $(F_{y\mathrm{f}})_{\max}$ and $(F_{y\mathrm{f}})_{\max}$ denote the front and rear lateral force potentials respectively. A maximum yaw-rate exists for both direction of a turn and will be denoted by $\dot{\psi}_{\max}$ and $\dot{\psi}_{\min}$. The bounds on the side-slip angle can be approximated by the linearized slip-angle at the rear wheels,

$$\beta_{\max} = \alpha_{\max} + l_{\mathrm{r}}\dot{\psi} \tag{5-35}$$

$$\beta_{\min} = \alpha_{\min} + l_{\mathrm{r}}\dot{\psi} \tag{5-36}$$

Where the maximum and minimum values correspond to the outside wheel and are determined using the tire-model described in chapter and the current longitudinal slips 4.

The side-slip inversion and cascaded nature of the control system allows the bounds on both the side-slip and the yaw-rate to be combined straightforwardly. If the reference of the side-slip angle inversion is set to one of the side-slip angle bounds, the output represents the yaw-rate necessary to reach this bound as if the associated dynamics behaves like a simple integrator. Therefore, the output of the side-slip angle inversion can be interpreted as a second set of bounds on the yaw-rate that prevent the rear axle side-slip from undesirable levels. Using equation 5-33 the new bounds can simply be expressed as,

$$\dot{\boldsymbol{\psi}}_\beta = -1 \cdot \left(K_\beta \mathbf{e}_\beta - \frac{A_x v_y - A_y v_y}{V} \right) \tag{5-37}$$

Where $\mathbf{e}_\beta$ is given by,

$$\mathbf{e}_\beta = \begin{bmatrix} \beta_{\max} - \beta_0 \\ \beta_{\min} - \beta_0 \end{bmatrix} \tag{5-38}$$

The translated side-slip angle bounds are now straightforwardly related to maximum yaw-rate from equation 5-34 and the current yaw-rate through equation 5-39. This comparison leads to a controller that that does not act inside the safe envelope but tries to intervene as soon as the yaw-rate exceeds any of the bounds described previously.

$$\dot{\psi}_r = \min\left(\max\left(\dot{\psi}_0,\ \dot{\psi}_{lb} \right),\ \dot{\psi}_{ub} \right) \tag{5-39}$$

The lower bound on the yaw-rate is given by minimum value of the translated side-slip bounds and the minimum attainable value of the steady state yaw-rate (5-40a). The upper bound on the yaw-rate is defined similarly (5-40b).

$$\dot{\psi}_{lb} = \min\left(\dot{\boldsymbol{\psi}}_\beta,\ \dot{\psi}_{\min} \right) \tag{5-40a}$$

$$\dot{\psi}_{ub} = \max\left(\dot{\boldsymbol{\psi}}_\beta,\ \dot{\psi}_{\max} \right) \tag{5-40b}$$

Further note that the gain K_β, scales the translated side-slip angle boundaries, with smaller values leading to tighter bounds and higher values to a controller that will intervene later. Beal, 2011; Bobier & Gerdes, 2013 show that the side-slip angle bounds are less critical and therefore K_β should be chosen such that the controller does not prevent the driver from reaching maximum lateral tire usage as quickly as possible, possibly allowing for some overshoot.

The current yaw-rate $\dot{\psi}_0$, can be replaced by a set-point from a reference model resulting in a model following controller that acts inside the safe envelope. A frequently applied set-point generator given by equation 5-41 derived from the linear-bicycle model was applied in this thesis ().

$$\frac{\dot{\psi}_{\mathrm{ss}}}{\delta} = \frac{v_x}{l + K_{ug} v_{\mathrm{x}}^2} \tag{5-41}$$

The understeer gradient K_{ug} given by equation 5-42 reveals some of the handling properties of the linear bicycle model and is extensively described in literature but will not be discussed in detail here.

$$K_{\mathrm{ug}} = -\frac{m}{l} \frac{l_f C_{\alpha \mathrm{f}} - l_r C_{\alpha \mathrm{r}}}{C_{\alpha \mathrm{f}} C_{\alpha \mathrm{r}}} \tag{5-42}$$

Where $C_{\alpha \mathrm{f}}$ and $C_{\alpha \mathrm{r}}$ denote the local or linearized lateral slip-stifness of the front and rear axle respectively. A higher fidelity set-point generator could improve the controller performance

when combined high-performance vehicle operating at the edge of the stable envelope as the accuracy of the linear bicycle model deteriorates in this nonlinear region of the state-space. Furthermore, cases exist in which the steering angle alone is not sufficient to infer the intent of the driver. For example if a driver is stabilizing the vehicle during a drifting maneuver through counter steering, it might not be the case that the driver is seeking to lessen the yaw-rate let alone reach a yaw-rate that is of opposite sign. Although these cases may require a more elaborate approach, finding such a yaw-rate set-point generator was considered outside of the scope of the current work.

Figure 5-5 provides a high level overview of the entire control system.

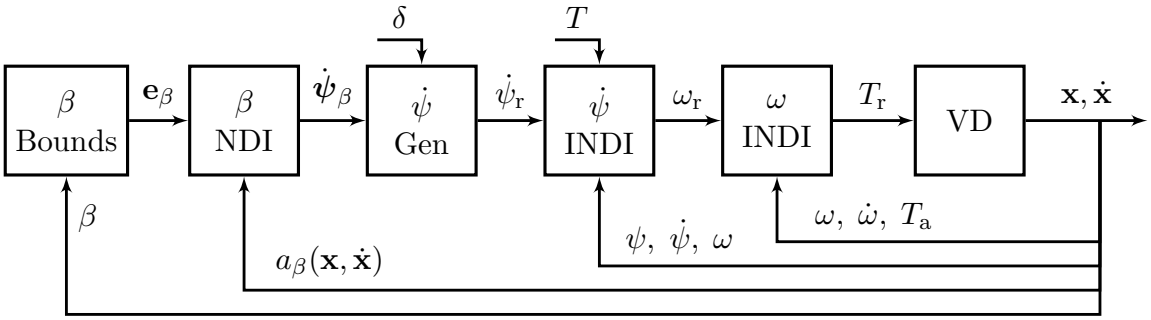

Figure 5-5: High level overview of the complete control system6

Chapter 6

Yaw-Rate Control effectiveness

The control effectiveness in the yaw-rate loop is defined as the partial derivative of the yaw-rate state-equation (4-1c) towards the prop-shaft velocities $\omega_{\mathrm{p}} = [\omega_{\mathrm{pf}}, \omega_{\mathrm{pr}}]^{\mathrm{T}}$ and can conveniently be written in matrix form using equation 4-2.

$$\mathbf{G}(\mathbf{x}_0, \mathbf{u}_0) = \left.\frac{\partial \mathbf{f}(\mathbf{x}, \mathbf{u})}{\partial \mathbf{u}}\right|_{(\mathbf{x}_0,\, \mathbf{u}_0)} = \left.\frac{\partial \ddot{\psi}}{\partial \boldsymbol{\omega}_{\mathrm{p}}}\right|_{(\mathbf{x}_0,\, \omega_{\mathrm{p}0})} = \mathbf{M}^{-1}{}_{3,3}\mathbf{E}_{3,*}\mathbb{T}_{\mathrm{B,W}}\frac{\partial \mathbf{F}}{\partial \boldsymbol{\omega}_{\mathrm{p}}}. \tag{6-1}$$

Where the vector $\mathbf{F}$ denotes the tire-forces in the wheel frame ${}^{\mathrm{w}}\mathbf{F}$. The prop-shaft velocities do not directly influence the tire-forces, therefore equation 6-23 is rewritten as,

$$\mathbf{G}_{\dot{\psi}} = \frac{\partial \ddot{\psi}}{\partial \boldsymbol{\omega}_{\mathrm{p}}} = \frac{\partial \ddot{\psi}}{\partial \boldsymbol{\omega}}\frac{\partial \boldsymbol{\omega}}{\partial \boldsymbol{\omega}_{\mathrm{p}}} = \mathbf{M}^{-1}{}_{3,3}\mathbf{E}_{3,*}\mathbb{T}_{\mathrm{B,W}}\frac{\partial \mathbf{F}}{\partial \boldsymbol{\omega}}\frac{\partial \boldsymbol{\omega}}{\partial \boldsymbol{\omega}_{\mathrm{p}}} \tag{6-2}$$

Where $\boldsymbol{\omega} = [\omega_{\mathrm{fl}}, \omega_{\mathrm{fr}}, \omega_{\mathrm{rl}}, \omega_{\mathrm{rr}}]^{\mathrm{T}}$ is the wheel speed vector and $\boldsymbol{\omega}_{\mathrm{p}} = [\omega_{\mathrm{pf}}, \omega_{\mathrm{pr}}]$ contains the prop-shaft velocities. From equations 4-38 - 4-39, 4-45 - 4-45 and the cases described in section 4-4-2, it is clear that $\frac{\partial \boldsymbol{\omega}}{\partial \boldsymbol{\omega}_{\mathrm{p}}}$ does not have a closed form solution. The estimation of this derivative will be treated in a later section, after finding an expression for $\frac{\partial \mathbf{F}}{\partial \boldsymbol{\omega}}$.

6-1 Tire force Jacobian

In the determination of the force Jacobian, the effects of normal load redistribution due to load-transfers is considered. That traction and braking forces create yaw-moments through load-transfers is well-known. In fact, Shibahata et al., 1993 propose their Direct Yaw-Moment Control (DYC) as a means to compensate for the moments created during accelerating and braking but use a crude estimation. However, in Direct Yaw-Moment Control (DYC) wheels can be actuated individually and as a result, the magnitude of the attainable yaw-moments is large. The effect of load-transfers on the control moments is therefore considered relatively small and slow in comparison and is usually neglected (Jonasson, Andreasson, Jacobson, & Trigell, 2010).

With the system under consideration it is not possible to actuate each wheel individually. As a consequence, the control authority is relatively low and the effect of load-transfers can not be neglected. It will be shown that the moments created through load-transfers have an attenuating effect on the overall control effectiveness and are of the same order as the moments predicted by considering the changes in wheel-speed only. More importantly, influence of load-transfers is shown to be such that under certain conditions the control effectiveness changes sign entirely.

To simplify future calculations, partition the tire force vector ${}^{\mathrm{W}}\mathbf{F}$ into:

$$\bar{\mathbf{F}} = \left[F_{x_{\mathrm{fl}}}, \ldots, F_{x_{\mathrm{rr}}}, F_{y_{\mathrm{fl}}}, \ldots, F_{y_{\mathrm{rr}}}\right]^{\mathrm{T}} \tag{6-3}$$

And define the vector valued tire force function as,

$$\bar{\mathbf{f}}(\boldsymbol{\omega}, \mathbf{F}_{\mathrm{z}}) = \left[f_{\mathrm{fl}}, \ldots, f_{\mathrm{rr}}, g_{\mathrm{fl}}, \ldots, g_{\mathrm{rr}}\right]^{\mathrm{T}} \tag{6-4}$$

Where,

$$f_{ij} : (\omega_{ij}, F_{zij}) \rightarrow f(\omega_{ij}, F_{zij}) \qquad i \in \{\mathrm{f,r}\},\ j \in \{\mathrm{l,r}\}, \tag{6-5}$$

$$g_{ij} : (\omega_{ij}, F_{zij}) \rightarrow g(\omega_{ij}, F_{zij}) \tag{6-6}$$

are given by equations 4-31 and 4-32. The dependencies of $f_{x_{ij}}$ and $g_{y_{ij}}$ on $v_{x_{ij}}$ and $v_{y_{ij}}$ are omitted for reasons of clarity . The vertical wheel load vector is defined as,

$$\mathbf{F}_{\mathrm{z}} = \left[F_{\mathrm{zfl}}, F_{\mathrm{zfr}}, F_{\mathrm{zrl}}, F_{\mathrm{zrr}}\right]^{\mathrm{T}}. \tag{6-7}$$

If only longitudinal load transfers are taken into account, the wheel normal loads, $\mathbf{F}_{\mathrm{z}}$, depend on the longitudinal components of body force vector ${}^{\mathrm{B}}\mathbf{F}$ through equations 4-9 - 4-11. The effect of steering angles on the longitudinal components of the force vector is small and therefore it is assumed that ${}^{\mathrm{B}}\mathbf{F} \approx {}^{\mathrm{W}}\mathbf{F}$. This implies that the normal load can be written as a function of the tire forces directly, $\mathbf{F}_{\mathrm{z}} = h(\bar{\mathbf{F}})$. For the calculation of the contribution of load transfers to the control effectiveness, the nominal part of $\mathbf{F}_{\mathrm{z}}$ is not of interest and therefore omitted. Equations 4-11a - 4-11d reduce to,

$$\mathbf{F}_{\mathrm{z}} = h(\bar{\mathbf{F}}) = \left[-\Delta W_x, -\Delta W_x, \Delta W_x, \Delta W_x\right]^{\mathrm{T}}. \tag{6-8}$$

The tire force function is now defined implicitly by,

$$\bar{\mathbf{F}} = \bar{\mathbf{f}}(\boldsymbol{\omega}, h(\bar{\mathbf{F}})). \tag{6-9}$$

Although this equation can not be used to directly calculate the tire forces from the wheel slips, it can be differentiated to find the derivative of the tire forces towards the wheel slips incorporating the effect of changing normal loads.

Defining the wheel-speed vector $\boldsymbol{\omega}$ as the independent variable, equation 6-9 can be differentiated implicitly, using the chain-rule. Resulting in:

$$\frac{\partial \bar{\mathbf{F}}}{\partial \boldsymbol{\omega}} = \frac{\partial \bar{\mathbf{f}}}{\partial \boldsymbol{\omega}} + \frac{\partial \bar{\mathbf{f}}}{\partial \mathbf{F}_{\mathrm{z}}} \frac{\partial \mathbf{F}_{\mathrm{z}}}{\partial \bar{\mathbf{F}}} \frac{\partial \bar{\mathbf{F}}}{\partial \boldsymbol{\omega}} \tag{6-10}$$

Solving for $\frac{\partial \bar{\mathbf{F}}}{\partial \boldsymbol{\omega}}$ gives,

$$\frac{\partial \bar{\mathbf{F}}}{\partial \boldsymbol{\omega}} = \left(I - \frac{\partial \bar{\mathbf{f}}}{\partial \mathbf{F}_{\mathrm{z}}} \frac{\partial \mathbf{F}_{\mathrm{z}}}{\partial \bar{\mathbf{F}}}\right)^{-1} \frac{\partial \bar{\mathbf{f}}}{\partial \boldsymbol{\omega}} \tag{6-11}$$

Where the term $\frac{\partial \bar{\mathbf{f}}}{\partial \boldsymbol{\omega}}$ corresponds to force Jacobian if no load transfers are considered. The matrix between parentheses, from now on referred to as M, accounts for the changes in the normal load distribution following a change in wheel speed.

Due to the partitioning of $\bar{\mathbf{F}}$, the matrix $\frac{\partial \bar{\mathbf{f}}}{\partial \mathbf{F}_{\mathrm{z}}}$ is made up of two diagonal matrices.

$$\frac{\partial \bar{\mathbf{f}}}{\partial \mathbf{F}_{\mathrm{z}}} = \begin{bmatrix} \frac{\partial \mathbf{f}}{\partial \mathbf{F}_{\mathrm{z}}} \\ \frac{\partial \mathbf{g}}{\partial \mathbf{F}_{\mathrm{z}}} \end{bmatrix} \tag{6-12}$$

Where,

$$\frac{\partial \mathbf{f}}{\partial \mathbf{F}_{\mathrm{z}}} = \mathrm{diag}\begin{pmatrix} \frac{\partial f_{\mathrm{fl}}}{\partial F_{z\,\mathrm{fl}}} & \frac{\partial f_{\mathrm{fr}}}{\partial F_{z\,\mathrm{fr}}} & \frac{\partial f_{\mathrm{rl}}}{\partial F_{z\,\mathrm{rl}}} & \frac{\partial f_{\mathrm{rr}}}{\partial F_{z\,\mathrm{rr}}} \end{pmatrix} \quad \text{and}$$
$$\frac{\partial \mathbf{g}}{\partial \mathbf{F}_{\mathrm{z}}} = \mathrm{diag}\begin{pmatrix} \frac{\partial g_{\mathrm{fl}}}{\partial F_{z\,\mathrm{fl}}} & \frac{\partial g_{\mathrm{fr}}}{\partial F_{z\,\mathrm{fr}}} & \frac{\partial g_{\mathrm{rl}}}{\partial F_{z\,\mathrm{rl}}} & \frac{\partial g_{\mathrm{rr}}}{\partial F_{z\,\mathrm{rr}}} \end{pmatrix}.$$

Similarly, the partial derivative $\frac{\partial \mathbf{F}_{\mathrm{z}}}{\partial \bar{\mathbf{F}}}$ can be expressed in block-form as,

$$\frac{\partial \mathbf{F}_{\mathrm{z}}}{\partial \bar{\mathbf{F}}} = \begin{bmatrix} \frac{\partial \mathbf{F}_{\mathrm{z}}}{\partial \mathbf{F}_x} & \mathbf{0} \end{bmatrix}. \tag{6-13}$$

The block matrix $\frac{\partial \mathbf{F}_{\mathrm{z}}}{\partial \mathbf{F}_x}$ can be simplified further by applying the chain rule a second time using the specific force as an intermediate variable, resulting in,

$$\frac{\partial \mathbf{F}_{\mathrm{z}}}{\partial \mathbf{F}_x} = \frac{\partial \mathbf{F}_{\mathrm{z}}}{\partial A_x} \frac{\partial A_x}{\partial \mathbf{F}_x}. \tag{6-14}$$

Where,

$$\frac{\partial \mathbf{F}_{\mathrm{z}}}{\partial A_x} = \begin{bmatrix} -\frac{\partial \Delta W_x}{\partial A_x} \\ -\frac{\partial \Delta W_x}{\partial A_x} \\ \frac{\partial \Delta W_x}{\partial A_x} \\ \frac{\partial \Delta W_x}{\partial A_x} \end{bmatrix} \quad \text{and} \quad \frac{\partial A_x}{\partial \mathbf{F}_x}^{\mathrm{T}} = \frac{1}{m}\begin{bmatrix} 1 \\ 1 \\ 1 \\ 1 \end{bmatrix}. \tag{6-15}$$

It follows from equations 6-12 - 6-13 that M can be written as,

$$M = \left(I - \frac{\partial \bar{\mathbf{f}}}{\partial \mathbf{F}_{\mathrm{z}}} \frac{\partial \mathbf{F}_{\mathrm{z}}}{\partial \bar{\mathbf{F}}}\right) = \begin{bmatrix} I - \frac{\partial \mathbf{f}}{\partial \mathbf{F}_{\mathrm{z}}} \frac{\partial \mathbf{F}_{\mathrm{z}}}{\partial A_x} \frac{\partial A_x}{\partial \mathbf{F}_x} & \mathbf{0} \\ -\frac{\partial \mathbf{g}}{\partial \mathbf{F}_{\mathrm{z}}} \frac{\partial \mathbf{F}_{\mathrm{z}}}{\partial A_x} \frac{\partial A_x}{\partial \mathbf{F}_x} & I \end{bmatrix} = \begin{bmatrix} A & \mathbf{0} \\ C & I \end{bmatrix} \tag{6-16}$$

Due to its structure, finding the inverse of matrix M is now relatively straightforward and is given by,

$$M^{-1} = \begin{bmatrix} A^{-1} & \mathbf{0} \\ -CA^{-1} & I \end{bmatrix} \tag{6-17}$$

The inverse of sub-matrix A can be found by noting that $\frac{\partial \mathbf{F}_{\mathrm{z}}}{\partial A_x} \frac{\partial A_x}{\partial \mathbf{F}_x}$ is in fact the outer-product of two column vectors. This allows the application of the Sherman-Morrison Formula (Sherman & Morrison, 1950), which gives the inverse of the sum of an invertible matrix K and the vector product uv^{T}, in terms of K^{-1} and vectors u and v (6-18).

$$(K + uv^{\mathrm{T}})^{-1} = K^{-1} - \frac{K^{-1}uv^{\mathrm{T}}K^{-1}}{1 + v^{\mathrm{T}}K^{-1}u} \tag{6-18}$$

Application of equation 6-18 to the inverse of sub-matrix A leads to,

$$A^{-1} = \left(I - \frac{\partial \mathbf{f}}{\partial \mathbf{F}_z}\frac{\partial \mathbf{F}_z}{\partial A_x}\frac{\partial A_x}{\partial \mathbf{F}_x}\right)^{-1} = I + \frac{1}{|A|}\frac{\partial \mathbf{f}}{\partial \mathbf{F}_z}\frac{\partial \mathbf{F}_z}{\partial A_x}\frac{\partial A_x}{\partial \mathbf{F}_x} \tag{6-19}$$

Where the determinant of A is given by,

$$|A| = 1 - \frac{\partial A_x}{\partial \mathbf{F}_x}\frac{\partial \mathbf{f}}{\partial \mathbf{F}_z}\frac{\partial \mathbf{F}_z}{\partial A_x} \tag{6-20}$$

$$= \left(\frac{\partial f_{\mathrm{fl}}}{\partial F_{z\mathrm{fl}}} + \frac{\partial f_{\mathrm{fr}}}{\partial F_{z\mathrm{fr}}} - \frac{\partial f_{\mathrm{rl}}}{\partial F_{z\mathrm{rl}}} - \frac{\partial f_{\mathrm{rr}}}{\partial F_{z\mathrm{rr}}}\right)\frac{\partial \Delta W_x}{A_x} + 1 \tag{6-21}$$

Substituting the result for A^{-1} in $-CA^{-1}$ leads to,

$$-CA^{-1} = \frac{\partial \mathbf{g}}{\partial \mathbf{F}_z}\frac{\partial \mathbf{F}_z}{\partial A_x}\frac{\partial A_x}{\partial \mathbf{F}_x}\left(I + \frac{1}{|A|}\frac{\partial \mathbf{f}}{\partial \mathbf{F}_z}\frac{\partial \mathbf{F}_z}{\partial A_x}\frac{\partial A_x}{\partial \mathbf{F}_x}\right). \tag{6-22}$$

Factoring out $|A|$ and bringing $\frac{\partial \mathbf{F}_z}{\partial A_x}\frac{\partial A_x}{\partial \mathbf{F}_x}$ into the parentheses results in,

$$-CA^{-1} = \frac{1}{|A|}\frac{\partial \mathbf{g}}{\partial \mathbf{F}_z}\left(\frac{\partial \mathbf{F}_z}{\partial A_x}\frac{\partial A_x}{\partial \mathbf{F}_x} - \left[\frac{\partial \mathbf{F}_z}{\partial A_x}\frac{\partial A_x}{\partial \mathbf{F}_x}\frac{\partial A_x}{\partial \mathbf{F}_x}\frac{\partial \mathbf{f}}{\partial \mathbf{F}_z}\frac{\partial \mathbf{F}_z}{\partial A_x} + \frac{\partial \mathbf{F}_z}{\partial A_x}\frac{\partial A_x}{\partial \mathbf{F}_x}\frac{\partial \mathbf{f}}{\partial \mathbf{F}_z}\frac{\partial \mathbf{F}_z}{\partial A_x}\frac{\partial A_x}{\partial \mathbf{F}_x}\right]\right). \tag{6-23}$$

The term within brackets equates to zero, reducing equation 6-23 to,

$$-CA^{-1} = \frac{1}{|A|}\frac{\partial \mathbf{g}}{\partial \mathbf{F}_z}\frac{\partial \mathbf{F}_z}{\partial A_x}\frac{\partial A_x}{\partial \mathbf{F}_x}. \tag{6-24}$$

Matrix inverse M^{-1} is now given by equation 6-25.

$$M^{-1} = \begin{bmatrix} I + \frac{1}{|A|}\frac{\partial \mathbf{f}}{\partial \mathbf{F}_z}\frac{\partial \mathbf{F}_z}{\partial A_x}\frac{\partial A_x}{\partial \mathbf{F}_x} & \mathbf{0} \\ \frac{1}{|A|}\frac{\partial \mathbf{g}}{\partial \mathbf{F}_z}\frac{\partial \mathbf{F}_z}{\partial A_x}\frac{\partial A_x}{\partial \mathbf{F}_x} & I \end{bmatrix} \tag{6-25}$$

Similarly, $\frac{\partial \bar{\mathbf{F}}}{\partial \boldsymbol{\omega}}$ is straightforwardly expressed in terms of the partial derivatives of $\bar{\mathbf{f}}$ and $\mathbf{F}_z$ only (6-26).

$$\frac{\partial \bar{\mathbf{F}}}{\partial \boldsymbol{\omega}} = \begin{bmatrix} I + \frac{1}{|A|}\frac{\partial \mathbf{f}}{\partial \mathbf{F}_z}\frac{\partial \mathbf{F}_z}{\partial \mathbf{F}_x} & \mathbf{0} \\ \frac{1}{|A|}\frac{\partial \mathbf{g}}{\partial \mathbf{F}_z}\frac{\partial \mathbf{F}_z}{\partial \mathbf{F}_x} & I \end{bmatrix}\frac{\partial \bar{\mathbf{f}}}{\partial \boldsymbol{\omega}} \tag{6-26}$$

The partial derivatives, $\frac{\partial \bar{\mathbf{f}}}{\partial \boldsymbol{\omega}}$, $\frac{\partial \mathbf{f}}{\partial \mathbf{F}_z}$ and $\frac{\partial \mathbf{g}}{\partial \mathbf{F}_z}$ appearing in equation 6-26 can either be found analytically or through finite differences, depending on the type of tire-model that is used. In this thesis finite differences were used.

6-1-1 Lateral Load-Transfers

The effect of changing lateral load-transfers can be included into the control effectiveness but is inherently smaller than the load-transfer effects discussed so far. Furthermore, the equations become significantly more complicated and contain more uncertainties on account

of equations 4-9a - 4-9b. Nevertheless, to properly evaluate effects the full effect of load-transfers on the control effectiveness and for reasons of completeness, the equations are given here.

If lateral load-transfers are included, equation 6-8 changes to,

$$\begin{aligned}\mathbf{F}_{\mathrm{z}} = h(\bar{\mathbf{F}}) = &[-\Delta W_x, -\Delta W_x, \Delta W_x, \Delta W_x]^{\mathrm{T}} + \\ &\left[-\Delta W_{y_{\mathrm{f}}}, \Delta W_{y_{\mathrm{f}}}, -\Delta W_{y_{\mathrm{r}}}, \Delta W_{y_{\mathrm{r}}}\right]^{\mathrm{T}}.\end{aligned} \tag{6-27}$$

The partial deri5vative $\frac{\partial \mathbf{F}_{\mathrm{z}}}{\partial \bar{\mathbf{F}}}$ is now a full matrix, given by equation 6-28.

$$\frac{\partial \mathbf{F}_{\mathrm{z}}}{\partial \bar{\mathbf{F}}} = \begin{bmatrix}\frac{\partial \mathbf{F}_{\mathrm{z}}}{\partial \mathbf{F}_x} & \frac{\partial \mathbf{F}_{\mathrm{z}}}{\partial \mathbf{F}_y}\end{bmatrix} \tag{6-28}$$

Where the block-matrix $\frac{\partial \mathbf{F}_{\mathrm{z}}}{\partial \mathbf{F}_y}$ can be expressed as outer product of two vectors (6-29).

$$\frac{\partial \mathbf{F}_{\mathrm{z}}}{\partial \mathbf{F}_y} = \frac{\partial \mathbf{F}_{\mathrm{z}}}{\partial A_y}\frac{\partial A_y}{\partial \mathbf{F}_y} \tag{6-29}$$

Where,

$$\frac{\partial \mathbf{F}_{\mathrm{z}}}{\partial A_y} = \begin{bmatrix}-\frac{\partial \Delta W_{y_{\mathrm{f}}}}{\partial A_y} \\ \frac{\partial \Delta W_{y_{\mathrm{f}}}}{\partial A_y} \\ -\frac{\partial \Delta W_{y_{\mathrm{r}}}}{\partial A_y} \\ \frac{\partial \Delta W_{y_{\mathrm{r}}}}{\partial A_y}\end{bmatrix} \quad \text{and} \quad \frac{\partial A_y}{\partial \mathbf{F}_y}^{\mathrm{T}} = \frac{1}{m}\begin{bmatrix}1\\1\\1\\1\end{bmatrix}. \tag{6-30}$$

Using equations 6-12, 6-14, 6-28 and 6-29 matrix M is rewritten to include the effects of lateral load-transfers, resulting in,

$$\bar{M} = \left(I - \frac{\partial \bar{\mathbf{f}}}{\partial \mathbf{F}_{\mathrm{z}}}\frac{\partial \mathbf{F}_{\mathrm{z}}}{\partial \bar{\mathbf{F}}}\right) = \begin{bmatrix} I - \frac{\partial \mathbf{f}}{\partial \mathbf{F}_{\mathrm{z}}}\frac{\partial \mathbf{F}_{\mathrm{z}}}{\partial A_x}\frac{\partial A_x}{\partial \mathbf{F}_x} & -\frac{\partial \mathbf{f}}{\partial \mathbf{F}_{\mathrm{z}}}\frac{\partial \mathbf{F}_{\mathrm{z}}}{\partial A_y}\frac{\partial A_y}{\partial \mathbf{F}_y} \\ -\frac{\partial \mathbf{g}}{\partial \mathbf{F}_{\mathrm{z}}}\frac{\partial \mathbf{F}_{\mathrm{z}}}{\partial A_x}\frac{\partial A_x}{\partial \mathbf{F}_x} & I - \frac{\partial \mathbf{g}}{\partial \mathbf{F}_{\mathrm{z}}}\frac{\partial \mathbf{F}_{\mathrm{z}}}{\partial A_y}\frac{\partial A_y}{\partial \mathbf{F}_y}\end{bmatrix} = \begin{bmatrix}A & B \\ C & D\end{bmatrix} \tag{6-31}$$

In a manner similar to the method described above, by repeated application of the Sherman-Morrison formula, the inverse of matrix $\bar{M}$ can be found. Resulting in the following expression,

$$\bar{M}^{-1} = \begin{bmatrix}A^{-1} & \mathbf{0} \\ \mathbf{0} & D^{-1}\end{bmatrix}\begin{bmatrix} I + \frac{P}{|\bar{M}|}\frac{\partial \mathbf{f}}{\partial \mathbf{F}_{\mathrm{z}}}\frac{\partial \mathbf{F}_{\mathrm{z}}}{\partial \mathbf{F}_y} & \frac{|A|}{|\bar{M}|}\frac{\partial \mathbf{f}}{\partial \mathbf{F}_{\mathrm{z}}}\frac{\partial \mathbf{F}_{\mathrm{z}}}{\partial \mathbf{F}_y} \\ \frac{|D|}{|\bar{M}|}\frac{\partial \mathbf{g}}{\partial \mathbf{F}_{\mathrm{z}}}\frac{\partial \mathbf{F}_{\mathrm{z}}}{\partial \mathbf{F}_x} & I + \frac{Q}{|\bar{M}|}\frac{\partial \mathbf{g}}{\partial \mathbf{F}_{\mathrm{z}}}\frac{\partial \mathbf{F}_{\mathrm{z}}}{\partial \mathbf{F}_x}\end{bmatrix}. \tag{6-32}$$

Where inverse of sub-matrix D is given by equation 6-33.

$$D^{-1} = I + \frac{1}{|D|}\frac{\partial \mathbf{g}}{\partial \mathbf{F}_{\mathrm{z}}}\frac{\partial \mathbf{F}_{\mathrm{z}}}{\partial \mathbf{F}_y} \tag{6-33}$$

And the determinant of D,

$$|D| = 1 - \frac{\partial A_y}{\partial \mathbf{F}_y}\frac{\partial \mathbf{f}}{\partial \mathbf{F}_{\mathrm{z}}}\frac{\partial \mathbf{F}_{\mathrm{z}}}{\partial A_y}. \tag{6-34}$$

Scalars P and Q are given by equation 6-35 and 6-36 respectively.

$$P = \frac{\partial A_x}{\partial \mathbf{F}_x} \frac{\partial \mathbf{g}}{\partial \mathbf{F}_z} \frac{\partial \mathbf{F}_z}{\partial A_x} \tag{6-35}$$

$$Q = \frac{\partial A_y}{\partial \mathbf{F}_y} \frac{\partial \mathbf{f}}{\partial \mathbf{F}_z} \frac{\partial \mathbf{F}_z}{\partial A_y} \tag{6-36}$$

Finally, the determinant of $\bar{M}$ can be expressed as,

$$\left|\bar{M}\right| = |A|\,|D| - PQ. \tag{6-37}$$

With the inverse of matrix $\bar{M}$ known the control effectiveness, including the effect of changing lateral and longitudinal load-transfers, is now easily found using equation 6-11.

$$\frac{\partial \bar{\mathbf{F}}}{\partial \boldsymbol{\omega}} = \begin{bmatrix} A^{-1} & \mathbf{0} \\ \mathbf{0} & D^{-1} \end{bmatrix} \begin{bmatrix} I + \frac{P}{|\bar{M}|} \frac{\partial \mathbf{f}}{\partial \mathbf{F}_z} \frac{\partial \mathbf{F}_z}{\partial \mathbf{F}_y} & \frac{|A|}{|\bar{M}|} \frac{\partial \mathbf{f}}{\partial \mathbf{F}_z} \frac{\partial \mathbf{F}_z}{\partial \mathbf{F}_y} \\ \frac{|D|}{|\bar{M}|} \frac{\partial \mathbf{g}}{\partial \mathbf{F}_z} \frac{\partial \mathbf{F}_z}{\partial \mathbf{F}_x} & I + \frac{Q}{|\bar{M}|} \frac{\partial \mathbf{g}}{\partial \mathbf{F}_z} \frac{\partial \mathbf{F}_z}{\partial \mathbf{F}_x} \end{bmatrix} \frac{\partial \bar{\mathbf{f}}}{\partial \boldsymbol{\omega}} \tag{6-38}$$

6-1-2 Separating Slip and Load-Tranfer Effects

Looking at equation 6-26 and 6-38 reveals that tire-force jacobian can be written as a sum of two matrices. Respectively $\frac{\partial \bar{\mathbf{f}}}{\partial \boldsymbol{\omega}}$ and a transformed version of this matrix, corresponding to the force Jacobian without load-transfer effects and a term that accounts for changing vertical wheel loads. This partition will be used to investigate the impact of load-transfers on the control effectiveness. Rewriting equation 6-11 is this way results in,

$$\frac{\partial \bar{\mathbf{F}}}{\partial \boldsymbol{\omega}} = \frac{\partial \bar{\mathbf{f}}}{\partial \boldsymbol{\omega}} + \hat{M} \frac{\partial \bar{\mathbf{f}}}{\partial \boldsymbol{\omega}} \tag{6-39}$$

Where the matrix $\hat{M}$ is given by equation 6-40.

$$\hat{M} = \begin{bmatrix} \frac{1}{|A|} \frac{\partial \mathbf{f}}{\partial \mathbf{F}_z} \frac{\partial \mathbf{F}_z}{\partial A_x} \frac{\partial A_x}{\partial \mathbf{F}_x} & \mathbf{0} \\ \frac{1}{|A|} \frac{\partial \mathbf{g}}{\partial \mathbf{F}_z} \frac{\partial \mathbf{F}_z}{\partial A_x} \frac{\partial A_x}{\partial \mathbf{F}_x} & \mathbf{0} \end{bmatrix} \tag{6-40}$$

Substituting equation 6-39 in equation 6-2 the control effectiveness results in a similar partition,

$$\tilde{\mathbf{G}}_{\dot{\psi}} = \mathbf{G}_{\dot{\psi}} + \hat{\mathbf{G}}_{\dot{\psi}} \tag{6-41}$$

Where matrix $\tilde{\mathbf{G}}_{\dot{\psi}}$ stands for the control effectiveness including load-transfer effects, $\mathbf{G}_{\dot{\psi}}$ denotes the component that is caused by wheel-speed increments and $\hat{\mathbf{G}}_{\dot{\psi}}$ accounts for yaw-moments created through changing normal loads.

6-1-3 Actuator Dynamics

For the derivation it was assumed that the wheel-speeds, slips and load-transfers can be approximated by their steady state values when evaluating the much slower body dynamics. In reality however, these phenomena are all governed by their own dynamics, e.g., a torque

increment will not immediately lead to a desired wheel-speed and reaching a certain wheel-speed will not immediately result in the expected wheel-slip and the associated wheel force. The dynamics associated with the output variable of a control loop or control input of a dynamic-system are often referred to as actuator dynamics. In this case it's possible to differentiate between actuator dynamics that are controlled through feedback in a subsequent loop and those that are not. That is, the prop-shaft velocities are controlled to their desired values in subsequent INDI loops, but the slips and the load-transfers remain uncontrolled. Moreover, the load-transfer response is slower than those of the wheel-speeds/slips as it is the result of the rolling and pitching motion of the car. Another way of looking at equation 6-41 is therefore, that $\mathbf{G}_{\dot{\psi}}$ constitutes the fast component of the control effectiveness and that $\hat{\mathbf{G}}_{\dot{\psi}}$ can be seen as a delayed load-transfer effect. Note that speeding up the prop-shaft velocity loop will have almost no effect on the delay of the load-transfer component of the control effectiveness. In fact, $\hat{\mathbf{G}}_{\dot{\psi}}$ is a direct result of car setup and geometry. It is assumed that the bandwidth separation between the load-transfer and the yaw-dynamics is sufficient for the proposed cascaded control structure.

6-2 Ratio of wheel-speed increments

The calculation of the partial derivative of the angular velocities of the wheel speeds to those of the prop-shafts is largely determined by the cases described in section 4-4-2.

The effects of an increment of the front prop-shaft velocity on the rear wheel-speeds and vice versa are assumed to be negligible. Therefore, the derivative $\frac{\partial \boldsymbol{\omega}}{\partial \boldsymbol{\omega}_\mathrm{s}}$ is conveniently expressed as,

$$\frac{\partial \boldsymbol{\omega}}{\partial \boldsymbol{\omega}_\mathrm{s}} = \begin{bmatrix} \frac{\partial \boldsymbol{\omega}}{\partial \omega_{\mathrm{s\,f}}} & \frac{\partial \boldsymbol{\omega}}{\partial \omega_{\mathrm{s\,r}}} \end{bmatrix} = \begin{bmatrix} \frac{\partial \omega_{\mathrm{fl}}}{\partial \omega_{\mathrm{s\,f}}} & 0 \\ \frac{\partial \omega_{\mathrm{fr}}}{\partial \omega_{\mathrm{s\,f}}} & 0 \\ 0 & \frac{\partial \omega_{\mathrm{rl}}}{\partial \omega_{\mathrm{s\,r}}} \\ 0 & \frac{\partial \omega_{\mathrm{rr}}}{\partial \omega_{\mathrm{s\,r}}} \end{bmatrix} \tag{6-42}$$

If the differential of a particular axle is locked, i.e., the relative velocity of the left and right wheels is zero, the dynamics of the power-train is of reduced order. From case 2 in section 4-4-2 we have $\omega_\mathrm{l} = \omega_\mathrm{r} = \omega_\mathrm{s}$. Therefore, for the locked axle the following relation holds,

$$\left(\frac{\partial \omega_\mathrm{l}}{\partial \omega_\mathrm{s}}\right)_i = \left(\frac{\partial \omega_\mathrm{r}}{\partial \omega_\mathrm{s}}\right)_i = 1 \tag{6-43}$$

Where subscript $i \in \{\mathrm{f}, \mathrm{r}\}$ denotes that the derivatives appearing in equation 6-43 belong to either the front or rear power-train.

However, if $(\omega_\mathrm{d})_i \neq 0$ the constraints 4-38 and 4-39 do not provide enough information to determine $\frac{\partial \boldsymbol{\omega}}{\partial \boldsymbol{\omega}_\mathrm{s}}$. In this case the derivative will be approximated using the steady-state wheel speed increments of the linearized power-train dynamics in response to a step-input. Constraint 4-40 can be used to derive an approximation for the non-zero entries appearing in $\frac{\partial \boldsymbol{\omega}}{\partial \omega_{\mathrm{s\,f}}}$ as a function these increments.

$$\frac{\partial \omega_{\mathrm{fl}}}{\partial \omega_{\mathrm{s\,f}}} \approx \frac{\Delta \omega_{\mathrm{fl}}}{\Delta \omega_{\mathrm{s\,f}}} = \frac{2\,(\omega_{\mathrm{fl}})_{\mathrm{ss}}}{(\omega_{\mathrm{fl}})_{\mathrm{ss}} + (\omega_{\mathrm{fr}})_{\mathrm{ss}}} \tag{6-44}$$

$$\frac{\partial \omega_{\mathrm{fr}}}{\partial \omega_{\mathrm{s\,f}}} \approx \frac{\Delta \omega_{\mathrm{rl}}}{\Delta \omega_{\mathrm{s\,f}}} = \frac{2\,(\omega_{\mathrm{fr}})_{\mathrm{ss}}}{(\omega_{\mathrm{fl}})_{\mathrm{ss}} + (\omega_{\mathrm{fr}})_{\mathrm{ss}}} \tag{6-45}$$

Where $(\omega_{ij})_{\text{ss}}$ denotes the steady-state angular-velocity increment of a single wheel due to a unit step torque input. The approximation for the rear axle is defined similarly.

To find the approximate ratio of the wheel speed increments, the corresponding dynamics are linearized. The time scale separation between the power-train and body dynamics is assumed to such that the states corresponding to the body dynamics are approximately constant when evaluating the response of the faster power-train dynamics. If friction losses are neglected and only changes in longitudinal load-transfers are considered, using equation 4-56 - 4-58 and constraints 4-38 - 4-39 the power-train dynamics can be rewritten in terms of the wheel speeds and subsequently linearized around a stationary point ($\dot{\boldsymbol{\omega}}_0 = 0$) resulting in,

$$\dot{\boldsymbol{\omega}} = \mathbf{J}_a \left.\frac{\partial \mathbf{F}_x}{\partial \boldsymbol{\omega}}\right|_{(\mathbf{x}_0,\,\mathbf{u}_0)} (\boldsymbol{\omega} - \boldsymbol{\omega}_0) + \mathbf{J}_b T_0 = \mathbf{J}_a A^{-1} \left.\frac{\partial \bar{\mathbf{f}}}{\partial \boldsymbol{\omega}}\right|_{(\mathbf{x}_0,\,\mathbf{u}_0)} (\boldsymbol{\omega} - \boldsymbol{\omega}_0) + \mathbf{J}_b T_0. \tag{6-46}$$

Matrices $\mathbf{J}_a$ and $\mathbf{J}_b$ are both in block-diagonal form with blocks representing the front and rear power-trains. Matrix $\mathbf{J}_a$ is written as,

$$\mathbf{J}_a = \begin{bmatrix} (\mathbf{J}_a)_{\text{f}} & \mathbf{0} \\ \mathbf{0} & (\mathbf{J_a})_{\text{r}} \end{bmatrix} \tag{6-47}$$

Where,

$$(\mathbf{J}_{\text{a}})_i = \frac{R_e}{N} \begin{bmatrix} 4J + J_{\text{d}} + (1+r)(J_{\text{c}}{+}J_{\text{s}}{+}J_{\text{eq}}) & (r-1)(J_{\text{c}}{+}J_{\text{s}}{+}J_{\text{eq}}) \\ J_{\text{d}} - (r+1)(J_{\text{c}}{+}J_{\text{s}}{+}J_{\text{eq}}) & 4J{+}J_{\text{d}}{+}(1+r)(J_{\text{c}}{+}J_{\text{s}}{+}J_{\text{eq}}) \end{bmatrix}, \tag{6-48}$$

$$r_i = (r_{\text{D}_\text{c}})_i \cdot \text{sng}((\omega_{\text{d}})_i) \tag{6-49}$$

and

$$N = (2J + J_{\text{d}})(J_{\text{s}} + J_{\text{c}} + J_{\text{eq}}). \tag{6-50}$$

Matrix $\mathbf{J}_b$ can be expressed as,

$$\mathbf{J}_b = \begin{bmatrix} (\mathbf{J}_b)_{\text{f}} & \mathbf{0} \\ \mathbf{0} & (\mathbf{J}_b)_{\text{r}} \end{bmatrix} \tag{6-51}$$

Where the sub-matrices are defined as,

$$(\mathbf{J}_b)_i = \frac{1}{N} \begin{bmatrix} K_{\text{eq}}(2J(1-r) + J_{\text{d}}) \\ K_{\text{eq}}(2J(1+r) + J_{\text{d}}) \end{bmatrix} \tag{6-52}$$

Note that for the derivation of matrices $(\mathbf{J}_a)_i$ and $(\mathbf{J}_b)_i$, it was assumed that pre-loading of the differential can be neglected and that the torque applied at the differential-casing is greater than zero, i.e., the max-function and the absolute signs can be dropped from equation 4-58.

The steady state values of the linearized system in response to a unit step-input are straightforwardly found by substituting a unit step in equation 6-46 and solving for the wheel-speeds, resulting in,

$$\boldsymbol{\omega}_{\text{ss}} = -\left(\mathbf{J}_a A^{-1} \frac{\partial \bar{\mathbf{f}}}{\partial \omega}\right)^{-1} \mathbf{J}_b \tag{6-53}$$

Substituting $\boldsymbol{\omega}_{\mathrm{ss}}$ into equations 6-44 and 6-45 results in,

$$\frac{\partial \omega_{\mathrm{fl}}}{\partial \omega_{\mathrm{sf}}} \approx \frac{\Delta \omega_{\mathrm{fl}}}{\Delta \omega_{\mathrm{sf}}} = \frac{2\left(2\frac{\partial F_{x\mathrm{fl}}}{\partial F_{z\mathrm{fl}}} + (1 - r_{\mathrm{f}})\right)\frac{\partial f_{\mathrm{fr}}}{\partial \omega_{\mathrm{fr}}}}{\left(2\frac{\partial F_{x\mathrm{fl}}}{\partial F_{z\mathrm{fl}}} + (1 - r_{\mathrm{f}})\right)\frac{\partial f_{\mathrm{fr}}}{\partial \omega_{\mathrm{fr}}} + \left(2\frac{\partial F_{x\mathrm{fr}}}{\partial F_{z\mathrm{fr}}} + (1 + r_{\mathrm{f}})\right)\frac{\partial f_{\mathrm{fl}}}{\partial \omega_{\mathrm{fl}}}} \tag{6-54}$$

$$\frac{\partial \omega_{\mathrm{fr}}}{\partial \omega_{\mathrm{sf}}} \approx \frac{\Delta \omega_{\mathrm{fr}}}{\Delta \omega_{\mathrm{sf}}} = \frac{2\left(2\frac{\partial F_{x\mathrm{fr}}}{\partial F_{z\mathrm{fr}}} + (1 + r_{\mathrm{f}})\right)\frac{\partial f_{\mathrm{fl}}}{\partial \omega_{\mathrm{fl}}}}{\left(2\frac{\partial F_{x\mathrm{fl}}}{\partial F_{z\mathrm{fl}}} + (1 - r_{\mathrm{f}})\right)\frac{\partial f_{\mathrm{fr}}}{\partial \omega_{\mathrm{fr}}} + \left(2\frac{\partial F_{x\mathrm{fr}}}{\partial F_{z\mathrm{fr}}} + (1 + r_{\mathrm{f}})\right)\frac{\partial f_{\mathrm{fl}}}{\partial \omega_{\mathrm{fl}}}} \tag{6-55}$$

For the rear, similar results can be found,

$$\frac{\partial \omega_{\mathrm{rl}}}{\partial \omega_{\mathrm{sr}}} \approx \frac{\Delta \omega_{\mathrm{rl}}}{\Delta \omega_{\mathrm{sr}}} = \frac{2\left(2\frac{\partial F_{x\mathrm{rl}}}{\partial F_{z\mathrm{rl}}} + (r_{\mathrm{r}} - 1)\right)\frac{\partial f_{\mathrm{rr}}}{\partial \omega_{\mathrm{rr}}}}{\left(2\frac{\partial F_{x\mathrm{rl}}}{\partial F_{z\mathrm{rl}}} + (r_{\mathrm{r}} - 1)\right)\frac{\partial f_{\mathrm{rr}}}{\partial \omega_{\mathrm{rr}}} + \left(2\frac{\partial F_{x\mathrm{rr}}}{\partial F_{z\mathrm{rr}}} - (1 + r_{\mathrm{r}})\right)\frac{\partial f_{\mathrm{rl}}}{\partial \omega_{\mathrm{rl}}}} \tag{6-56}$$

$$\frac{\partial \omega_{\mathrm{rr}}}{\partial \omega_{\mathrm{sr}}} \approx \frac{\Delta \omega_{\mathrm{rr}}}{\Delta \omega_{\mathrm{sr}}} = \frac{2\left(2\frac{\partial F_{x\mathrm{rr}}}{\partial F_{z\mathrm{rr}}} - (1 + r_{\mathrm{r}})\right)\frac{\partial f_{\mathrm{rl}}}{\partial \omega_{\mathrm{rl}}}}{\left(2\frac{\partial F_{x\mathrm{rl}}}{\partial F_{z\mathrm{rl}}} + (r_{\mathrm{r}} - 1)\right)\frac{\partial f_{\mathrm{rr}}}{\partial \omega_{\mathrm{rr}}} + \left(2\frac{\partial F_{x\mathrm{rr}}}{\partial F_{z\mathrm{rr}}} - (1 + r_{\mathrm{r}})\right)\frac{\partial f_{\mathrm{rl}}}{\partial \omega_{\mathrm{rl}}}} \tag{6-57}$$

The approximate wheel-speed ratios are a function of the local longitudinal slip-stiffnesses, the partial derivatives of the tire-model to the normal loads and the differential-ramps respectively $\frac{\partial f_{ij}}{\partial \omega_{ij}}$, $\frac{\partial f_{ij}}{\partial F_{z_{ij}}}$ and $(r_{\mathrm{D_c}})_i$. The dependence of $\boldsymbol{\omega}_{\mathrm{ss}}$ on the inertia's is canceled out due to the left-right symmetry of the power-trains and there is no influence of T_0 due to the linear nature of equation 6-46. If the locking ratio $(r_{\mathrm{D_c}})_i$ is relatively large, the differential will lock at low longitudinal slip values. This means that the values of $\frac{\partial f_{ij}}{\partial F_{z_{ij}}}$ are small compared to the other terms appearing in equations 6-54 through 6-57 and may be neglected.

In conclusion, depending on the state of the differentials, the derivative of the wheel speeds to the prop-shaft velocities is either constraint by the locking mechanism of the differential or approximated by equations 6-54 through 6-57, summarized in equation 6-58 and 6-59.

$$\frac{\partial \boldsymbol{\omega}}{\partial \omega_{\mathrm{sf}}} = \begin{cases} \begin{bmatrix} 1 & 1 & 0 & 0 \end{bmatrix}^{\mathrm{T}} & \text{if } (\omega_{\mathrm{d}})_{\mathrm{f}} = 0 \\ \begin{bmatrix} \frac{\Delta \omega_{\mathrm{fl}}}{\Delta \omega_{\mathrm{sf}}} & \frac{\Delta \omega_{\mathrm{fr}}}{\Delta \omega_{\mathrm{sf}}} & 0 & 0 \end{bmatrix}^{\mathrm{T}} & \text{if } (\omega_{\mathrm{d}})_{\mathrm{f}} \neq 0 \end{cases} \tag{6-58}$$

and

$$\frac{\partial \boldsymbol{\omega}}{\partial \omega_{\mathrm{sr}}} = \begin{cases} \begin{bmatrix} 0 & 0 & 1 & 1 \end{bmatrix}^{\mathrm{T}} & \text{if } (\omega_{\mathrm{d}})_{\mathrm{r}} = 0 \\ \begin{bmatrix} 0 & 0 & \frac{\Delta \omega_{\mathrm{rl}}}{\Delta \omega_{\mathrm{sr}}} & \frac{\Delta \omega_{\mathrm{rr}}}{\Delta \omega_{\mathrm{sr}}} \end{bmatrix}^{\mathrm{T}} & \text{if } (\omega_{\mathrm{d}})_{\mathrm{r}} \neq 0 \end{cases} \tag{6-59}$$

With expressions for $\frac{\partial \boldsymbol{\omega}}{\partial \omega_{\mathrm{sf}}}$ and $\frac{\partial \boldsymbol{\omega}}{\partial \omega_{\mathrm{sr}}}$ the derivative $\frac{\partial \boldsymbol{\omega}}{\partial \boldsymbol{\omega}_{\mathrm{s}}}$ can be approximated and all the elements of equation 6-2 are known. The next section discusses the results found with equation 6-2.

6-3 Evaluation of the Control Effectiveness

This section discusses the results that were found with equation 6-2. The control effectiveness is evaluated at stationary points of the planar vehicle presented in Chapter 4 at different driving torque and steering angle inputs. For a specific longitudinal velocity V_x, the torque input

on a single axle is swept through the full operating range of the respective ICE/MGU while the other is kept zero. This procedure is repeated for different steering angles corresponding to a left-hand turn.

Algorithm 2 Evaluating the front axle Control Effectiveness for V_x

```
for i = 1...n do
    for j = 1...n do
        Given V_x, δ_i, T_j and ω_df = 0
        Find (x_ss)_ij such that [β̇, ψ̈, ω̇_sf, ω̇_sr, ω̇_dr]^T = 0
        if T_D max < |T_fr − T_fl| then
            (Locked condition infeasible)
            Given V_x, δ_i and T_j
            Find (x_ss)_ij such that [β̇, ψ̈, ω̇_sf, ω̇_df, ω̇_sr, ω̇_dr]^T = 0
        Calculate G̃_f((x_ss)_ij, δ_i, T_j)
```

In order to determine the state of the differential, the stationary points are first determined assuming locked conditions, i.e., using the reduced order differential model described in section 4-4. If the maximum locking torque is not sufficient to guarantee locked conditions, stationary point is redetermined using the full differential model. Assuming a locked differential first, results in a slightly larger number of points in which the axle stays locked, due to the difference in static and dynamic friction values. Algorithm 2 describes the basic steps needed for the evaluation of the control effectiveness in different operating points for front axle in pseudo code. Note that unactuated axle is assumed to remain in unlocked condition.

6-3-1 Front Axle

Figure 6-1 depicts the control effectiveness contours determined for the front axle with a locking coefficient $r_{\mathrm{D_c}} = 0.15$ at progressively higher longitudinal velocities. The contours are plotted against the torque and the lateral acceleration as measured in the body frame. Lighter areas represent positive control effectiveness whereas negative control effectiveness appears dark. The red line indicates the zero magnitude isoline.

At low torque inputs the axle is unlocked regardless of steering angle. Moving from the bottom to the top of the plots, the torque input and therefore the locking torque increases, eventually locking the differential. The control effectiveness exhibits a large discontinuity across the point of locking, increasing dramatically in the direction of the locked state.

Incremental Nonlinear Dynamic Inversion is robust against model inaccuracies as long as the sign of the control effectiveness model matches reality (?, ?). Note that the zero magnitude isoline almost always coincides with this discontinuity, except at high torques and low steering inputs at low velocities. Consequently, changing the state of the differential almost always results in a sign change of the control effectiveness. Because the state of the differential can be inferred from wheel speed measurements, the sign of the control effectiveness is therefore known as well. This results in a potentially robust method despite the strong discontinuous behavior and potential model inaccuracies.

Figure 6-1 further reveals that if the velocity is increased the torque at which the front axle locks decreases. Furthermore, the lateral acceleration at which the axle unlocks increases. The combined effect is a larger operating range with positive control effectiveness as the longitudinal velocity increases.

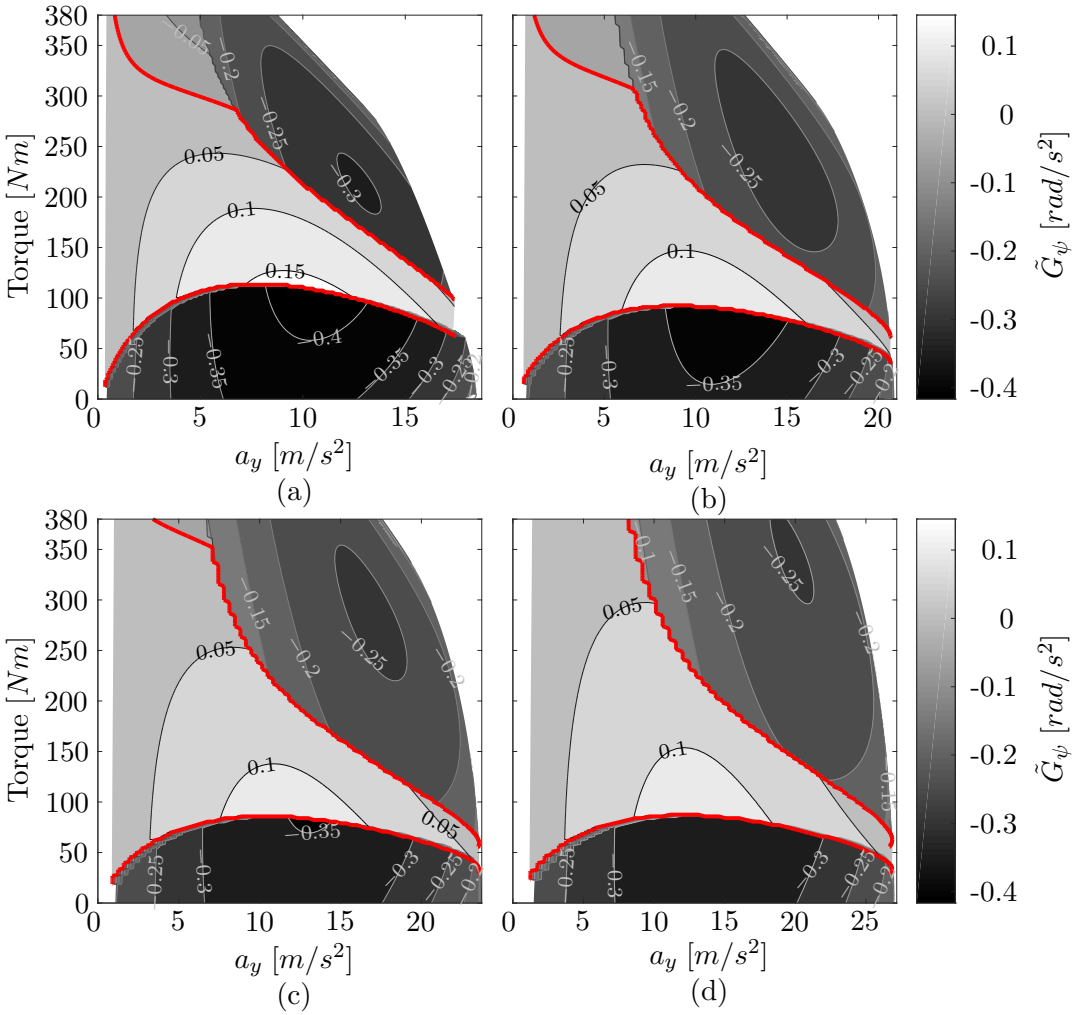

Figure 6-1: Control Effectiveness calculated for the front axle with $r_{D_c} = 0.15$ at progressively higher velocities. Figure (a): $V_x = 30m/s$, Figure (b): $V_x = 40m/s$, Figure (c): $V_x = 50m/s$ and Figure (d): $V_x = 60m/s$.

6-3-2 Rear Axle

Figure 6-2 illustrates the effect of increasing longitudinal velocities on the control effectiveness contours determined for the rear axle with a locking coefficient $r_{D_c} = 0.95$. The differential is locked through most of the operating range due to the large locking coefficient. Consequently, the control effectiveness is mostly positive and grows in magnitude both with torque and lateral acceleration.

Sub-figures (a) through (d) further demonstrate that in contrast to systems that use differential drive/braking, the longitudinal velocity has an attenuating effect on the maximum control effectiveness. This maximum decreases from approximately $0.4\,rad/s^2$ at $V_x = 30\,m/s$ to about $0.2\,rad/s^2$ at $V_x = 60\,m/s$, markedly limiting the control authority at high longitudinal velocities. Further note that compared to the front axle, the longitudinal velocity has little effect on the location of the locking discontinuity.

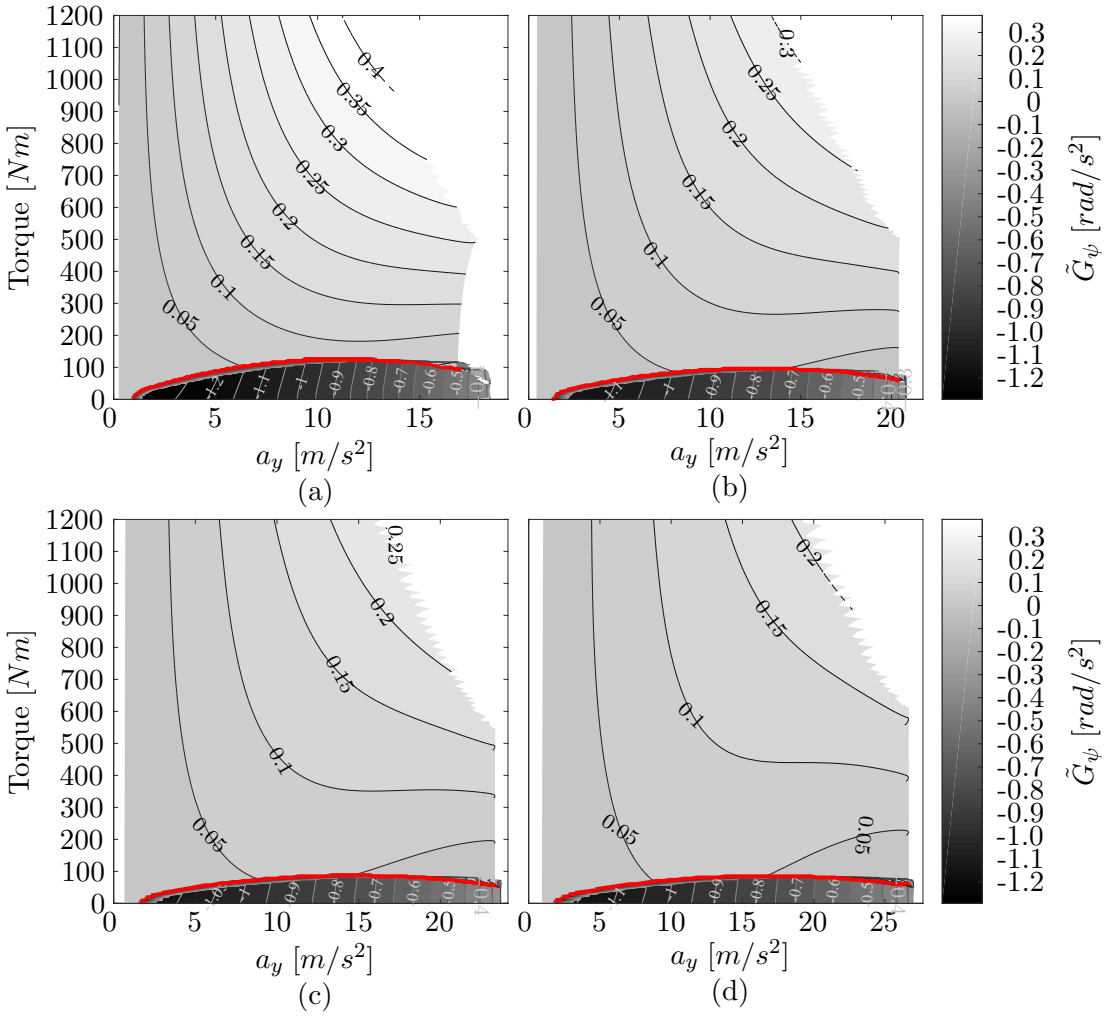

Figure 6-2: Control Effectiveness calculated for the rear axle with $r_{\mathrm{D_c}} = 0.95$ at progressively higher velocities. Figure (a): $V_x = 30m/s$, Figure (b): $V_x = 40m/s$, Figure (c): $V_x = 50m/s$ and Figure (d): $V_x = 60m/s$.

6-3-3 Locking Coefficient

Figure 6-3 illustrates the effects of increasing locking coefficients on the control effectiveness for the rear axle at $V_x = 30m/s$. Sub-figure (a) represents the control effectiveness for $r_{\mathrm{D_c}} = 0$.

With a locking coefficient of zero the axle effectively operates as an open-differential resulting in complete absence of the discontinuity that could be seen in Figures 6-1 and 6-2. The control effectiveness initially increases almost linearly with lateral acceleration, sloping off again halfway through the interval towards the point of maximum acceleration and maximum torque.

Sub-figure (b) depicts the control effectiveness with a tiny locking coefficient, $r_{\mathrm{D_c}} = 0.01$. Even with this small locking coefficient, the operating range at which the axle is locked is considerable, reflected by the band of positive control effectiveness bounded by its characteristic discontinuity. Increasing the control effectiveness has an effect on the control effectiveness in unlocked state although not yet visible in Sub-figure (b). Therefore, the negative region of the control effectiveness is almost identical to Sub-figure (a), preserving the second zero-crossing moving towards maximum torque and maximum lateral acceleration.

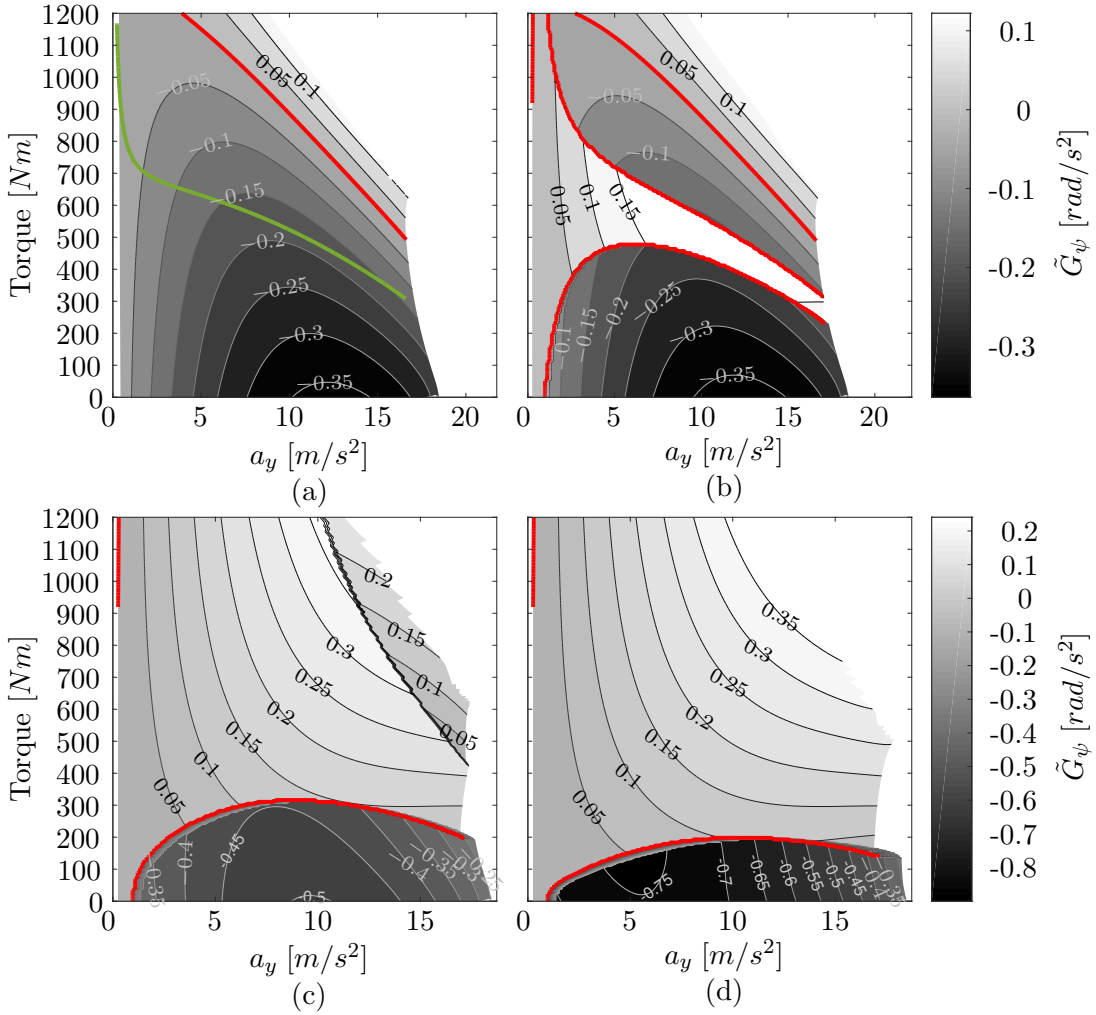

Figure 6-3: Control Effectiveness calculated for the rear axle at $V_x = 30m/s$ for different locking ratio's. Figure (a): $r_{\mathrm{D_c}} = 0.0$, Figure (b): $r_{\mathrm{D_c}} = 0.01$, Figure (c): $r_{\mathrm{D_c}} = 0.2$ and Figure (d): $r_{\mathrm{D_c}} = 0.5$.

Sub-figure (c) depicts the control effectiveness with a locking coefficient of $r_{\mathrm{D_c}} = 0.2$. The larger locking coefficient lowers the torque at which he axle locks and increases the acceleration at which the axle unlocks, substantially increasing the area with locked conditions.

The green line in Sub-figure (a) represents the zero magnitude isoline for the relative angular velocity of both wheels. In the area below this line the outer wheel spins faster than the inside wheel and vice versa opposite of this line. The result of this sign change is that, in the operating range above this line the control effectiveness increases with the locking coefficient and that below this line the control effectiveness decreases with increasing locking coefficient. This can be explained through the fact that the LSD effectively transfers some torque from the faster to the slower spinning wheel.

The areas with locked conditions in Sub-figures (b) through (d) correspond to the areas with zero relative velocity, much like the green line in Sub-figure (a). Another way of looking at Figure 6-3 is therefore that the locked region grows from a line with zero area if there is no locking effect in figure (a) to an area that covers much of the operating range in Sub-figure (d) at a locking coefficient of $r_{\mathrm{D_c}} = 0.5$. The area with locked conditions doesn't grow much further past this point. Increasing the available locking torque therefore primarily increases the understeering effect in unlocked conditions and therefore the growth of the discontinuity at the border of the locked and unlocked operating range.

While the locking coefficient does increase the size of the area with locked conditions, it doesn't change the magnitude of control effectiveness in this area, clearly visible between sub-figures (c) and (d). This can be explained through the fact that these areas are all described by the same reduced order differential model which is unaffected by the locking coefficient.

6-3-4 Load Transfers

Figure 6-4 gives some insight in the effects of load-transfers on the control effectiveness. The plots appearing in the first column of Figure 6-4 depict the control effectiveness if no load-transfer effects are present, corresponding to the nominal control effectiveness $\mathbf{G}_{\dot{\psi}}$. Column two illustrates the isolated effect of load-transfers on the control effectiveness, corresponding to $\hat{\mathbf{G}}_{\dot{\psi}}$. The last column represents the combined effect of slip and load-transfer effects that has been discussed so far.

The second column reveals that the yaw-moment created by load-transfers has an understeering nature on both the front and rear axle, in locked as well as unlocked conditions, i.e., the isolated load-transfer control effectiveness is negative for a left-hand turn or positive steering angle. A simplified explanation can be given by using the longitudinal load-transfer effect. Whenever the prop-shaft velocity is increased, and therefore the longitudinal acceleration, the normal load at the front decreases and the normal load at the rear increases an equal amount. The lateral forces in the front are therefore decreased while they increase it in the front, creating a yaw-moment that opposes the direction of rotation. This effect is important but only partially accounts for the observed effects as it approximately corresponds to the effect of sub-block $\hat{M}_{12}$ of matrix $\hat{M}$ in equation 6-39, if only longitudinal load-transfers are considered.

The load-transfer effect initially increases approximately linear with lateral acceleration and is highest in the low torque regime. The first trend can be explained by realizing that at high

lateral accelerations, changes in normal loads also result in larger changes in lateral loads and consequently larger yaw-moments are generated. The second trend can be explained by noting that the longitudinal slip stiffnesses are high at low torque inputs. This results in a high longitudinal-acceleration over prop-shaft-velocity-increment ratio and therefore strong load-transfer effects.

The magnitude of these load-transfer effects is usually very small compared to the control authority of conventional stability control systems, and are most often neglected completely (?, ?), e.g., in systems featuring differential braking and independent drive systems. In the current context however, the magnitude of the load-transfer effect is of the same order as the nominally available control moments, as reflected by the magnitudes appearing in column one and two of Figure 6-4. Therefore, load-transfers can not be ignored. Instead, they have a considerable effect on the behavior of both actuators.

The effect of load-transfers is most apparent when the axle is unlocked. Row one and two of Figure 6-4, respectively represent the control effectiveness for the front and rear axle, equipped with an open-differential. In steady state, the slip increments of the wheels on an axle with an open differential will be such that the force increase on either wheel is equal. Therefore, an open differential does not create any yaw-moments through differential torque effects but almost entirely through the decrease of lateral tire forces on the respective axle.

On the front axle a decrease of lateral load causes a small yaw-moment opposing the turn, resulting in a nominal control effectiveness that is negative throughout most of the operating range as seen in sub-figure (a). A positive steering angle at the front axle causes part of the force increments to be directed along the body y-axis. At high longitudinal slip stiffnesses, the increase of the longitudinal tire force component along the body y-axis is larger than the decrease of lateral tire-forces resulting from a longitudinal slip increment. The result is a small band of positive nominal control effectiveness at the front axle for low input torques. However, the moments created by load-transfers are relatively large in the low torque regime, resulting in the complete absence of positive total control effectiveness as illustrated by sub-figure (c).

Sub-figure (d) depicts the nominal control effectiveness for the rear axle. A decrease of lateral load at the rear axle causes a small yaw-moment in the direction of the turn resulting in a nominal control effectiveness which is positive throughout the operating range. The zero magnitude isoline coincides with the zero lateral acceleration and torque input lines due to the absence of a steering angle at the rear axle. Although the nominal control effectiveness is positive everywhere, the load-transfer effect is such that the combined effect is negative through a large portion of the operating range. Only a small band of positive control effectiveness in the high torque/acceleration regime remains. Compared to the front axle the effect of load transfers is considerably larger and frequently opposite to what one expects from just considering changes in tire-slip.

Row three and four of Figure 6-4 reveal the components of the control effectiveness of respectively the front and rear, equipped with a locked axle. A prop-shaft velocity increment on an axle with a locked differential, results in an equally large wheel speed increment on both wheels. In contrast to the open differential the torque increase is therefore not always equal on both wheels. As the lateral acceleration increases, the normal load shifts from the inner to the outer wheel, thereby increasing the slip stiffness of the outer wheel and decreasing it on the opposing wheel. Therefore, an equally large wheel speed increment will create a larger change in tire force at the outer wheel than the inner wheel, causing a yaw-moment in the direction

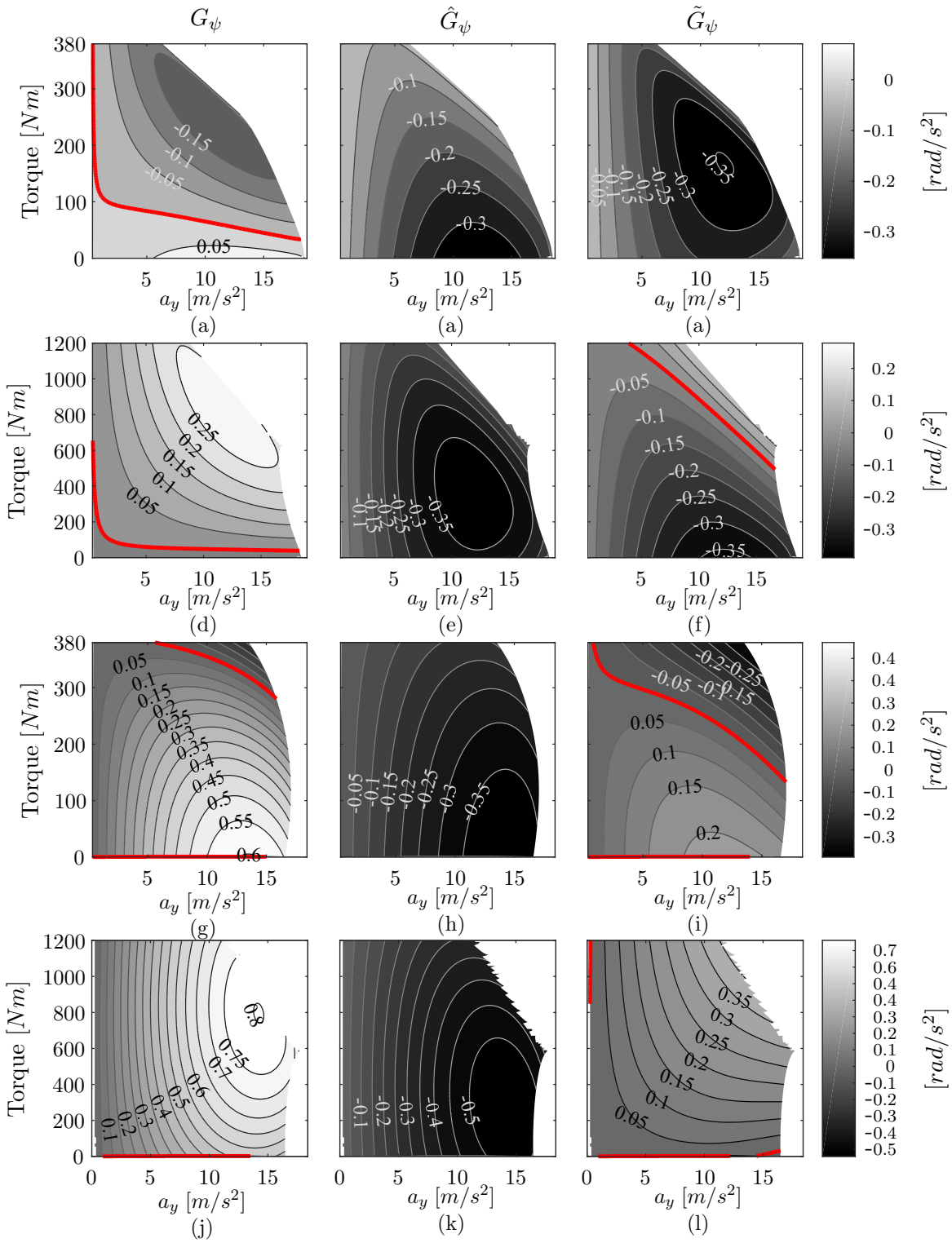

Figure 6-4: The effect of load-transfers on the control effectiveness. For all plots: $V_x = 30m/s$. First row (a,b,c): Front, Open differential. Second row (d,e,f): Rear, Open differential. Third row (g,h,i): Front, Locked Differential. Last row (j,k,l): Rear, Locked Differential. First column (a,d,g,j): No load transfer effects. Second column (b,e,h,k): Load transfer effect only. Last column (c,f,i,l): Total Control Effectiveness.

of the turn. The nominal control effectiveness of a locked axle therefore gradually increases with lateral acceleration, illustrated by the approximately equidistant parallel vertical lines in the low acceleration regime of sub-figures (g) and (j). However, at higher longitudinal slips the yaw-rate itself has a small attenuating effect on the growth of the left/right slip stiffness delta and at the same time causes a slightly higher slip increment at the inner wheel compared to the outer wheel, which cause the nominal control effectiveness to grow less with lateral acceleration than would be expected from just a linear tire model. Tire load sensitivity has a similar effect.

Apart from a yaw-moment through a delta tire-force, a locked axle creates a yaw-moment by decreasing lateral tire forces, similar to the open differential. On the front axle this significantly decreases the control effectiveness in the high acceleration/torque regime as demonstrated by sub-figure (g). The maximum nominal control effectiveness at the front thus occurs at high accelerations in the low torque regime and decreases towards the high torque/acceleration operating range. Inversely, on the rear axle the effect of decreasing lateral loads is to amplify the differential tire-force effect. The result is that the nominal control effectiveness at the rear has a maximum in the high torque/acceleration regime as illustrated by sub-figure (j).

Sub-figure (i) depicts the total control effectiveness at the front axle. As with the open differential, changing load-transfers have a strong attenuating effect on the total control effectiveness of a locked axle. The zero magnitude isoline is shifted down most notably at high accelerations. Sub-figure (l) reveals that changing load-transfers approximately half the magnitude throughout most of the operating range. However, both Sub-figures (i) and (l) demonstrate that load-transfers have a considerably smaller effect on the sign of the control effectiveness of a locked axle compared to an open differential.

Bibliography

Abe, M. (2015). *Vehicle handling dynamics: theory and application*. Butterworth-Heinemann.

Abe, M., Kano, Y., Suzuki, K., Shibahata, Y., & Furukawa, Y. (2001). Side-slip control to stabilize vehicle lateral motion by direct yaw moment. *JSAE review*, *22*(4), 413–419.

Amodeo, M., Ferrara, A., Terzaghi, R., & Vecchio, C. (2010). Wheel slip control via second-order sliding-mode generation. *IEEE Transactions on Intelligent Transportation Systems*, *11*(1), 122-131. (cited By 59)

Andreasson, J., & Bünte, T. (2006). Global chassis control based on inverse vehicle dynamics models. *Vehicle System Dynamics*, *44*(sup1), 321–328.

Bacon, B., & Ostroff, A. (2000). Reconfigurable flight control using nonlinear dynamic inversion with a special accelerometer implementation. In *Aiaa guidance, navigation, and control conference and exhibit.* (cited By 14)

Beal, C. E. (2011). *Applications of model predictive control to vehicle dynamics for active safety and stability*. Stanford University.

Bobier, C. G. (2012). *A phase portrait approach to vehicle stabilization and envelope control*. Unpublished doctoral dissertation, Stanford University.

Bobier, C. G., & Gerdes, J. C. (2013). Staying within the nullcline boundary for vehicle envelope control using a sliding surface. *Vehicle System Dynamics*, *51*(2), 199–217.

Bodson, M. (2002). Evaluation of optimization methods for control allocation. *Journal of Guidance, Control, and Dynamics*, *25*(4), 703–711.

Bordingnon, K. A., & Durham, W. C. (1995). Closed-form solutions to constrained control allocation problem. *Journal of Guidance, Control, and Dynamics*, *18*(5), 1000–1007.

Cho, W., Yoon, J., Kim, J., Hur, J., & Yi, K. (2008). An investigation into unified chassis control scheme for optimised vehicle stability and manoeuvrability. *Vehicle System Dynamics*, *46*(SUPPL.1), 87-105. (cited By 64)

Delli Colli, V., Tomassi, G., & Scarano, M. (2006). "single wheel" longitudinal traction control for electric vehicles. *IEEE Transactions on Power Electronics*, *21*(3), 799-808. (cited By 45)

Di Cairano, S., Tseng, H., Bernardini, D., & Bemporad, A. (2013). Vehicle yaw stability control by coordinated active front steering and differential braking in the tire sideslip

angles domain. *IEEE Transactions on Control Systems Technology*, *21*(4), 1236-1248. (cited By 62)

Drakunov, S. V., Ashrafi, B., & Rosiglioni, A. (2000). Yaw control algorithm via sliding mode control. In *Proceedings of the american control conference, 2000.* (Vol. 1, pp. 580–583).

Enns, D. (1998). Control allocation approaches. In *Guidance, navigation, and control conference and exhibit* (p. 4109).

FIA. (2016). *2016 technical regulations for lmp1 prototype.*

Forstinger, M., Bauer, R., & Hofer, A. (2015). Modelling and simulation of passive limited-slip differentials. *IFAC-PapersOnLine*, *48*(1), 502–507.

Fredriksson, J., Andreasson, J., & Laine, L. (2004). Wheel force distribution for improved handling in a hybrid electric vehicle using nonlinear control. In *Decision and control, 2004. cdc. 43rd ieee conference on* (Vol. 4, pp. 4081–4086).

Härkegård, O. (2003). *Backstepping and control allocation with applications to flight control.* Unpublished doctoral dissertation, Linköpings universitet.

Holzapfel, F., & Sachs, G. (2004). Dynamic inversion based control concept with application to an unmanned aerial vehicle. In *Aiaa guidance, navigation, and control conference and exhibit* (p. 4907).

Hsu, Y.-H. J., & Gerdes, J. C. (2005). Stabilization of a steer-by-wire vehicle at the limits of handling using feedback linearization. In *Proceedings of imece2005.*

Inagaki, S., Kshiro, I., & Yamamoto, M. (1994). Analysis on vehicle stability in critical cornering using phase-plane method. In *International symposium on advanced vehicle control (1994: Tsukuba-shi, japan). proceedings of the international symposium on advanced vehicle control 1994.*

ISO/TC22/SC33. (2011, December). *Road vehicles - vehicle dynamics and road-holding ability - vocabulary* (Vol. 2011; Standard). Geneva, CH: International Organization for Standardization.

Johnson, E. N. (2000). *Limited authority adaptive flight control.* Unpublished doctoral dissertation, School of Aerospace Engineering, Georgia Institute of Technology.

Johnson, E. N., & Calise, A. J. (2000). Pseudo-control hedging: A new method for adaptive control. In *Advances in navigation guidance and control technology workshop.*

Jonasson, M. (2009). *Exploiting individual wheel actuators to enhance vehicle dynamics and safety in electric vehicles.* Unpublished doctoral dissertation, KTH Royal Institute of Technology.

Jonasson, M., Andreasson, J., Jacobson, B., & Trigell, A. S. (2010). Global force potential of over-actuated vehicles. *Vehicle system dynamics*, *48*(9), 983–998.

Klomp, M. (2007). *On drive force distribution and road vehicle handling-a study of understeer and lateral grip.* Unpublished doctoral dissertation.

Klomp, M. (2010). *Longitudinal force distribution and road vehicle handling.* Unpublished doctoral dissertation, Chalmers University of Technology.

Kokotovic, P. V., O'malley, R., & Sannuti, P. (1976). Singular perturbations and order reduction in control theoryan overview. *Automatica*, *12*(2), 123–132.

Lombaerts, T., Looye, G., Chu, Q., & Mulder, J. (2010). Pseudo control hedging and its application for safe flight envelope protection. In *Aiaa guidance, navigation, and control conference.* (cited By 4)

Manning, W., & Crolla, D. (2007). A review of yaw rate and sideslip controllers for passenger vehicles. *Transactions of the Institute of Measurement and Control*, *29*(2), 117–135.

Milliken, W. F., & Milliken, D. L. (1995). *Race car vehicle dynamics* (Vol. 400). Society of Automotive Engineers Warrendale.

Morselli, R., Zanasi, R., & Sandoni, G. (2006). Detailed and reduced dynamic models of passive and active limited-slip car differentials. *Mathematical and Computer Modelling of Dynamical Systems*, *12*(4), 347–362.

Motoyama, S., Uki, H., ISODA Manager, K., & YUASA Manager, H. (1993). Effect of traction force distribution control on vehicle dynamics. *Vehicle System Dynamics*, *22*(5-6), 455–464.

Pacejka, H. (2005). *Tire and vehicle dynamics*. Elsevier.

Pacejka, H. B., & Bakker, E. (1992). The magic formula tyre model. *Vehicle system dynamics*, *21*(S1), 1–18.

Park, J., & Kim, C. (1999). Wheel slip control in traction control system for vehicle stability. *Vehicle System Dynamics*, *31*(4), 263-278. (cited By 28)

Petersen, J. A., & Bodson, M. (2006). Constrained quadratic programming techniques for control allocation. *IEEE Transactions on Control Systems Technology*, *14*(1), 91–98.

Piyabongkarn, D., Lew, J., Rajamani, R., Grogg, J., & Yuan, Q. (2007). On the use of torque-biasing systems for electronic stability control: Limitations and possibilities. *IEEE Transactions on Control Systems Technology*, *15*(3), 581-589. (cited By 34)

Rajamani, R. (2011). *Vehicle dynamics and control*. Springer Science & Business Media.

Reiner, J., Balas, G. J., & Garrard, W. L. (1996). Flight control design using robust dynamic inversion and time-scale separation. *Automatica*, *32*(11), 1493–1504.

Schumacher, C., Khargonekar, P., & McClamroch, N. (1998). Stability analysis of dynamic inversion controllers using time-scale separation. In *Guidance, navigation, and control conference and exhibit* (p. 4322).

Sherman, J., & Morrison, W. J. (1950). Adjustment of an inverse matrix corresponding to a change in one element of a given matrix. *The Annals of Mathematical Statistics*, *21*(1), 124–127.

Shi, J., Li, X., Lu, T., & Zhang, J. (2012). Development of a new traction control system for vehicles with automatic transmissions. *International Journal of Automotive Technology*, *13*(5), 743-750. (cited By 3)

Shibahata, Y., Shimada, K., & Tomari, T. (1993). Improvement of vehicle maneuverability by direct yaw moment control. *Vehicle System Dynamics*, *22*(5-6), 465–481.

Sieberling, S., Chu, Q., & Mulder, J. (2010). Robust flight control using incremental nonlinear dynamic inversion and angular acceleration prediction. *Journal of Guidance, Control, and Dynamics*, *33*(6), 1732-1742. (cited By 76)

Simplicio, P., Pavel, M., Kampen, E. van, & Chu, Q. (2013). An acceleration measurements-based approach for helicopter nonlinear flight control using incremental nonlinear dynamic inversion. *Control Engineering Practice*, *21*(8), 1065-1077. (cited By 26)

Slotine, J.-J. E., Li, W., et al. (1991). *Applied nonlinear control* (Vol. 199) (No. 1). prentice-Hall Englewood Cliffs, NJ.

Smeur, E., Chu, Q., & De Croon, G. (2016). Adaptive incremental nonlinear dynamic inversion for attitude control of micro air vehicles. *Journal of Guidance, Control, and Dynamics*, *39*(3), 450-461. (cited By 1)

Smith, P. (1998). A simplified approach to nonlinear dynamic inversion based flight control. In *23rd atmospheric flight mechanics conference* (p. 762-770). (cited By 0)

Snell, S., Enns, D., & Garrard, W. (1992). Nonlinear inversion flight control for a super-

maneuverable aircraft. *Journal of Guidance, Control, and Dynamics*, *15*(4), 976-984. (cited By 351)

Song, J., & Boo, K. (2004). Performance evaluation of traction control systems using a vehicle dynamic model. *Proceedings of the Institution of Mechanical Engineers, Part D: Journal of Automobile Engineering*, *218*(7), 685-696. (cited By 18)

Svendenius, J. (2007). Tire modeling and friction estimation (Doctoral dissertation, Lund Institute of Technology, Lund Universitycs). *PhD Theses*.

Tahami, F., Kazemi, R., & Farhanghi, S. (2003). A novel driver assist stability system for all-wheel-drive electric vehicles. *IEEE Transactions on Vehicular Technology*, *52*(3), 683-692. (cited By 85)

Tchamna, R., & Youn, I. (2013). Yaw rate and side-slip control considering vehicle longitudinal dynamics. *International Journal of Automotive Technology*, *14*(1), 53-60. (cited By 21)

Tomizuka, M., & Hedrick, J. (1995). Advanced control methods for automotive applications. *Vehicle System Dynamics*, *24*(6-7), 449-468. (cited By 30)

Uffelmann, F. (1983). Automotive stability and handling dynamics in cornering and braking maneuvers. *Vehicle System Dynamics*, *12*(4-5), 203–223.

Van Zanten, A. (2000). *Bosch esp systems: 5 years of experience* (Tech. Rep.). SAE Technical Paper. (cited By 33)

Van Zanten, A., Erhardt, R., & Pfaff, G. (1995). *Vdc, the vehicle dynamics control system of bosch* (Tech. Rep.). SAE Technical Paper. (cited By 21)

Virnig, J., & Bodden, D. (1994). Multivariable control allocation and control law conditioning when control effectors limit. In *Guidance, navigation, and control conference* (p. 3609).

Weiskircher, T., & Müller, S. (2012). Control performance of a road vehicle with four independent single-wheel electric motors and steer-by-wire system. *Vehicle system dynamics*, *50*(sup1), 53–69.

Yim, S., Choi, J., & Yi, K. (2012). Coordinated control of hybrid 4wd vehicles for enhanced maneuverability and lateral stability. *IEEE Transactions on Vehicular Technology*, *61*(4), 1946-1950. (cited By 30)

Zanasi, R., Sandoni, G., & Morselli, R. (2001). Simulation of variable dynamic dimension systems: the clutch example. In *Control conference (ecc), 2001 european* (pp. 3149–3154).